

**HIGHLY CONDUCTIVE SODIUM DODECYL SULPHATE TREATED  
POLY (3,4-ETHYLENETHIOXYLTHIOPHENE) : POLYSTYRENE SULFONATE  
(PEDOT: PSS) CONTAINING COPPER NANOPARTICLES FOR FLEXIBLE  
ORGANIC SOLAR CELLS**

**By**

**CYNTHIA MWANSA**

**A Dissertation submitted to the University of Zambia in partial fulfilment of the  
requirement of the degree of Master of Science in Physics**

**THE UNIVERSITY OF ZAMBIA**

**LUSAKA**

**2020**

## **Declaration**

I, Cynthia Mwansa hereby declare that this dissertation represents my work and has not previously been submitted for a degree at this or any other University.

**Signed:** .....

**Date:** .....

## **Copyright**

All rights reserved. No part of this dissertation may be reproduced or stored in any form or by any means without prior permission in writing from the author or the University of Zambia.

## Approval

The dissertation of **Cynthia Mwansa** is approved as fulfilling part of the requirements for the award of the degree of **Master of Science in Physics** by the University of Zambia.

**1. Examiner 1**

Name: .....

Signature: .....

Date: .....

**2. Examiner 2**

Name: .....

Signature: .....

Date: .....

**3. Examiner 3**

Name: .....

Signature: .....

Date: .....

**4. Chairperson- Board of Examiners**

Name: .....

Signature: .....

Date: .....

**5. Supervisor**

Name: .....Dr. Onesmus Munyati.....



Signature: .....

Date:.....14 September 2020.....

## Abstract

Polymer Solar Cells (PSCs) have attracted great attention due to the advantages of their light weight, flexibility and low cost. The typical device architecture of polymer based solar cell consists Indium Tin Oxide (ITO) on glass as the transparent conducting electrode, Poly (3, 4-ethylenedioxythiophene): polystyrene sulfonate (PEDOT: PSS) as the hole transport layer, a photoactive layer and aluminium as the back contact. ITO is brittle and mechanically rigid making the solar cell device not to be flexible. This has motivated the search for alternatives to replace ITO. One such candidate is PEDOT:PSS. Although treatment with various solvents has demonstrated the ability to increase the conductivity of PEDOT: PSS, its conductivity has remained relatively low compared to that of ITO. In order to make PEDOT: PSS viable for use in ITO free solar cells, there is need to increase its conductivity and transparency. In this study, the optical, morphological and electrical properties of PEDOT: PSS films doped with sodium dodecyl sulphate (SDS) and copper nanoparticles (CuNPs) are investigated. Solutions of PEDOT: PSS containing different amounts of SDS and copper nanoparticles were prepared to determine the optimum loading levels. The solutions were sonicated and then deposited by spin coating onto pre-cleaned glass substrates. The films produced were characterized using Ultraviolet-Visible (UV-VIS) spectroscopy to determine the optical properties while atomic force microscopy (AFM) was used to evaluate morphological characteristics. Characterisation of the structural properties was done using X-ray diffraction (XRD), Scanning electron microscopy (SEM) and Raman. Charge carrier mobility was characterised using the Hall Effect Measurements. Conductivity measurements were done using a four-point probe coupled to a source meter. The conductivity of PEDOT: PSS films were significantly enhanced from  $0.56 \pm 0.19$  S/cm to  $3772.86 \pm 53.18$  S/cm by treatment with sodium dodecyl sulphate (SDS) and doping using copper nanoparticles. This high conductivity was as a result of the conformational change of the PEDOT:PSS from Benzoid (coiled) to Quinoid (linear) as confirmed by Raman. The AFM images showed segregated PEDOT and PSS regions at lower doping levels. The morphology evolved into a 'honey comb' structure consisting inter-connected PEDOT regions which improved the charge transport hence conductivity. XRD peak at  $41.6^\circ$  corresponded to the presence of copper in PEDOT:PSS:SDS:CuNPs and the size of the crystal was calculated as 5.83nm. SEM images revealed a well-connected percolation network of CuNPs which formed a Face Centered Cubic (FCC) nanocrystal and nanosoldering structures hence enhancing conductivity and decreased the nanowire-nanowire (NW-NW) contact resistance by increasing the contact surface area under the assistance of the conducting polymer (PEDOT:PSS). The charge carrier mobility increased from  $0.5 \text{cm}^2/\text{Vs}$  to  $5.3 \text{cm}^2/\text{Vs}$  after the addition of SDS and copper nanoparticles. From these results, it was concluded that the tremendous increase in conductivity arose mainly by increased charge carrier mobility.

## **Dedication**

This work is dedicated to my children (Natasha Bupe Bwalya, Nandi Nsansa Bwalya and Nkandu Lerato Bwalya) and Aquila Mwansa for bearing my busy schedule and not forgetting my husband ‘Bwalya Bupe Bwalya’ who supported me from the beginning till the end. Thank you for giving me strength to forge ahead.

To my parents (Kenneth Mbokolo Mwansa and Beatrice Kaoma Mwansa), you are a blessing to me. Mum and Dad, your teaching, guidance, encouragement and sacrifice is what has made me to achieve all this today. I will always be grateful.

To God almighty, my creator and pillar of strength, my source of wisdom, I am who I am today because you made it possible.

## **Acknowledgements**

First of all, I would like to thank my supervisor Dr. Onesmus Munyati and co-supervisor Dr. Sylvester Hatwaambo for all the guidance and support. I wish to extend my gratitude to the Energy and Environmental Research Group (EERG) and ISP (International Science Program) for funding my research.

I would like to thank the staff at the Department of Physics and Chemistry for making my time here pleasant and conducive for research.

I wish to thank Isabel Chisulo, Simon Mwale, and Chipo Siabamba (Chief Scientist, Department of Chemistry), for introducing me to AFM, four-point probe measurements, UV-VIS spectroscopy and FTIR techniques. Also thanking Mr Bundala (Department of Physics) and MrDaka (Department of Chemistry) for providing the necessary materials I needed for research. I extend my gratitude to Pannan Kyesmen and the University of Pretoria for SEM, XRD and Raman characterisation of the samples. I want to thank Sawa Hezekiah from University of Dar es salaam for characterisation of the Hall Effect measurements.

Last, but certainly not the least, I would like to thank my family and friends, especially my siblings Brilliant Mwansa, Matilda Mwansa, Abigail Mwansa, Susan Mwansa and Kenneth Mwansa for their encouragement and making sure that my time spent outside the confines of the laboratory were also pleasant.

## TABLE OF CONTENTS

Declaration .....	ii
Copyright .....	iii
Approval .....	iv
Abstract .....	v
Dedication .....	vi
Acknowledgements .....	vii
List of Figures .....	xiii
List of Tables .....	xvi
Appendix .....	xvii
List of Acronyms .....	xviii
CHAPTER ONE .....	1
INTRODUCTION .....	1
1.0 Background .....	1
1.1 Statement of the problem .....	3
1.2 Objectives .....	3
1.2.1 Main Objective .....	3
1.2.2 Specific objectives .....	4
1.3 Research questions .....	4

1.5 Significance of the Study .....	4
CHAPTER TWO .....	6
THEORETICAL BACKGROUND .....	6
2.0 Introduction .....	6
2.1 Theoretical Background of Polymer Solar Cells .....	15
2.1.1 Transparent Conductive Electrode .....	16
2.1.2 PEDOT:PSS as a Hole Transporting Layer (HTL) .....	17
2.1.3 Active Layer .....	17
2.1.4 Metal Electrode.....	18
2.2 Conducting Polymers .....	18
2.2.1 PEDOT: PSS .....	19
2.3 Sodium Dodecyl Sulfate (SDS) .....	24
2.4 Charge Transportation in Polymer Solar Cells .....	25
2.5 Charge Mobility .....	28
2.6 Doping.....	29
2.6.1 Doping in conductive polymers.....	30
2.6.2 Doping in organic molecular semiconductors .....	31
2.7 Morphology.....	31
2.8 Hole transporting layers .....	32

CHAPTER THREE .....	35
LITERATURE REVIEW .....	35
3.0 Introduction .....	35
CHAPTER FOUR.....	40
EXPERIMENTAL METHODS .....	40
4.0 Introduction .....	40
4.1 Materials Preparation .....	40
4.2 Sample Preparation .....	41
4.2.1 PEDOT: PSS containing sodium dodecyl sulfate.....	41
4.2.2 PEDOT:PSS containing Sodium dodecyl sulfate and copper nanoparticles ...	41
4.2.2.1 Synthesis of copper nanoparticles .....	41
4.2.3 Film Deposition .....	42
4.3 Experimental Techniques .....	42
4.3.1 Atomic force microscopy (AFM) .....	43
4.3.1.1 Characterisation using Atomic Force Microscopy .....	44
4.3.2 Scanning Electron Microscope .....	45
4.3.2.1 Characterization using Scanning Electron Microscopy .....	45
4.3.3 X-Ray Diffraction (XRD).....	46

4.3.3.1 Characterisation using X-Ray Diffraction.....	47
4.3.4 Raman Spectroscopy .....	48
4.3.4.1 Characterisation using Raman spectroscopy .....	50
4.3.5 Ultraviolet-Visible Spectroscopy .....	50
4.3.5.1 Basic Principle.....	50
4.3.5.2 Working principle of the Ultraviolet-Visible spectroscopy .....	51
4.3.5.3 Characterisation using Ultra Violet – Visible Spectroscopy .....	52
4.3.6 The Hall Effect Measurement.....	52
4.3.6.1 Working principle of Hall Effect.....	53
4.3.7 Hall Effect Measurements .....	56
4.3.8 Electrical property measurements using a Four Point Probe.....	56
4.3.8.1 Characterisation using Four Point Probe Measurements.....	59
CHAPTER FIVE .....	60
RESULTS AND DISCUSSION.....	60
5.0 Introduction .....	60
5.1 Morphological Evaluation.....	60
5.1.1 Morphological Evaluation by Atomic Force Microscopy .....	60
5.1.2 Morphological Evaluation by Scanning Electron Microscopy (SEM).....	66
5.2 Structural Characterization.....	70

5.2.1 Structural Characterization by X-Ray Diffraction.....	70
5.2.2 Structural Characterization by Raman spectroscopy.....	72
5.3 Absorptionproperties.....	75
5.4 Charge Mobility Measurements.....	79
5.5Electrical Properties.....	80
CHAPTER SIX.....	83
CONCLUSIONS AND RECOMMENDATIONS.....	83
6.0 Introduction.....	83
6.1 Conclusions.....	83
6.2 Recommendations.....	84
REFERENCES:.....	86
APPENDIX:.....	97
Appendix A:.....	97
Appendix B:.....	98

## List of Figures

FIGURE 1: MANUFACTURING OF POLYMER SOLAR CELLS THROUGH ROLL-TO-ROLL PRINTING TECHNOLOGY' .....	6
FIGURE 2: POLYMERIC SOLAR CELL HETEROJUNCTIONS .....	9
FIGURE 3: TYPICAL CURRENT-VOLTAGE CHARACTERISTICS OF ORGANIC SOLAR CELLS IN DARK AND UNDER ILLUMINATION. ....	11
FIGURE 4: FUNDAMENTAL MECHANISM OF THE PHOTON-TO-ELECTRON CONVERSION PROCESS IN BULK HETEROJUNCTION SOLAR CELLS. ....	13
FIGURE 5: ENERGY BANDS AND BAND GAP OF PUSH/PULL POLYMER .....	14
FIGURE 6: POLYMER SOLAR CELL ARCHITECTURE .....	15
FIGURE 8: SCHEMATIC STRUCTURES OF PEDOT: PSS MIXTURE BEFORE AND AFTER SDS MODIFICATION. ....	21
FIGURE 9: SCHEMATIC STRUCTURES OF THE BENZOID AND QUINOID STRUCTURES .....	24
FIGURE 10: CHEMICAL STRUCTURE OF SODIUM DODECYL SULPHATE .....	25
FIGURE 11: FORMATION AND SPLITTING OF AN EXCITON IN AN ACTIVE LAYER OF BHJ SOLAR CELL .....	27
FIGURE 12: ORGANIC SOLAR CELL WITH AN HTL MATERIAL .....	33
FIGURE 13: SCHEMATIC STRUCTURE OF ATOMIC FORCE MICROSCOPY .....	44
FIGURE 14: SCHEMATIC DIAGRAM FOR RAMAN SPECTROSCOPY .....	48
FIGURE 15: ENERGY-LEVEL DIAGRAM SHOWING THE STATES INVOLVED IN RAMAN SPECTRUM .....	49
FIGURE 16: SIMPLIFIED SCHEMATIC OF A DOUBLE BEAM UV- VISIBLE SPECTROPHOTOMETER .....	52

FIGURE 17: THE HALL EFFECT MEASUREMENT SYSTEM AT UNIVERSITY OF DAR-ES-SALAAM .....	53
FIGURE 18: SCHEMATIC DIAGRAM SHOWING THE DIRECTION OF THE LORENTZ FORCE AND VELOCITY .....	54
FIGURE 19: PICTURE OF THE HALL EFFECT SAMPLE MOUNTING BOARD WITH FOUR OHMIC CONTACTSMOUNTED ON THE SAMPLE SPECIMEN. ....	56
FIGURE 20: SCHEMATIC STRUCTURE OF A FOUR POINT PROBE .....	57
FIGURE 21: AFM IMAGES OF PEDOT: PSS .....	62
FIGURE 22: AFM IMAGES SHOWING PHASE SEPARATION .....	63
FIGURE 24: FORMATION OF FACE-CENTERED CUBIC (FCC) .....	67
FIGURE 25: (A) FACE CENTERED CUBIC (FCC) NANOCRYSTAL, (B) NANOSOLDERING ..... STRUCTURES AND (C) FCC CRYSTAL STRUCTURES AT 2MM .....	69
FIGURE 26: XRD PATTERNS OF PEDOT: PSS DOPED WITH SDS AND CuNPs .....	70
FIGURE 27: XRD PATTERNS OF PEDOT: PSS DOPED WITH SDS AND CU NPS SHOWING (111)(130), (112) AND (202) FACETS. ....	71
FIGURE 28: RAMAN SPECTRA OF PEDOT: PSS, PEDOT: PSS: SDS AND..... PEDOT: PSS: SDS: CUNPs FILMS. ....	73
FIGURE 29: RAMAN SPECTRA OF PEDOT: PSS, PEDOT: PSS: SDS AND..... PEDOT: PSS: SDS: CUNPs FILMS .....	74
FIGURE 30: GRAPH OF ABSORBANCE AGAINST WAVELENGTH SHOWING THE ABSORBANCE FOR EACHDOPING LEVEL .....	75
FIGURE 31: COLUMN CHART SHOWING ABSORBANCE AT 950NM .....	76
FIGURE 32: GRAPH OF CONCENTRATION AGAINST MOBILITY .....	79
FIGURE 33: COLUMN CHART SHOWING CONDUCTIVITY OF PEDOT: PSS AFTER DOPING	

WITH SDS AND COPPER NANOPARTICLES.....81

## List of Tables

TABLE 1: CONDUCTIVITY IMPROVEMENT ON PEDOT:PSS .....	39
TABLE 2: TABLE OF ROUGHNESS VALUES AT DIFFERENT DOPING LEVELS .....	66
TABLE 3: CALCULATION OF THE DIFFRACTION ANGLES $\theta$ AND $\beta$ AT FULL WIDTH HALF MAXIMUM(FWHM) .....	72
TABLE 4: ANALYSIS OF THE OPTICAL PROPERTIES SHOWING A TREND IN THE MAXIMUM ABSORPTION PEAK, ABSORPTION REGION AND RANGE .....	78

## Appendix

### Appendix A

CALCULATION OF THE AVERAGE COPPER NANOPARTICLES CRYSTAL SIZE.....	97
---	----

### Appendix B

FIGURE 1: CURRENT-VOLTAGE CURVE FOR 0% SDS .....	98
FIGURE 2: CURRENT-VOLTAGE CURVE FOR 5% SDS .....	98
FIGURE 3: CURRENT-VOLTAGE CURVE FOR 10% SDS .....	99
FIGURE 4: CURRENT-VOLTAGE CURVE FOR 15% SDS .....	99
FIGURE 5: CURRENT-VOLTAGE CURVE FOR 20% SDS .....	100
FIGURE 6: CURRENT-VOLTAGE CURVE FOR 15% SDS AND CuNPs.....	100
TABLE 1: ERROR ANALYSIS IN CONDUCTIVITY VALUES FOR UNDOPE PEDOT: PSS.....	101
TABLE 2: ERROR ANALYSIS IN CONDUCTIVITY VALUES FOR 5% SDS .....	101
TABLE 3: ERROR ANALYSIS IN CONDUCTIVITY VALUES FOR 10% SDS .....	101
TABLE 4: ERROR ANALYSIS IN CONDUCTIVITY VALUES FOR 15% SDS .....	102
TABLE 5: ERROR ANALYSIS IN CONDUCTIVITY VALUES FOR 20% SDS .....	102
TABLE 6: ERROR ANALYSIS IN CONDUCTIVITY VALUES FOR 15% SDS + CuNPs.....	102

## List of Acronyms

AEY	Auger electron yield
AFM	Atomic force microscopy
Ag	Silver
Al	Aluminium
AM1.5	Air mass 1.5 Charge- coupled device
BHJ	Bulk heterojunction
CCD	Charge- coupled device
CdTe	Cadmium telluride
CIGS	Copper indium gallium selenide
CMC	Critical Micelle concentration
CuNPs	Copper Nanoparticles
CuNW	Copper nanowire
CuSO <sub>4</sub> .5H <sub>2</sub> O	Copper Sulphate Pentahydrate
DTS	Distributed temperature sensing
ECD	Electron Capture Dissociation
EELS	Electron energy loss spectroscopy
EG	Ethylene Glycol
EERG	Energy and Environmental Research Group
EQE	External quantum efficiency
ETL	Electron Transporting Layer
FCC	Face Centred Cubic

FF	Fill factor
FTO	Fluorinated tin oxide
FWHM	Full Width Half Maximum
GaInP	Gallium indium phosphide
Ge	Germanium
GMS	Glycerol Monostearate
HOMO	Highest occupied molecular orbital
HTL	Hole Transport Layer
ICP	Inductively coupled plasma
IQE	Internal quantum efficiency
ISP	International Science Program
ITO	Indium doped tin oxide
$J_{sc}$	Short circuit current density
LUMO	Lowest unoccupied molecular orbital
MDMO-PPV	Poly[2-methoxy-5-(3,7-dimethyloctyloxy)- 1,4phenylenevinylene]
MPP	Maximum power point
$NaBH_4$	Sodium Borohydrate
NaOH	Sodium Hydroxide
NEXAFS	Near-edge X-ray absorption fine structure
OFETs	organic field-effect transistors
OPV	Organic Photovoltaic
OSC	Organic solar cells

P3HT	Poly(3-hexylthiophene)
PCBM	[6,6]-phenyl-C61-butyric acid methyl ester
PC <sub>70</sub> BM	[6,6]-phenyl-C71-butyric acid methyl ester
PCDTBT	Poly[N-(1-octylnonyl)-2,7-carbazole]-alt-5,5-[4,7-di(thien-2yl)-2,1,3-benzothiadiazole]
PCE	Power conversion efficiency
PEDOT:PSS	Poly(3,4-ethylenedioxythiophene) polystyrene sulfonate
PET	Polyethylene terephthalate
PEY	Partial electron yield
PSC	Polymer Solar Cells
PV	Photovoltaic
SDS	Sodium Dodecyl Sulphate
SEM	Scanning electron microscopy/microscope
S/cm	Siemens per centimetre
Si	Silicon
SIMS	Secondary ion mass spectrometry
STM	Scanning tunnelling microscopy
STXM	Scanning transmission X-ray microscopy
TCE	Transparent conducting electrode
TEM	Transmission electron microscopy/microscope
TEY	Total electron yield
TQ1	Poly[2,3-bis-(3-octyloxyphenyl)quinoxaline-5,8-

diyl-altthiophene-2,5-diyl]

UPS	Ultraviolet photoelectron spectroscopy
UV-Vis	Ultraviolet visible spectroscopy
$V_{oc}$	Open circuit voltage
XRD	X-Ray Diffraction
XPS	X-ray photoelectron spectroscopy

# CHAPTER ONE

## INTRODUCTION

### 1.0 Background

The discovery of the photovoltaic effect in silicon (Si) diodes in 1954 marked the dawn of the era of modern solid-state photovoltaic (PV) technology. Currently, crystalline silicon and various inorganic thin-film solar cells are the dominant photovoltaic technologies, with the lab efficiency of the crystalline silicon solar cells at 24.7%<sup>[1,2]</sup>. The crystalline silicon solar cells also known as conventional, traditional or wafer based cells are the first generation solar cells. Even though the first generation solar cell has high efficiency, it has a high cost of production. Hence, came the thin film solar cells, the second generation solar cells that included amorphous silicon, cadmium telluride (CdTe) and copper indium gallium selenide (CIGS) cells. The purpose of the thin film solar cells was to reduce the costs by eliminating the costs of the silicon wafer and increase in the size of the unit of manufacturing from that of a silicon wafer to that of a glass sheet, about 100 times larger in area<sup>[3]</sup>. Reducing the cost of the solar cells came at the expense of low efficiency, which led to the development of the next generation solar cells, in search for high efficiency. Commercial uptake of these solar cells had issues such as low efficiencies and instability. This prompted research for new materials to produce low cost, high-efficiency solar cells<sup>[3]</sup>. The need to develop cheaper renewable energy sources stimulated scientific research for an efficient, low-cost photovoltaic device which led to the discovery of polymer solar cells.

The steady improvement in energy conversion efficiency during the past decades led to organic photovoltaic (OPV) evolving into a promising technology for renewable energy. Polymer Solar Cells (PSCs) have attracted significant attention due to the advantages of lightweight, flexibility and low cost with the possibility of fabricating large area device by liquid base processing<sup>[4],[5]</sup>. Compared with inorganic solar cells, organic solar cells have several advantages, including low-cost processing, mechanical flexibility<sup>[6]</sup>, and broad spectral and energy level tunability. Organic materials used in PSCs can be solution processed at low cost, allowing large-area deposition on flexible substrates through roll-to-roll or contact printing technologies<sup>[7]</sup>. Organic materials are therefore promising candidates for large-area and flexible processing of transparent electrodes which are essential components for optoelectronic devices and photovoltaic equipment, such as touch panels, organic light-emitting diodes, solar cells and flexible devices<sup>[8]</sup>. However, organic materials intended for use in PSCs have drawbacks such as low carrier densities and low charge mobilities, which limit their properties as transparent electrodes<sup>[9]</sup>. A well-known transparent electrode based on organic material is poly(3,4-ethylene dioxythiophene) doped with polystyrene sulfonic acid (PEDOT: PSS)<sup>[10]</sup>.

On the other hand, Indium tin oxide (ITO) is widely used as a transparent electrode in optoelectronic devices because it has high transparency and low resistance, but it is expensive to process. One advantage of organic solar cells is their being light in weight and flexible. The use of ITO in the cell architecture make the cell brittle and mechanically rigid.

The limitation in the cost of production of PSCs and indium scarcity has led to the low-cost replacement for the commercial feasibility of PSCs. The other disadvantage of ITO

is that its mechanical flexibility is limited and cracks occur when subjected to stress<sup>[11]</sup>. These cracks usually induce defects in the electrode and the other layers of the solar cell when exposed to water and moisture. The acidic and hygroscopic characteristics of PEDOT: PSS can cause indium loss from the ITO transparent anode when exposed to water, adversely affecting the device stability<sup>[12]</sup>.

### **1.1 Statement of the problem**

There is a need to replace ITO as a transparent conducting electrode because it is mechanically rigid and fragile for use in PSC where the significant advantage is flexibility. Furthermore, ITO adds to the cost of polymer solar cells due to the high cost of processing, and with the indium scarcity, it is anticipated that the prices will continue to rise on the world market. PEDOT: PSS is a viable potential to be used as a transparent conducting electrode for the ITO free solar cells. In its pristine form, PEDOT:PSS has a much lower conductivity than ITO and is therefore not a suitable replacement of ITO as transparent conducting oxide in PSC. PEDOT: PSS absorbs nearly 20% of the incident radiation intended for the active layer, to make it more practical, its transparency needs to be increased beyond 80 %.

### **1.2 Objectives**

#### **1.2.1 Main Objective**

The main objective of this study was to enhance the electrical properties of PEDOT: PSS by doping using sodium dodecyl sulphate and copper nanoparticles.

### **1.2.2 Specific objectives**

The objectives of the study were to:

- (i) develop PEDOT: PSS thin films with different surfactant loading levels,
- (ii) evaluate the optical, electrical and morphological characteristics of PEDOT:PSS: SDS and PEDOT:PSS:SDS: CuNPs doped thin films, and
- (iii) determine the charge mobility of the PEDOT:PSS: SDS thin films.

### **1.3 Research questions**

- (i) What is the highest conductivity of PEDOT: PSS that can be attained after doping?
- (ii) What are the achievable optimal optical and electrical properties after doping PEDOT:PSS using SDS and Copper Nanoparticles?

### **1.5 Significance of the Study**

Two main advantages of polymer solar cells are their flexibility and light-weight. However, the use of ITO as the TCE results in mechanical rigidity and more weight. Additionally, ITO also increases the cost of polymer solar cells. The enhanced electrical conductivity of PEDOT: PSS to near that of ITO will allow the replacement or avoidance of using ITO as a TCE. Furthermore, the reduction in light absorption will allow more light to reach the active layer leading to enhanced conductivity and facilitation of charge (hole transport) mobility. It is anticipated that the improved optical and electrical properties will translate into higher photoconversion efficiencies. Coupled with the advantages of weight, cost and

flexibility, a better and cheaper material will be available to replace the expensive ITO for use in solar cells as a TEC.

# CHAPTER TWO

## THEORETICAL BACKGROUND

### 2.0 Introduction

The development of polymer solar cells marked one of the new dawns for another form of clean energy sources. Polymer solar cells have attracted so much attention because they can be manufactured on plastic substrates by a variety of printing techniques<sup>[13],[14]</sup>. In polymer solar cells, the active materials used for the fabrication of devices are the soluble organic solvents. Hence, Polymer solar cells have the potential to be manufactured as flexible devices in a continuous roll-to-roll printing process as illustrated in Figure 1.

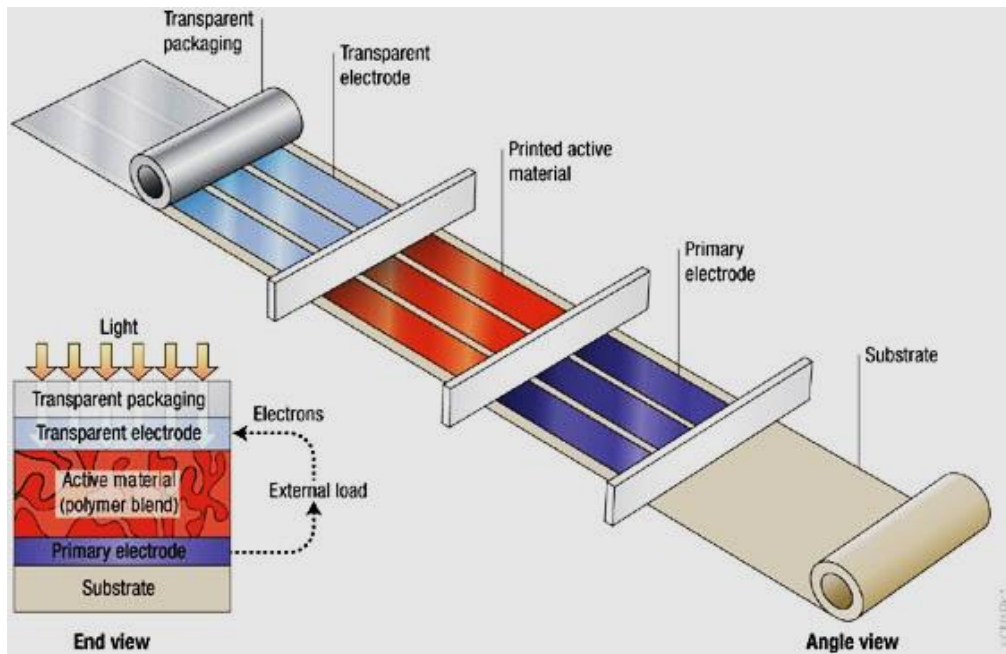


**Figure 1:** Manufacturing of Polymer Solar Cells through roll-to-roll printing technology<sup>[13]</sup>

Polymer solar cells are organic solar cells because they incorporate organic materials. An organic solar cell is a photovoltaic device that uses organic electronics or natural materials such as small molecules and polymers to convert solar energy into electrical energy<sup>[15]</sup>. The first process is the absorption of a photon leading to the formation of an excited state, that is, a bound electron-hole pair (exciton) creation; secondly, the exciton diffuses to a region where exciton dissociation (charge separation) occurs; and lastly is the movement of charge within the organic solar cell to the respective electrodes<sup>[14]</sup>. The organic molecules absorb light and induce transport of electrical charges between the conduction band of the absorber and the conduction band of the acceptor molecule. Organic photovoltaic cells are made of an electron acceptor and electron donor materials rather than semiconductor  $p - n$  junctions as in semiconductor photovoltaic cells. The particles that form the electron-donor region of organic PV cells, where exciton electron-hole pairs are generated, are mainly conjugated polymers possessing delocalized  $\pi$  electrons that result from carbon  $p$  orbital hybridisation<sup>[10]</sup>. The  $\pi$  electrons are excited by the light in or near the visible spectrum from Highest Occupied Molecular Orbital (HOMO) to the Lowest Unoccupied Molecular Orbital (LUMO) of the molecules, denoted by a  $\pi - \pi^*$  transition. The bandgap energy between these orbitals determines which wavelength of light will be absorbed<sup>[16]</sup>. Semiconductor photovoltaic cells use the energy absorbed by photons to generate free charge carriers (holes and electrons) which can do electrical work. Organic photovoltaic cells are photovoltaic devices that accomplish this conversion of energy using organic materials<sup>[17]</sup>. To efficiently accomplish the conversion of energy absorbed by photons using organic materials, a bilayer arrangement is required. In a bilayer arrangement, there are two layers in between the conductive electrodes. Electrostatic forces are generated at the

interface between the two layers because of their electron affinities and ionisation energies. The difference in the electron affinities and ionisation energies splits the excitons more efficiently as compared to a single layer organic photovoltaic cell. The layer with higher electron affinity and ionisation potential is known as the electron acceptor, and the layer with lower electron affinity and ionisation potential is the electron donor. Such a structural arrangement is also called a planar donor-acceptor heterojunction<sup>[14]</sup>.

A planar heterojunction is the most straightforward device that promotes exciton separation, embedded between a transparent conductor such as ITO coated with PEDOT: PSS or fluorinated tin oxide (FTO) and a reflecting metal (usually Al or Ag)<sup>[18]</sup> as shown in Figure 2b. In bulk heterojunction polymer solar cells, the light generates an exciton which is followed by charge separation. The bound excitons migrate to the interface with a significant drop in chemical potential energy to drive dissociation into an electron-hole pair that spans the interface across the donor and acceptor (Figure 2a). The first heterojunction to be formed was a bilayer architecture shown in Figure 2b, but this architecture was limited as the active layer must be thin to utilise all excitons. In order to separate an exciton, a heterojunction should exist within the exciton diffusion length. This can be achieved in a bulk heterojunction (Figure 2c) or an ordered heterojunction<sup>[18]</sup> (Figure 2d).

The bulk heterojunction (BHJ) (Fig. 2c) is a very successful device architecture for polymer photovoltaics because the exciton harvesting is made near-perfect by creating a highly folded architecture such that all excitons are formed near a heterojunction<sup>[19]</sup>. BHJs are formed by spin-coating the polymer and an electron acceptor from a universal

solvent. Common acceptors used in polymer BHJs are fullerenes, polymers, and *n*-type inorganic nanoparticles<sup>[20]</sup>.

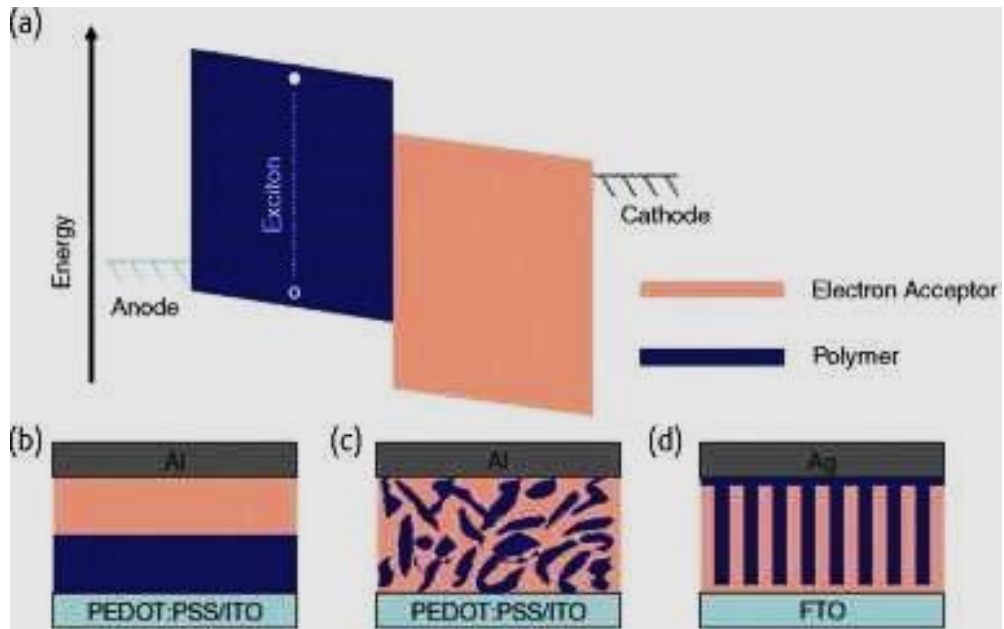


**Figure 2:** Polymeric solar cell heterojunctions: (a) Energy diagram of a Heterojunction with an exciton in the polymer phase. (b) Bilayer heterojunction. (c) Bulk heterojunction. (d) Ordered heterojunction.<sup>[20]</sup>

In order to achieve efficient polymer photovoltaics in bulk heterojunction solar cells the domain sizes of the donor and acceptor must be small compared to the distance the excitons must migrate to allow efficient exciton harvesting before natural exciton decay. The electrochemical potential drop at the donor-acceptor interface must be sufficient to dissociate excitons and the carrier transport rate must be fast as compared to the back-transfer rate. The geminated pair must split before the transfer of the electron from the acceptor to the donor. Hence the hopping rate is proportional to the carrier mobility since much work is done to modify the interfacial back-transfer rate.

Photogeneration of the electron-hole pairs in the light-harvesting material, followed by accumulation of the charge carriers at the collecting electrodes, gives rise to the difference of potentials between the electrodes<sup>[21]</sup>. Three parameters used to evaluate the performance of polymer solar cells are: open-circuit voltage ( $V_{oc}$ ), short circuit current density ( $J_{sc}$ ) and fill factor ( $FF$ )<sup>[22]</sup>. Short-circuit current ( $J_{sc}$ ) is the current reaching the contacts with no applied field and open-circuit voltage ( $V_{oc}$ ) is the maximum potential generated by the device. The ratio of the maximum power generated to the product of  $J_{sc}$  and  $V_{oc}$  is known as Fill Factor and is related to the quality of the device<sup>[19]</sup>. In polymer solar cells, device characteristics such as fill factor ( $FF$ ), short-circuit current density ( $J_{sc}$ ) and open-circuit voltage ( $V_{oc}$ ), as well as the cell lifetime are all highly dependent on the interface properties of the electrodes and the active layers and the bulk properties of the materials. For these reasons, numerous modifications of electrodes by the introduction of an interfacial layer have been studied intensively for high-performance and stable organic solar cells (OSCs). Several key factors such as transparency, conductivity, passivation property, film morphology, stability, and solution-processability considered for uses of these promising interfacial layers are areas of active research.<sup>[23]</sup>

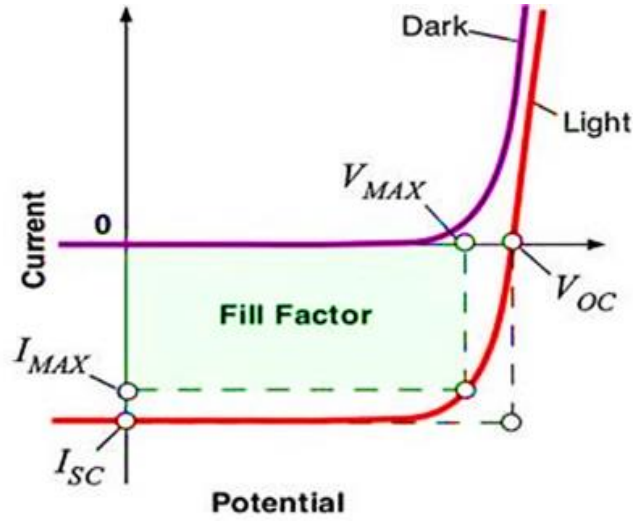


**Figure 3:** Typical current-voltage characteristics of organic solar cells in dark and under Illumination<sup>[17]</sup>.

For a photon-to-electron conversion process in polymer solar cells, the external quantum efficiency (EQE) is defined as the ratio between the photogenerated charges at the electrodes to the number of the incident photons at a particular wavelength (i.e., EQE is a function of wavelength), in terms of energy<sup>[22]</sup>. The expression for EQE is given in equation (1).

$$EQE(\lambda) = \eta_A(\lambda) \times \eta_{ED}(\lambda) \times \eta_{CS}(\lambda) \times \eta_{CC}(\lambda) \quad (1)$$

where  $\lambda$  is the wavelength of incident light, and efficiencies  $\eta_A$  is absorption efficiency,  $\eta_{ED}$  is exciton diffusion efficiency,  $\eta_{CS}$  is charge separation efficiency, and  $\eta_{CC}$  is charge collection efficiency<sup>[24]</sup>. The power conversion efficiency (PCE), (%), of a photovoltaic device, is defined by the equation (2).

$$\eta = (J_{sc} \times V_{oc} \times FF) / (P_{in}) \quad (2)$$

where  $J_{sc}$ ,  $V_{oc}$ ,  $FF$ , and  $P_{in}$  are the short-circuit current density, open-circuit voltage, fill factor, and power of incident light, respectively. The value of  $J_{sc}$  is influenced by the breadth of the light absorption spectrum (determined mainly by the band gap), the extent of light absorption (determined by the thickness of the active layer), and the morphology of the active layer. Theoretically, the  $J_{sc}$  is defined by equation (3).

$$J_{sc} = \frac{hc}{q} \int \frac{P_{sun}(\lambda) \cdot EQE(\lambda)}{\lambda} d\lambda \quad (3)$$

Where  $P_{sun}$  represents the solar spectrum,  $q$  is the elementary charge,  $h$  is Planck's constant,  $\lambda$  is the wavelength and  $c$  is the speed of light.

The open-circuit voltage ( $V_{oc}$ ) is the maximum potential at which there is no current. Theoretically, the value of  $V_{oc}$  is linearly proportional to the difference in energy levels between the HOMO of the donor and the LUMO of the acceptor. Therefore, to increase the value of  $V_{oc}$ , one can either lower the HOMO of the donor or raise the LUMO of the acceptor. Hence, the value of  $V_{oc}$  is determined principally by the properties of the material of the donor and acceptor in the active layer, although different cathode materials also affect the  $V_{oc}$ . The Fill Factor is sensitive to competition between photocurrent generation and charge recombination and therefore significantly impacted by the morphology of the active layer<sup>[25]</sup>.

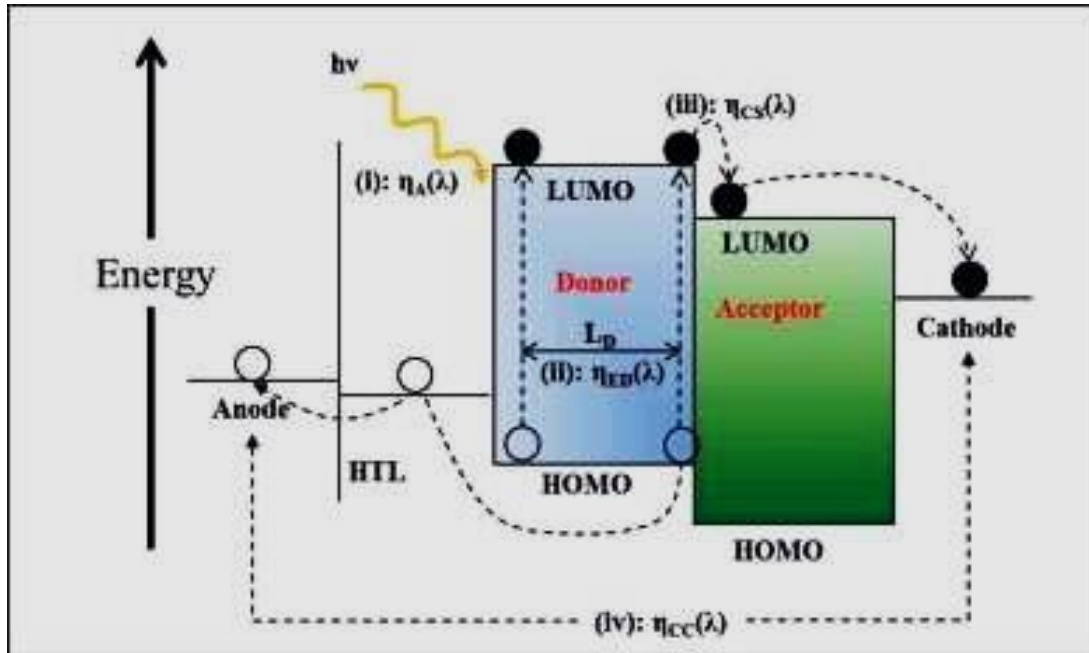


**Figure 4:** Fundamental mechanism of the photon-to-electron conversion process in Bulk Heterojunction solar cells.<sup>[26]</sup>

The relatively low values of  $J_{sc}$  for OPVs arise mainly from the larger optical band gaps of the organic molecules used, typically 1.5–2eV (1.1eV for silicon). Therefore, there is a need for low bandgap organic semiconductors with light absorption that extends further into the infrared (IR) to lower the bandgap. Three basic units describe the architecture of the conjugated polymer: its backbone repeating groups, side chains, and substituents. The backbone of repeating units consisting of the conjugated chains determine the HOMO and LUMO energy levels and the bandgap of the polymer. Low bandgap polymers usually used as the donor materials and fullerene derivatives such as PC<sub>71</sub>BM could widely be adopted as the acceptor component given their relatively high electron affinity and charge carrier mobility.

For conjugated polymers to be used in OPVs, they need to exhibit low bandgaps to broaden the absorption range; crystalline characteristics to ensure good charge mobility; low HOMO energy levels enhance the values of  $V_{oc}$ ; and suitable LUMO energy levels for efficient electron transfer to the fullerene moieties. The electron push and pull of molecular units in conjugated polymer chains is the most successful strategy for harvesting more photons. The alternating push and pull of units allow the internal charge transfer process along the conjugated chain to increase the effective resonance length of the  $\pi$  electrons which leads to smaller bandgaps as a result of facilitated  $\pi$  electron delocalization through planarization.

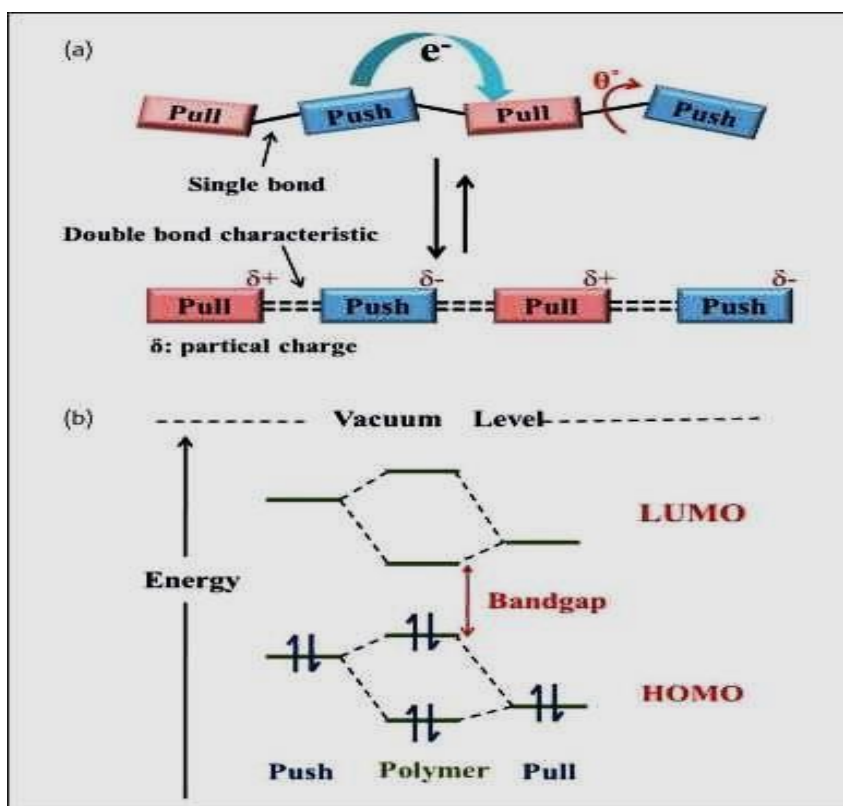


**Figure 5:** Energy Bands and Band gap of push/pull polymer(a) the delocalisation of  $\pi$  electrons and (b) the energy bands of push and pull units and the bandgap of a push/pull polymer. <sup>[26]</sup>

## 2.1 Theoretical Background of Polymer Solar Cells

The Polymer solar cell architecture consists of top glass with conductive electrode and a hole transporting layer followed by an active layer and a metal electrode. An example of such an architecture is shown in Figure 6 with an indium tin oxide (ITO) as conductive glass on top followed by PEDOT:PSS as the electron or hole blocking layer, an active layer which contains the electron acceptor and an electron donor and aluminium as the metal electrode on top.

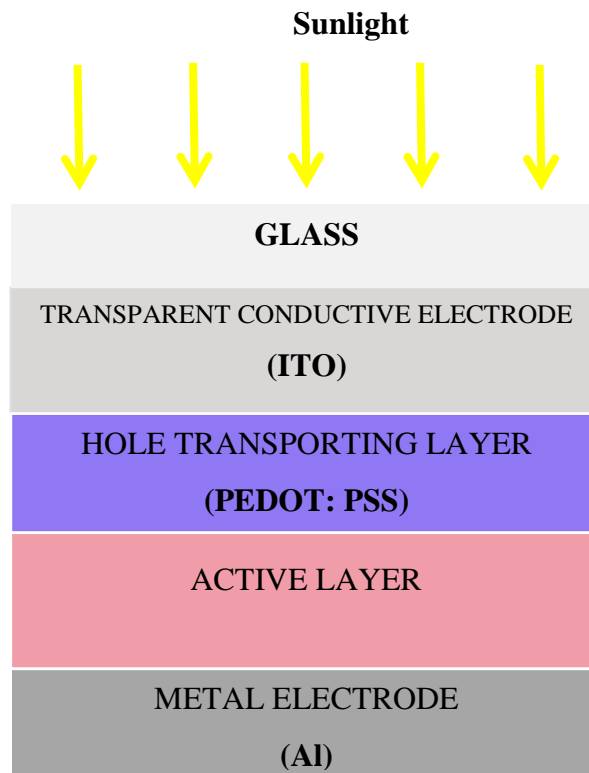


**Figure 6:** Polymer solar cell architecture

The order and nature of the blocking layers, as well as the quality of the metal electrode, depends on the architecture of the solar cell. In this architecture, the ITO absorbs the

light that is transmitted to the active layer where charge dissociation occurs. The separated charges are then transported to the respective electrodes through the hole transporting layer and electron transporting layer.

### **2.1.1 Transparent Conductive Electrode**

Transparent conductive electrodes are electrodes of optically transparent and electrically conductive material. ITO is used as a transparent conducting electrode because it has high conductivity and good optical properties. ITO is a heavily doped semiconductor, essentially indium oxide ( $\text{In}_2\text{O}_3$ ), containing high density donors of tin ( $10^{20}$  to  $10^{21} \text{ cm}^{-3}$ )<sup>[27]</sup>. The high density carrier increases the conductivity to levels of metallic conduction. ITO has high conductivity due to the electrons that are donated by the conduction band. The free carriers in the conduction band are excited to higher-energy levels inside the conduction band and then rapidly fall back to the bottom of the conduction band. The absorption of infrared radiation by the free carriers leads to high level of optical absorption. However, ITO does not have an optical band gap, instead, it has a large electronic band gap which makes it transparent to visible light. The undoped  $\text{In}_2\text{O}_3$  behaves as an insulator with an optical band gap of about 3.5eV. Hence this determines the optical properties of the ITO at higher photon energy levels<sup>[28]</sup>.

### **2.1.2 PEDOT: PSS as a Hole Transporting Layer (HTL)**

The hole transporting layer must have a valence band higher than that of the absorber and to extract holes from the absorber. It must have a higher conduction band than that of the absorber to reject the electrons. In polymer solar cells heterojunction, the hole transporting layer is used to transport holes to the anode. The hole transporting layer works in conjunction with an Electron Transporting layer. An Electron transporting layer is a material that transports electrons to the cathode. If a hole transporting layer is present, electrons cannot reach the anode<sup>[29]</sup>. The hole transporting layer and electron transporting layer prevents charge recombination. The hole transporting layer and electron transporting layer have much higher charge transporting properties compared with the active materials. The charges that reach the interfaces with the hole transporting layer and electron transporting layer can quickly move away from the active layer<sup>[30]</sup>. In this way, charge recombination is efficiently blocked as charges that recombine cannot be collected.

### **2.1.3 Active Layer**

The active layer is the photoactive material that is used to harvest light. Since the active layer harvests light, it has the function of photon absorption and generation of excitons. The photon absorption and generation of excitons are bound by the electron hole pairs. To achieve the photovoltaic effect in organic materials, the electron must be separated from holes in the excitons. The separation of electron from a hole is mainly done by dissociation which can only be achieved by setting the potential energy gradients at the sides of the active layer. One side can be set as the hole transporting layer (HTL) for holes and the other side as electron transporting layer(ETL), for electrons. The HTL and

ETL are used as charge separators. To effectively dissociate the electrons and holes from the excitons and transport them to the cathode and anode, the transporting layers must have a conduction band lower than that of the absorber so that all the electrons are extracted from the excitons reaching the active layer. The separation of the electrons from the excitons is done in conjunction with the rejection of the holes by the electron transporting layer. For the electron transporting layer to effectively reject the holes, it must have a valence band lower than that of the absorber<sup>[28]</sup>.

#### **2.1.4 Metal Electrode.**

Aluminium metal is often used as the top electrode in polymer solar cells because it has a low workfunction and in some cases calcium metal can also be used because it has similar properties with aluminium. These metals are found to be highly reactive to oxidation and easily form oxides with insulating properties. The formation of oxides form barriers to charge extraction that reduce charge recombination by blocking the charges<sup>[24]</sup>.

#### **2.2 Conducting Polymers**

Conducting polymers are polymers with the ability to conduct charge.<sup>[31]</sup> These polymers have attracted attention because of their electronic, optical, and mechanical properties that can be fine tuned by the synthesis or doping methods. Conducting Polymers (CP) like polyaniline, polypyrrole, polythiophene have attracted attention due to their good electrical and optical properties<sup>[32]</sup>. These polymers have metallic-like properties with high conductivity and can be considered as semiconductors.<sup>[33]</sup> However, the polymers have drawbacks such as lower conductivity and reduced transparency as compared to

some commercially available solar cell materials. Polyaniline and polypyrrole are conducting polymers with high conductivity but lack properties of solubility and processibility. Polythiophene and PEDOT have become more popular due to the higher stability of polythiophene and its derivatives and the resistance to degradation<sup>[41]</sup>. Polythiophene and its derivatives are stable both in their doped and undoped states and exhibit high stability of the optical spectrum and high conductivity retention at elevated temperatures for long intervals <sup>[32]</sup>. PEDOT: PSS is polythiophene derivative with exceptional optical, conductive and solubility properties.

### **2.2.1 PEDOT: PSS**

PEDOT: PSS is a conducting polymer that used as a hole transporting layer in polymer solar cells. PEDOT: PSS consists of two polymers PEDOT which is conjugated and conducting with PSS as a counter ion. PSS is a saturated polymer and is non conducting. PEDOT is hydrophobic leading to poor solubility in aqueous environment. PSS on the other hand is hydrophilic and facilitates the solubility of PEDOT. PEDOT carries a positive charge based on polythiophene while PSS, a sulfonated polystyrene that carries a negative charge. The two charged macromolecules together make a macromolecular salt called PEDOT: PSS shown in Figure 7.

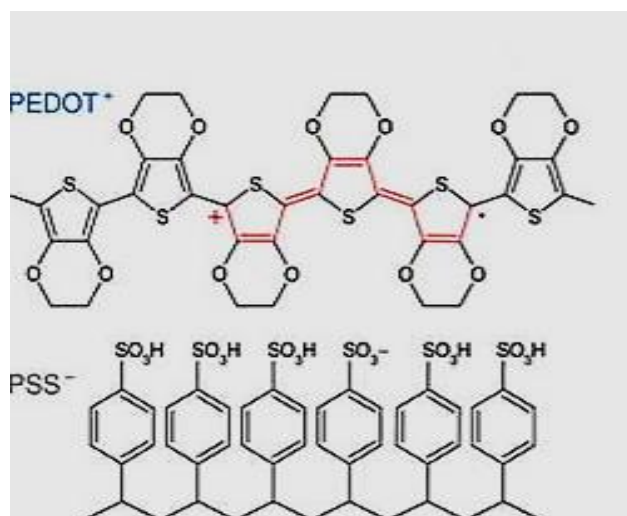


**Figure 7:** Chemical structure of PEDOT: PSS<sup>[34]</sup>

The polymer PEDOT: PSS sits at the interface of ITO and the active layer of a polymer solar cell. In a polymer solar cell, PEDOT: PSS is used as a hole extracting layer (HEL)<sup>[35]</sup> where its function is to transport holes to the anode. For a polymer solar cell, increased roughness of PEDOT: PSS films increases the contact area within the active layer facilitating more charge transfer which is an advantage to the device performance.

The pristine PEDOT: PSS consists of grains with a hydrophobic and highly conductive PEDOT-rich core and a hydrophilic insulating PSS-rich shell. The inclusion of ionic surfactants weakens the Coulomb attraction between PEDOT: PSS and phase separation between hydrophobic PEDOT and hydrophilic PSS chains occurs. Furthermore, the interaction between ionic surfactant and PEDOT and PSS chains enable the reorientation of the PEDOT chains by getting away from PSS chains coils allowing more inter-chain interactions among PEDOT components. Thus, the energy barrier for interchain and inter-domain charge hopping lowers and charge transfer among the PEDOT chains would become faster, leading to a significant enhancement of the

conductivity of PEDOT: PSS film<sup>[11]</sup>. Morphological studies of the optimal phase separation and different fabrication methods have been pursued by different scientific researchers<sup>[36]</sup>. Figure 8 shows the separation of the PEDOT from the PSS chains after SDS modification.

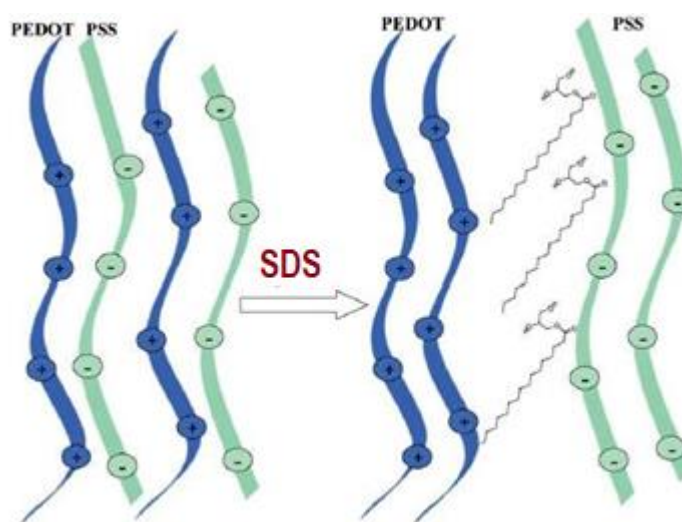


**Figure 8:** Schematic structures of PEDOT: PSS mixture before and after SDS Modification.<sup>[37]</sup>

PEDOT: PSS has high optical transparency in the visible light spectrum and the high work function (4.8–5.2 eV) which facilitates the formation of an Ohmic contact with many universal polymer donors, with which PEDOT: PSS behaves like a good HTL material that can be solution processed. PEDOT is used as a transparent, conductive polymer in OLEDs and organic transistors because of its high electrical conductivity (up to 500 S/cm) and excellent thermal and chemical stability. However, PEDOT alone is insoluble and difficult to process; hence it is blended with polystyrene sulfonic acid, (PSS), which serves as the charge-balancing dopant during polymerisation<sup>[38]</sup>. The

PEDOT: PSS blend is found to form a highly stable dispersion in water with improved ease of processing. In this complex, oligomeric PEDOT segments are tightly attached to PSS chains using electrostatic forces. The combination results in a water-dispersed polyelectrolyte system with reasonably good film-forming properties and excellent thermal stability<sup>[39]</sup>. However, the blending of PEDOT: PSS is at the expense of low conductivity (1S/cm), which is saliently lower than that of ITO<sup>[40]</sup>. If organic compounds, including high boiling solvents like methyl pyrrolidone, dimethyl sulfoxide, sorbitol, ionic liquids, and surfactants, are added, conductivity increases by many orders of magnitude. The increase in conductivity makes the PEDOT: PSS suitable as a transparent electrode, for flexible organic solar cells<sup>[32]</sup> to replace the traditionally used indium tin oxide (ITO), owing to the high conductivity of 4600 S/cm. PEDOT: PSS films have high transparency in the visible range, high mechanical flexibility, and excellent thermal stability. Doped PEDOT: PSS has been used widely for depositing thin, transparent films for use as an electrode in electronics applications<sup>[32]</sup>.

PEDOT: PSS thin films can be quickly deposited using different techniques like template synthesis, chemical vacuum deposition (CVD), spin coating, inkjet printing, electro-polymerisation, and spraying. PEDOT: PSS is a low bandgap *p*-type semiconducting material with its energy gap lying in the visible-near IR range (1.6 eV for  $\pi$ - $\pi^*$  transition) and shows an absorption maximum in the middle of the visible spectrum at 600 nm. Doped PEDOT: PSS is almost transparent in the visible region (with a light blue tint) and while neutral polymer possesses a blue-black colour. In its pristine state, a film of PEDOT-PSS consists of a mixture of undoped and doped

PEDOT units in the ratio 1:4, corresponding to an intermediate state between the fully doped (oxidised) and undoped (reduced) state. Electrochemical doping of PEDOT: PSS results in the addition of bandgap energy levels, producing absorptive transitions in the visible region that invoke an observable colour change. This high contrast electrochromic phenomenon associated with electrochemical doping and the corresponding changes in the absorption spectrum is of particular interest to understand the charge storage mechanism during doping/developing process. Whenever electrochemical doping takes place, ions are incorporated into or extracted from the PEDOT: PSS film. This incorporation of ions manifests itself in the form of an increase in electrical conductivity. The conductivity increase in these materials arises from the introduction of polaronic and bipolaronic species on the polymer backbone <sup>[32]</sup>, which are charge compensated by a counter ion. The formation of the polarons is believed to originate from the expanding polymers chains and conformational changes from benzoid to quinoid forms as shown in Figure 9. The presence of these charged molecular defects introduce symmetric mid-band gap energy states. At higher doping levels, broad bipolaron bands develop, effectively minimising the bandgap and moving the material into a quasi-metallic regime. This electrochromic behaviour brought about by electron transfer reaction that takes place during the electrochemical oxidation and reduction of the polymer makes PEDOT: PSS suitable as a cathodically colouring polymer in the construction of ECDs.

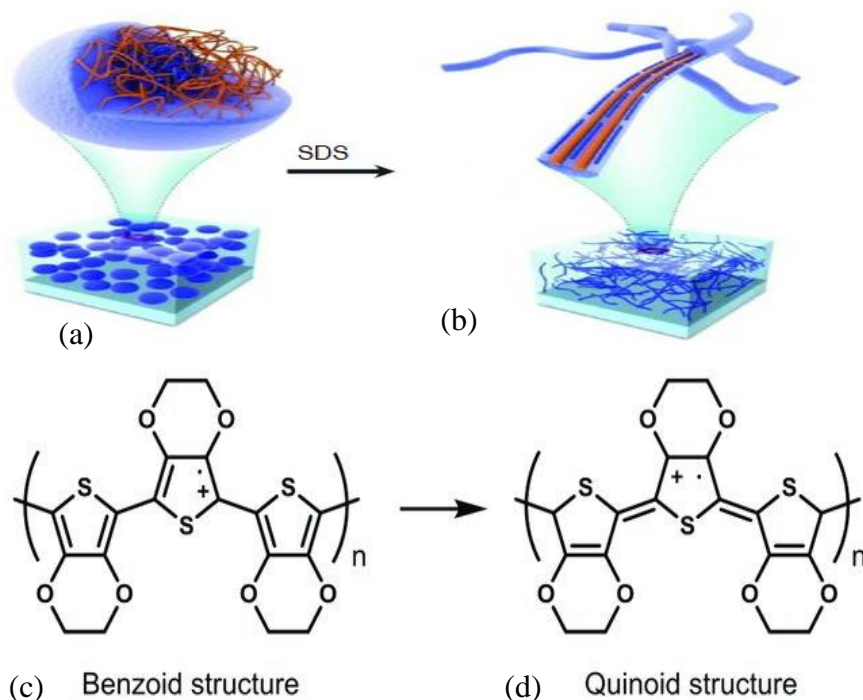


**Figure 9:** Schematic structures of the benzoid and quinoid structures  
 (a) Coiled PEDOT: PSS structures before adding SDS in benzoid form  
 (b) Expanded PEDOT: PSS structures after adding in quinoid form  
 (c) Benzoid structure (d) Quinoid structure <sup>[34]</sup>

### 2.3 Sodium Dodecyl Sulfate (SDS)

The sodium dodecyl sulfate (SDS) is used as one of the surfactants to improve the electrical, optical, and structural properties of PEDOT: PSS. A surfactant is an active agent that can lower the surface tension between two liquids, between a gas and a liquid or between a liquid and a solid. The structural formula is shown in Figure 10. It consists of a hydrophobic tail and a polar group.



**Figure 10:** Chemical Structure of Sodium Dodecyl Sulphate

SDS shows hydrophobic properties when the contact angle with water is high and has hydrophilic properties when the contact angle with water is low. Hence, its polar parts are associated with water while the non-polar parts are segregated away. SDS molecules can cluster together as micelles when they are present above a certain concentration called the critical micelle concentration<sup>[41]</sup>. The SDS critical micelle concentration (CMC) in pure water at 25 °C is 8.2 mM, and the aggregation number at that concentration is at 62. Critical micelle concentration is the transition concentration of a surfactant in the bulk phase at which molecules aggregate to form micelles<sup>[38]</sup>.

#### **2.4 Charge Transportation in Polymer Solar Cells**

Charge carriers in polymers are polarons and bipolarons. A polaron is a quasiparticle that results when an electron (or hole) in the conduction band of a crystalline polymer or semiconductor polarizes the lattice in its vicinity. A bipolaron is a quasiparticle consisting of two polarons. Polarons are used in condensed matter physics to understand the interactions between electrons and atoms in solid materials<sup>[27]</sup>.

To understand charge transport in organic molecules, it is important to elaborate on the electronic structure. Organic molecules are made of molecular subunits. These hydrocarbon molecules have a backbone of carbon atoms. The strong bonds forming the molecular backbone come from  $sp_2$  hybridized atomic orbitals of adjacent carbon atoms that overlap to yield bonding  $s$  and antibonding  $s^*$  molecular orbitals. The remaining  $p_z$  orbitals overlap resulting  $p$  and  $p^*$  orbitals with less binding or antibinding energies. In the ground state of the molecule, the bonding orbitals up to the HOMO are filled with two electrons of antiparallel spin. The antibonding orbitals from the LUMO are empty. When light is absorbed by a molecule, an electron is promoted from HOMO to the LUMO, forming electron-hole pairs known as excitons<sup>[42]</sup>. The excitons then diffuse into an interfacial layer, where the difference in the work function exists to avoid charge recombination. The diffusion is then followed by the charge separation between an electron donor and acceptor blend within the interface of the devices' active layer<sup>[43]</sup>. The charges are then transported to the device's electrode where the charges flow outside the cell to perform work and then re-enter the device on the opposite side. To minimise charge recombination as well as enhance power conversion efficiency (PEC), it is essential to blend the conducting polymer with electron acceptor material such as fullerene. The blending process creates an interface between the donor material and the acceptor material. Across this donor-acceptor interface, a sizeable HOMO-LUMO energy level is offset to produce a large internal electric field gradient capable of splitting the exciton into free electrons and holes. This kind of photovoltaic devices containing a blend of donor-acceptor materials is also known as a bulk hetero-junction [BHJ] solar cell, schematically shown in Figure 11. A donor is a material with low electron affinity while an acceptor is a material with high electron affinity.

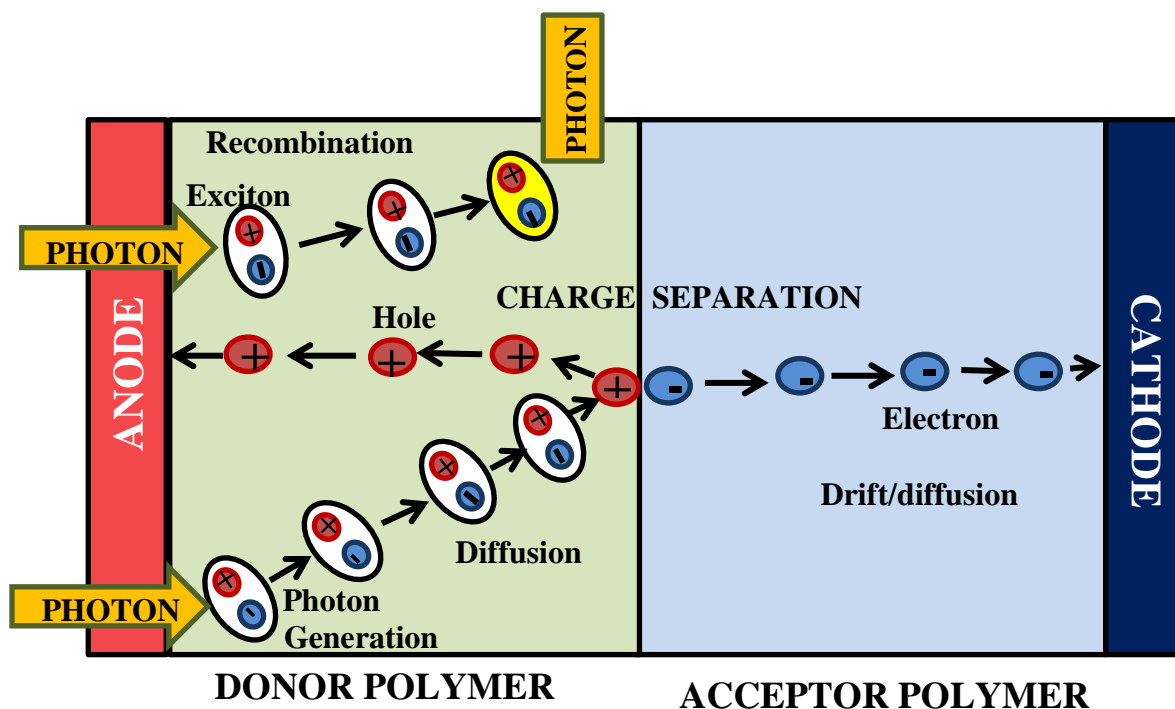


**Figure 11:** Formation and splitting of an exciton in an active layer of BHJ solar cell

The charged pair formed after exciton dissociation, a geminate pair, is often still coulombically bound and must be dissociated by an internal field. After separation, each charge carrier must be transported through the device to the appropriate contact while avoiding traps and recombination. These charges are carried primarily by drift caused by the built-in field, though diffusion can play a significant role. The exciton diffusion length limits the efficiency of the planar heterojunction device. Excitons travel distance of  $\sim 3^{-10}$  nm in most organic semiconductors before undergoing recombination. The excitons formed at a distant location from the heterojunction than the exciton diffusion length, have a lower probability of being harvested.<sup>[19]</sup>

## 2.5 Charge Mobility

Charge mobility is an important parameter for polymer solar cells. Charge mobility influences the extraction and recombination of charges at the donor and acceptor interface layers. The operation of a polymer solar cell is based on light absorption, charge separation and charge transport to the electrodes. During the transport of charges, recombination can occur which can reduce the power conversion efficiency. The rate at which the recombination occurs is determined by the mobility and density of electrons and holes.

The electron and hole mobility are the special cases of electrical mobility of charged particles in a fluid under the influence of the applied electric field. Electrical mobility is the ability of charged particles to move through a medium in response to an electric field. Charge mobility is given as

$$\mu = \frac{v_d}{E} \quad (4)$$

where;  $v_d$  is the drift velocity and  $E$  is the electric field.

The conductivity depends on the mobility and carrier concentration. Studies show that mobilities should be higher than  $10^{-4} \text{ cm}^2/\text{V}\cdot\text{s}$  to extract the carriers as they are transported in the device before they undergo recombination. The mobilities of  $10^{-4}$ – $10^{-2} \text{ cm}^2/\text{Vs}$  are probably optimal for devices with the film thicknesses of 200–500 nm<sup>[19]</sup>. Higher mobilities require changes in the design of the device to minimise dark current and ensure high photon-to-electron conversion efficiencies with low voltage dependence. The low voltage dependence of photon-to-electron conversion efficiencies contributes to high fill factors which leads to high photocurrents. The high

photocurrents require light absorption over the entire solar spectrum leading to the development of low bandgap polymers. The highest photocurrents that have been achieved under one-sun illumination for polymer PV is  $\sim 15\text{mA/cm}^2$  as compared to  $40\text{mA/cm}^2$  for a single crystal silicon cell, leaving room for progress<sup>[19]</sup>. Minimising the losses in the chemical potential of the device is necessary to drive  $V_{oc}$  to the maximum.

## 2.6 Doping

Doping is the process of adding impurities known as dopants in a semiconductor solar cell or polymer solar cell to alter its electrical, structural and optical properties. These impurity atoms are known as dopants. A primary dopant is a substance that drastically changes the electronic, optical, structural and magnetic properties and is accompanied by an increase in conductivity. A secondary dopant is an inert substance that if applied to a primary doped polymer further induces changes in the properties of a polymer, for example to increase its conductivity<sup>[44],[45]</sup>.

The doping process requires some necessary conditions to follow. The atom to be doped in the compound must be placed at the same position as that of atom of the dopant. There should be no distortion in the material after the insertion of the dopants. The size of the dopants should be precisely the same as that of the size of the atom of the compound. The percentage of doping in a compound should not be more than one percent<sup>[46]</sup>.

### 2.6.1 Doping in conductive polymers

Doping in conductive polymers is done by adding chemical surfactants to either oxidise or reduce the system so that the electrons are pushed into the conducting orbitals within the potentially conducting polymer.

There are two methods of doping a conductive polymer, that is chemical and electrochemical doping. Both methods use the principle of an oxidation-reduction (REDOX) process. Chemical doping involves exposing a polymer to an oxidant or a reductant. The method of exposing a polymer to a reductant is far less common and involves the alkali metals. Electrochemical doping is done by suspending a polymer-coated, working electrode in an electrolyte solution in which the polymer is insoluble along with reference electrodes and a separate counter electrode. The electric potential difference is created between the two electrodes that cause charge and appropriate counterions from the electrolyte to enter the polymer in the form of electron addition or removal. The process of doping that involves the movement of charge and counterions from an electrolyte to diffuse the polymer in the form of electron addition is called *n*-doping, while the process involving the removal of electrons is called *p*-doping. The former is less common because the abundant oxygen in the Earth's atmosphere creates an oxidising environment. An *n*-doped polymer reacts immediately in the presence of oxygen to de-dope (reoxidize to the neutral state) the polymer. Thus, chemical *n*-doping is performed in an inert environment. Electrochemical *p*-doping is very common in research because it is easier to exclude oxygen from a solvent in a sealed flask.

### **2.6.2 Doping in organic molecular semiconductors**

Molecular dopants are more preferred in doping molecular semiconductors because of their compatibilities of processing with the host due to similar evaporation temperatures or controllable solubility. Molecular dopants are more beneficial because of their relatively large size as compared to metal ion dopants like  $\text{Li}^+$  and  $\text{Mo}^{6+}$ , which makes them have excellent spatial confinement to be used in a multilayer structure in OLEDs and Organic solar cells<sup>[44]</sup>.

### **2.7 Morphology**

Morphology is the structural arrangement of atoms and /or molecules in different materials such as conducting polymers. The properties of the conducting polymers lie in the alignment of the polymers themselves. The arrangement of the polymers affects the mobility of the charges within the polymer itself. The choice of polymer blends and doping levels affects the morphology. The spin coating speed also plays a part in the outcome of the morphology. The distribution of the polymers in the hole transporting layer affects the mobility and electrical properties of the conducting polymers.

Morphology studies conducted on the active layer of the polymer solar cell help to understand how the donor and acceptor materials may be distributed within the active layer of an organic solar cell<sup>[29]</sup>. The distribution of electron acceptor and donor in the active layer is known to influence the electrical properties of polymer solar cells. The blending of the solution and spin-coating plays an essential role in the quest for morphology control<sup>[29]</sup>.

The active layer of a polymer solar cell consists of a blend of an electron donating conjugated polymer and an electron-accepting fullerene derivative. The impact of the morphology of the active layer on the solar cell performance is demonstrated in many systems. The systems in the polymer blends that display laterally phase separated domains have been studied extensively by a variety of microscopy techniques. The most common way of varying and controlling the morphology of a donor/acceptor system is through the choice of processing solvents and the use of solvent additives during formation. This change in morphology is often accompanied by improved performance. The effect of additives on film morphology and device performance depends strongly on the material system in use<sup>[47]</sup>.

## **2.8 Hole transporting layers**

The morphology of the active layer in polymer solar cells is often such that the donor and acceptor materials are in direct contact with both electrodes. Hence, the interfacial layers are commonly placed between the active layer and the electrodes to improve charge selectivity and enhance charge extraction<sup>[48]</sup>. The layer positioned between the active layer and the anode is known as the hole transporting layer (HTL) whereas that placed between the active layer and the cathode is known as the electron transporting layer. For it to function as an efficient HTL, the workfunction should be high enough to match the HOMO of the donor. For a reason, an upper contact barrier at the anode/donor interface can be avoided, and ohmic contact between the anode and the active layer promoted. If the conduction band of the HTL material lies sufficiently far above the LUMO of the active layer materials, the HTL will also prevent electron transfer into the anode. The material for the hole transporting layer should have high

mobility to facilitate the transportation of charge to avoid back transfer and recombination of charges<sup>[19]</sup>. Figure 12 shows the components of an organic solar cell with an HTL material that has an electronic structure such that hole collection by the anode may be facilitated while electron transport to the anode blocked.

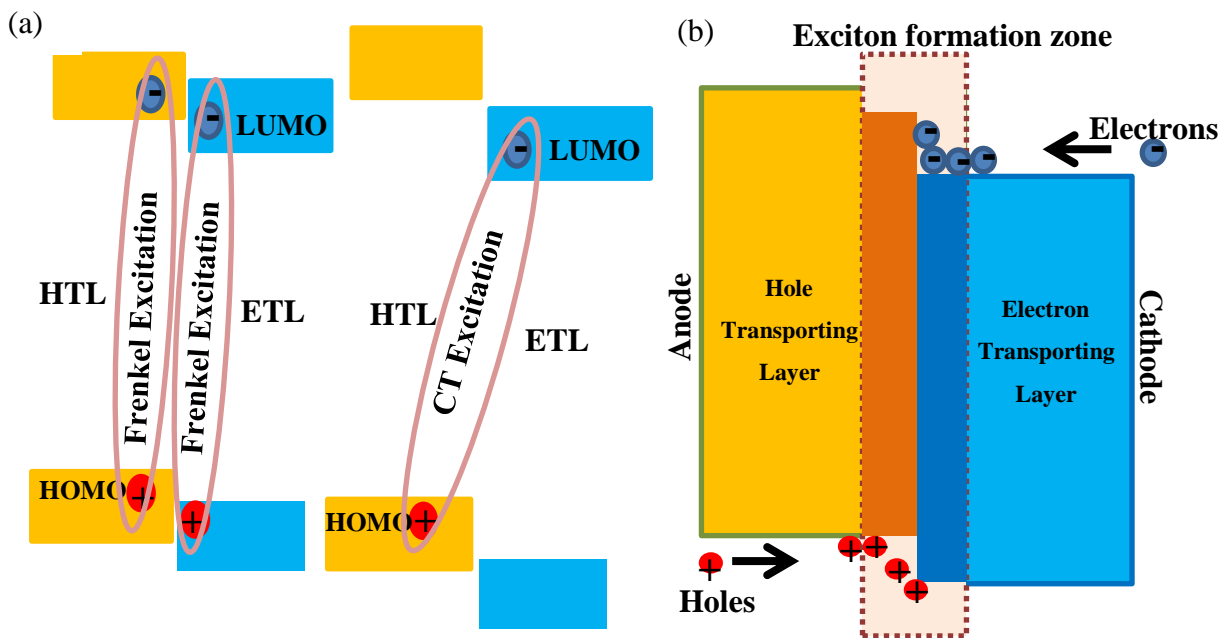


**Figure 12:** Organic solar cell with an HTL material

The optical properties of the HTL are essential since only the light that reaches the active layer and is absorbed produces excitons and thus contribute to the photocurrent. The HTL should have a high transmittance in the spectral region where the solar cell operates. Materials with high band gaps are therefore suitable since they have high optical transmittance in most of the solar spectrum. In solar cells with the conventional device structure where the active layer is deposited on top of the HTL, the HTL material

should also have a surface energy that allows for good wetting and film formation of the active layer. Materials used as HTLs should also have high hole mobility. Different types of materials have successfully been used as HTLs in polymer solar cells. One of the most commonly used is PEDOT: PSS, a water-soluble polyelectrolyte that can have high electrical conductivity and exhibits high optical transparency in the visible region<sup>[49]</sup>. The relatively high work function of PEDOT: PSS can lead to a low energy barrier for holes at the interface between the active layer and the PEDOT: PSS.<sup>[50],[51]</sup> However, the major drawback of PEDOT: PSS lies in its adverse chemical properties such as its hygroscopic and acidic nature, which are harmful to the long term stability of BHJ organic solar cells.<sup>[51],[52]</sup> The recent state-of-the-art donor materials are designed to have a deep-lying HOMO to maximise the  $V_{oc}$ , hence having HTLs with high work functions has become increasingly important<sup>[53]</sup>.

## CHAPTER THREE

### LITERATURE REVIEW

#### 3.0 Introduction

Early attempts to use molecular electronic materials in photovoltaics employed an organic semiconductor as a direct replacement for the inorganic semiconductor in a conventional solar cell and this led to poor performance. This first promising approach was a heterojunction that contained two different organic semiconductor layers, one of which had a stronger affinity for electrons and the other for holes<sup>[54]</sup>. A heterojunction is necessary to separate the light generated excitons. Further work on solution-processable conjugated polymers showed that a distributed or "bulk" heterojunction could be made by casting a layer from a mixture of two different polymers, or a polymer and a soluble fullerene molecule, in solution, and that such a heterojunction was effective at generating a photocurrent.

The effective bulk heterojunction devices were made from blends of polymers with other small molecules, an inorganic semiconductor nanoparticle, or metal oxide acceptors, and small molecule combinations, but most research had focused on polymer: fullerene combinations. Key advances continued through the last decade, with the discovery of performance improvements resulting from the choice of solvent, use of a self-ordering polymer, processing treatments such as thermal annealing, better matching of electrodes to organic layers, lower band gap polymers, alternative acceptors, and higher ionization potential polymers, resulting in present-day efficiency records of 8.3 % (certified)<sup>[27]</sup> and over 9 % (uncertified)<sup>[27]</sup>. A wide range of material

systems has been explored for OPV including solution processed polymer acceptor systems, where the acceptor component may be a polymer, fullerene, soluble small molecule, inorganic semiconductor nanoparticle, or metal oxide. In the past years, more companies have become engaged in the development of OPV technology and materials<sup>[4]</sup>, while academic research has burgeoned, with increasing attention paid to both fundamental and industrial issues<sup>[34]</sup>.

PEDOT: PSS is one of the most successful commercial conductive polymers due to its high mechanical flexibility and excellent thermal stability<sup>[55],[56]</sup>. PEDOT: PSS is well-known as the most remarkable conducting polymer, due to its good film-forming properties, high transparency, tunable conductivity, and excellent thermal stability<sup>[34]</sup>. However, the electrical conductivity of pristine PEDOT: PSS is less than 1 S/cm, which is too low to be utilised in polymer cells. High conductivity is the major factor affecting the efficiency of the polymer cells and different approaches have shown to improve the conductivity of PEDOT: PSS.

The conductivity of PEDOT: PSS has been reported to be increased by the addition of dielectric organic solvents, such as dimethyl sulfoxide (DMSO) or by post-treatment with a strong acid<sup>[57]</sup>. To improve the performance of PEDOT: PSS for high efficient polymer solar cells, it is necessary to increase the conductivity of PEDOT: PSS.

Research has shown that the conductivity of PEDOT: PSS film can be increased to 80 S/cm by adding SDS into PEDOT: PSS aqueous solution through blending method. The conductivity of PEDOT:PSS increased from 0.5 to 1008 S/cm with increasing concentrations of SDS solution from 0 to 400 mM by dipping method<sup>[58]</sup>. Additionally,

the film thickness decreased from 80 to 30 nm with increasing concentrations of SDS aqueous solution<sup>[59]</sup>.

A significant improvement of the conductivity of PEDOT:PSS films (from ~1 S/cm to more than 1000 S/cm) was achieved by glycerol monostearate (GMS) modification and the highest conductivity reached 1019 S/cm<sup>[60]</sup>. The conductivity improvement by GMS modification is proposed to result from the GMS-induced segregation of PSS chains and the conformational change of the conductive PEDOT chains within PEDOT:PSS. The hydrophobic groups of GMS interact with the hydrophobic PEDOT of PEDOT:PSS and the hydrophilic groups interact with the hydrophilic PSS chains. The hydroxyl groups play an important role in the phase separation between PEDOT and PSS chains<sup>[60]</sup>. The conductivity of PEDOT:PSS increased due to the expansion of the PEDOT chains. The conductivity enhancement was due to the increase of the charge-carrier mobility resulting from the conformational change of the PEDOT chains from coiled to linear which led to the increase in inter-chain interaction among the PEDOT chains<sup>[61]</sup>. PEDOT:PSS was also treated with formic acid and recorded a conductivity of 2050 S/cm achieved at 26M with high transparency<sup>[62]</sup>.

The highest conductivity of PEDOT:PSS films obtained up to now reached 4380 S/cm<sup>[58]</sup> very recently by using sulphuric acid treatment method, achieving four orders of magnitude as compared to untreated PEDOT:PSS films<sup>[61]</sup>. The conductivity of the thin films of PEDOT:PSS were first enhanced from 0.3 S/cm to 3065 S/cm through a treatment with dilute sulphuric acids. PEDOT:PSS films with a sheet resistance of 39  $\Omega$ /sq and transparency of around 80% at 550 nm were obtained. These PEDOT:PSS

films with conductivity and transparency comparable to ITO can replace ITO as the transparent electrode of optoelectronic devices<sup>[63]</sup>.

Ishida and co-worker reported that the carrier mobility extracted from thin film transistors of highly conductive PH1000 films with EG addition was  $1.7 \text{ cm}^2/\text{Vs}$  and the carrier density was in the order of  $10^{21}/\text{cm}^3$ <sup>[64],[9]</sup>. For the film without EG addition, the carrier mobility showed a much lower value of  $0.045 \text{ cm}^2/\text{Vs}$  and the carrier density was on the order of  $10^{20}/\text{cm}^3$ . These results provided direct evidence that the improvement in electric conductivity in PEDOT:PSS following the addition of EG was mainly caused by improving the carrier mobility, and that it also increased the calculated carrier density.' It was then concluded that the improved carrier mobility and carrier density was as a result of the morphological change in the PEDOT:PSS films caused by the addition of ethylene glycol (EG)<sup>[56]</sup>.

Researches have demonstrated the ability to improve the conductivity of PEDOT: PSS to that of ITO, but the reasons behind the high conductivity have not much been explored in terms of optical, morphological, structural and electrical properties.

A summary of conductivity improvements on PEDOT: PSS are given in the Table 1.

**Table 1:** Conductivity improvement on PEDOT:PSS

<b>DOPANT</b>	<b>CONDUCTIVITY (S/cm)</b>	<b>REFERENCE</b>	<b>APPLICATION</b>
PEDOT:PSS:DMSO	800.0	<b>73</b>	Conducting polymer
PEDOT:PSS:GMS	1019	<b>57</b>	Conducting Electrode
PEDOT:PSS+FormicAcid	2050	<b>59</b>	Conducting Electrode
PEDOT:PSS:SDS	1008	<b>55</b>	Conducting Electrode
PEDOT:PSS: H <sub>2</sub> SO <sub>4</sub>	3065	<b>8</b>	Conducting Electrode
PEDOT:PSS: H <sub>2</sub> SO <sub>4</sub>	4380	<b>58</b>	Conducting Electrode
PEDOT:PSS + CH <sub>3</sub> OH	1362	<b>79</b>	Conducting Electrode

# CHAPTER FOUR

## EXPERIMENTAL METHODS

### 4.0 Introduction

This chapter describes the materials and the basic working principles of the instruments that were used to characterise the optimized samples. The main material of study in this dissertation is poly (3, 4-ethylene dioxythiophene) polystyrene sulfonate (PEDOT:PSS). This chapter describes the methods used for the preparation of the samples and characterization. The methods give step by step details how the preparation of the samples was done. In this chapter the steps carried out to characterise the samples are also clearly outlined

### 4.1 Materials Preparation

The materials used to prepare the samples were poly (3, 4-ethylene dioxythiophene) polystyrene sulfonate (PEDOT: PSS), sodium dodecyl sulfate (SDS) and copper nanoparticles. The PEDOT: PSS was first doped with SDS as a secondary dopant and then copper nanoparticles (CuNPs) were used as a tertiary dopant. The type of PEDOT: PSS used was the high-grade PH 1000 thin films purchased from Osila. The SDS solution was prepared from sodium dodecyl sulphate powder from Aldrich. The copper nanoparticles were prepared from copper sulphate pentahydrate using sodium hydroxide solution, sodium borohydrate solution, sodium dodecyl sulphate and Ascorbic acid purchased from Aldrich

## **4.2 Sample Preparation**

### **4.2.1 PEDOT: PSS containing sodium dodecyl sulfate**

First, the PEDOT: PSS (PH 1000) thin films were prepared using four different concentrations of SDS. The concentration was varied in the PEDOT: PSS (PH1000): SDS solution and the samples were compared with a pristine sample. The PEDOT: PSS was filtered through a 0.45 $\mu$ m PES syringe filter. The SDS solution was prepared by dissolving appropriate amounts of SDS powder in distilled water. Different solutions of varied concentrations of the samples were prepared as follows: 5% SDS, 10% SDS, 15% SDS and 20% SDS concentrations in PEDOT: PSS (PH1000) solution.

### **4.2.2 PEDOT:PSS containing Sodium dodecyl sulfate and copper nanoparticles**

#### **4.2.2.1 Synthesis of copper nanoparticles**

The solutions for making copper nanoparticles were prepared by dissolving appropriate amounts to make the following concentrations of 0.1 M sodium hydroxide solution (NaOH), 0.01M sodium borohydrate solution (NaBH<sub>4</sub>), 1.0 M sodium dodecyl sulphate (SDS), 0.03 M copper sulphate pentahydrate (CuSO<sub>4</sub>.5H<sub>2</sub>O) and 0.01M Ascorbic acid. To synthesize the copper nanoparticles, 4ml of CuSO<sub>4</sub>.5H<sub>2</sub>O was pipetted into a 30 ml container. In the container, 5 ml of distilled water was added to get a pale blue solution. Then 2ml of SDS and 4 drops of NaOH were added to the contents and the solution changed its colour to yellow. Later, 1ml of NaBH<sub>4</sub> was added and the solution changed to orange and then brick red. The solutions were left overnight for the copper nanoparticles to settle. The copper nanoparticles were then collected by decanting the solution and rinsed with acetone and left for 30minutes for the particles to settle again.

The rinsing was done twice to make sure that all the SDS was completely washed away. The copper nanoparticles were then dried using nitrogen to create an inert environment so that the copper nanoparticles do not oxidise. Appropriate amounts of copper nanoparticles were then measured and added to make PEDOT: PSS: SDS: CuNPs solution ranging from 0% to 5 % copper nanoparticles.

#### **4.2.3 Film Deposition**

The glass substrates were prepared by first cutting an area of 2.0 cm x 2.0 cm. These were washed in acetone and soapy water to remove dirt from the surface. They were then cleaned by subsequent ultra-sonication in detergent water and twice with deionized water. The substrates were then dried in the open air at room temperature. Then 2 ml of PEDOT: PSS: SDS: CuNPs was measured using a syringe and spread over the glass substrate. Spin coating was done at 3000 rpm (revolutions per second) for 1 minute using the Laurell 650 M spin Coater. The samples were left to dry in open air for a 5 - 10 minutes, at room temperature and then annealed. The annealing of the samples was performed at temperatures of 130°C, 150°C and 170°C. Films with PEDOT: PSS: SDS: CuNPs were annealed in a hot atmosphere at 130°C for 20 minutes, at 150°C for 5 minutes and 170°C for 5 minutes. The annealed samples were subsequently characterised for electrical, optical, morphological and structural properties.

#### **4.3 Experimental Techniques**

The instruments used in this dissertation for characterization are; Atomic Force Microscope (AFM), Scanning Electron Microscopy (SEM), X-ray Diffractometer (XRD), Raman spectrophotometer, Ultra violet-visible spectroscope (UV-vis), Hall Effect Measurement system and Four point probe. The morphological evaluation was

done using the Atomic Force Microscopy, FlexiAFM nanosurf and Zeiss Ultra plus 55 field emission scanning electron microscope (FE-SEM). Structural characterization was conducted using an XPERT-PRO X-ray Diffraction and a WITec alpha 300 RAS+ Confocal micro-Raman microscope. The ultraviolet-visible spectroscopy, UV 2600 Shimadzu was used to perform analysis to evaluate the optical properties and hence study the absorption characteristics. The Hall Effect measurement was done using HMS-3000 Ecopia Hall Effect measurement system connected to a data acquisition computer. The RM3000 Jandel Four Point Probe coupled to a source meter that was used for electrical characterization.

#### **4.3.1 Atomic force microscopy (AFM)**

The atomic force microscope is a high resolution imaging device with a high resolution scanning probe microscope that can measure in a fraction of nanometres. An AFM uses a cantilever with a sharp tip to scan over the sample. The scanning is done by the tip of the probe which moves over the surface. As the tip of the probe approaches the surface at a close range, the attractive force between the surface and the tip causes the cantilever to deflect toward the surface of the specimen. The flexible cantilever that has its tip mounted scans over the surface while keeping the force constant between the tip and the specimen surface. A laser beam is used to detect the cantilever deflections towards the specimen surface or away. The cantilever causes slight changes in the reflected beam that is recorded by a sensitive photodiode which is used to generate an accurate topographic map of the surface.

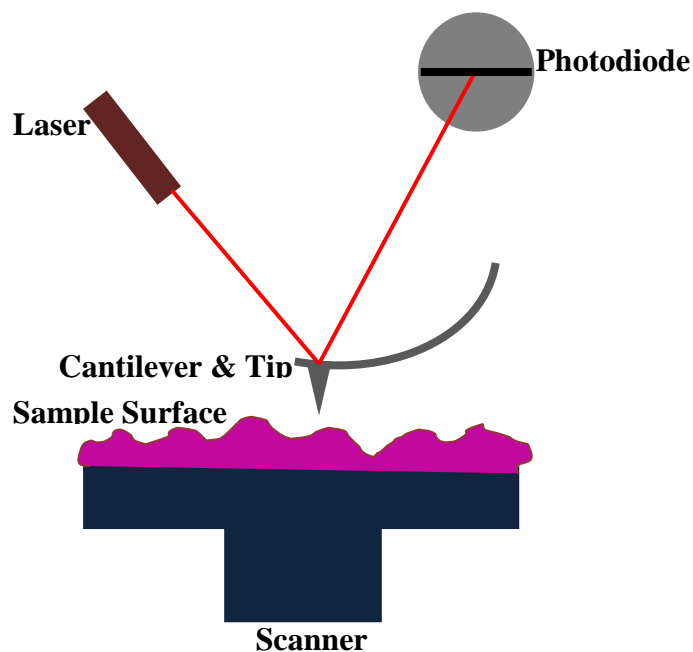


**Figure 13:** Schematic Structure of Atomic Force Microscopy

Imaging can be done by either contact mode (static) or tapping mode (dynamic). In contact mode, the tip is in continuous contact with the sample and the detected net force is the sum of the attractive and repulsive force between the tip and the sample. In tapping mode, the topography of the sample is mapped by tapping the surface of the sample with an oscillating probe tip. The amplitude of the cantilever's oscillation changes with surface topography of the sample and the topography image is obtained by monitoring these changes.

#### **4.3.1.1 Characterisation using Atomic Force Microscopy**

The Atomic Force Microscopy was carried out to study the surface morphology of the samples by using a FlexiAFM nanosurf easyscan2 operating in non-contact mode. The 2.0 cm x 2.0 cm glass substrate spin-coated with doped PEDOT: PSS films was mounted on the stage inside the Nanosurf microscope which is interfaced with the

computer. Scanning was performed on 10  $\mu\text{m}$ , 500 nm, and 250 nm scan areas to obtain the topography that was used to evaluate the surface morphology of the samples. The atomic force microscopy was also used to determine the film thickness of the samples by creating a step on each sample and then scanning over that area. The difference in the sharp peaks of the topography obtained by scanning over the step was used to determine film thicknesses. For each concentration of 0% SDS, 5% SDS, 10% SDS, 15% SDS and 20% SDS, three samples were scanned to obtain the topography that was analysed for surface morphologies and film thicknesses.

#### **4.3.2 Scanning Electron Microscope**

A scanning electron microscope (SEM) is a microscope that is used to produce images by scanning the surface with a focused beam of electrons. The electrons interact with atoms in the sample, generating signals that contain information about the surface topography. The electrons from the beam hit the surface of the object and bounce. The number of electrons that can be detected depends on the specimen topography. A detector collects the scattered electrons and turn them into an image. The electron beam is scanned in a fast mode and the position of the beam is combined with the signal detected to produce an image.

##### **4.3.2.1 Characterization using Scanning Electron Microscopy**

Scanning electron microscopy (SEM) micrographs of the prepared samples were obtained using a Zeiss Ultra Plus 55 field emission scanning electron microscope (FE-SEM) operated at 1.0 nm, 15 kV. The samples spincoated on 2.0 cm  $\times$  2.0 cm glass

substrate were mounted on a stage and placed in the specimen chamber which was evacuated. The scan was run to give a detailed image of the micrographs.

### **4.3.3 X-Ray Diffraction (XRD)**

X-ray diffraction is an analytical technique used in materials science to determine crystal structures. XRD is used to trace the paths of X-rays through crystals to probe the structure. The two primary techniques involved are powder X-ray diffraction and single X-ray diffraction. The powder X-ray diffraction defines phases and purity of the crystalline species. The single X-ray diffraction gives identity to the atoms in a crystal and their locations, the electron densities, bond lengths, and angles<sup>[65]</sup>. X-rays are electromagnetic waves whose wavelength is similar to the atomic spacing in crystals. When a single X-ray strikes an individual atom, it is diffracted. When two coherent X-rays strike atoms in different planes, the diffracted X-rays interfere, resulting in constructive or destructive signals. The diffraction pattern of a powder crystalline sample comprises of intense spots that form rings of constructive interference. The angles at which these spots occur correspond to the spacing of atoms in that plane. The spacing can be determined using Bragg's Law.

Bragg's law is a law in physics that defines the relationship between the angle of X-rays or electrons and the distance between the crystal planes so that there is a strong reflection of the X-rays.

$$2d\sin\theta = n\lambda \quad (5)$$

Where  $\theta$  is the angle between the incident or the reflected beam and the crystal plane,  $\lambda$  is the X-ray wavelength,  $d$  is the crystal plane separation, and  $n$  is an integer

An X-ray diffractometer consists of three primary components namely the X-ray source, a specimen holder, and a detector. All components are oriented in a coplanar, circular arrangement with the sample holder at the centre. The source usually contains a Copper target that emits a beam of collimated X-rays when bombarded by electrons. The beam is directed at the sample, which refracts the X-rays. The sample and the detector are then rotated in opposite directions until the angles of X-ray intensity are determined. High X-ray intensity corresponds to constructive interference by a crystallographic plane in both single-crystal and powder X-ray diffraction. Powder X-ray diffraction reveals the crystal structure of the sample, while single-crystal X-ray diffraction additionally reveals the chemical content and locations of atoms<sup>[66]</sup>.

#### **4.3.3.1 Characterisation using X-Ray Diffraction**

The structural analysis (X-ray diffraction (XRD)) was carried out using an XPERT-PRO with the reflection geometry at  $2\theta$  values ( $1^\circ - 50^\circ$ ) with a step size of  $0.05^\circ$ , operating with a Cu  $K\alpha$  radiation source  $\lambda = 1.54184$  nm at 30V and 10A . Powder X-ray diffraction and single-crystal X-ray diffraction were run to reveal the crystal structure and chemical content and locations of the atoms respectively. The sample scanning was run at  $2\theta$  with a step size of  $0.05^\circ$  to obtain the spectrum that was analysed to give the size of the crystal and give chemical composition in the samples. XRD was also used to observe the angular positions of the lattice indices at different peaks which were used to determine the crystal structure of the samples.

### 4.3.4 Raman Spectroscopy

Raman spectroscopy is a spectroscopic technique that is used to observe vibrational, rotational and other low-frequency modes in a system<sup>[67]</sup>. Raman spectroscopy is mostly used in chemistry to provide a structural fingerprint to identify molecules.

The spectroscopy depends on the inelastic scattering or Raman scattering of monochromatic light from a laser in the visible, near-infrared, and near-ultraviolet range. The laser light interacts with molecular vibrations, phonons or other excitations in the system, resulting in the energy of the laser photons being shifted up or down. The shift in energy gives information about the vibrational modes in the system.

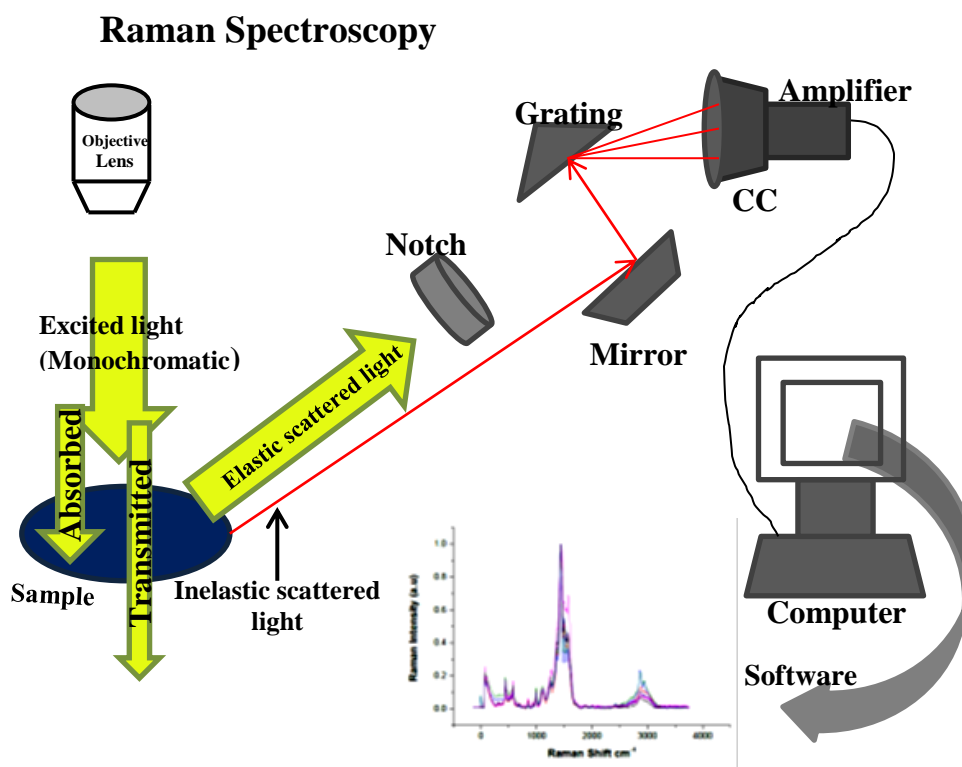
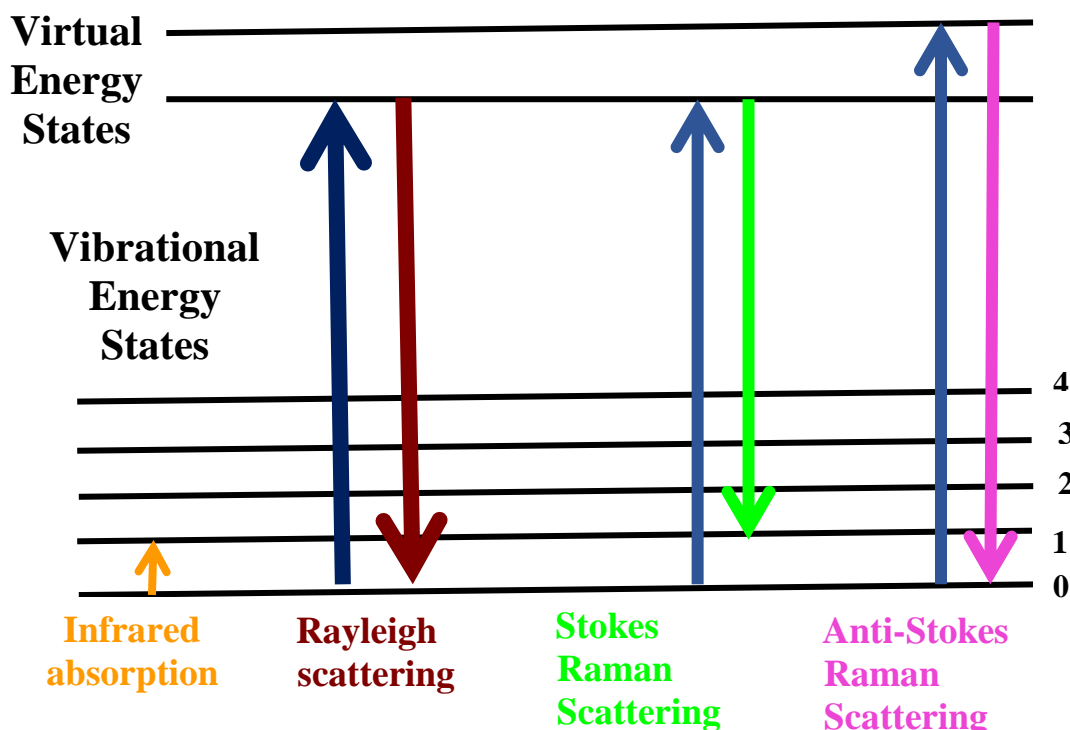


Figure 14: Schematic diagram For Raman Spectroscopy

The sample is illuminated with a laser beam. The electromagnetic radiation from the illuminated spot is collected with a lens and sent through a monochromator. The scattered radiation at the wavelength corresponding to the laser line (Rayleigh scattering) is filtered out by either a notch filter, edge pass filter, or a bandpass filter. The rest of the collected light is dispersed onto a detector. Spontaneous Raman scattering is typically very weak, and as a result, the main difficulty of Raman spectroscopy is separating the weak inelastically scattered light from the intense Rayleigh scattered laser light<sup>[68]</sup>.



**Figure 15:** Energy-level diagram showing the states involved in Raman spectrum

Raman spectroscopy is used to study the chemical bonding, intra-molecular bonds and to identify molecules as well as to find out the phase shift in the bonds.

#### 4.3.4.1 Characterisation using Raman spectroscopy

A WITec alpha 300 RAS+ Confocal micro- Raman microscope (Focus Innovations, Germany) set on a 532 nm laser wavelength was used to characterize the PEDOT: PSS: SDS: CuNPs samples with a spectral acquisition time of 150 s and laser power of 5 mW to avoid sample heating. The samples were scanned to obtain the spectrum which were analysed to determine the phase shift as well as the vibrational stretching of the atoms.

#### 4.3.5 Ultraviolet-Visible Spectroscopy

##### 4.3.5.1 Basic Principle

Ultraviolet-visible spectroscopy (UV/Vis) or ultraviolet-visible spectrophotometry (UV/Vis) is used to measure absorption or reflectance or transmittance in the ultraviolet, visible spectral region. The absorption of radiation by organic compounds mainly results from the presence of  $\pi$  bonds. Absorption of radiation by organic compounds occurs in the visible and ultraviolet region and involves the transitions of electrons from the ground state to higher energy states. The electronic transitions involved in the UV and visible regions are:  $n \rightarrow \pi^*$ ,  $\pi \rightarrow \pi^*$ ,  $n \rightarrow \sigma^*$ ,  $\pi \rightarrow \sigma^*$ ,  $\sigma \rightarrow \pi^*$  and  $\sigma \rightarrow \sigma^*$ . The only transitions that occur in the UV-vis region are observed as  $\pi \rightarrow \pi^*$  and  $n \rightarrow \pi^*$ . The transitions to antibonding orbitals are associated only with unsaturated centres in the molecule. These energies are sufficient to excite an electron to higher energy orbitals. When samples with matching energies are exposed to light, electronic transitions occur within the molecule and light energy is absorbed as the electron is promoted to the higher energy orbitals<sup>[32]</sup>. An optical spectrometer records

the wavelength at which absorption occurs together with the degree of absorption at each wavelength.

#### **4.3.5.2 Working principle of the Ultraviolet-Visible spectroscopy**

UV visible spectrophotometers consist of a UV-visible microscope integrated with a UV-visible spectrophotometer. The primary parts of a spectrophotometer are a light source (usually a tungsten filament), a sample holder, a diffraction grating in a monochromator or a prism to separate the different wavelengths of light, and a detector. The detector is a photomultiplier tube, a photodiode, a photodiode array or a charge-coupled device (CCD).

The UV uses light in the visible and adjacent ranges to run the scan. The single photodiode detectors and photomultiplier tubes used with scanning monochromators, filter light so that only the light that reaches the detector is that of a single wavelength. Scanning monochromators move the diffraction grating to each wavelength so that its intensity is measured as a function of wavelength. The absorption or the reflectance in the visible range directly affects the perceived colour of the chemicals involved in the region of the electromagnetic spectrum. Hence, the atoms and molecules undergo electronic transitions from the ground state to the excited state.

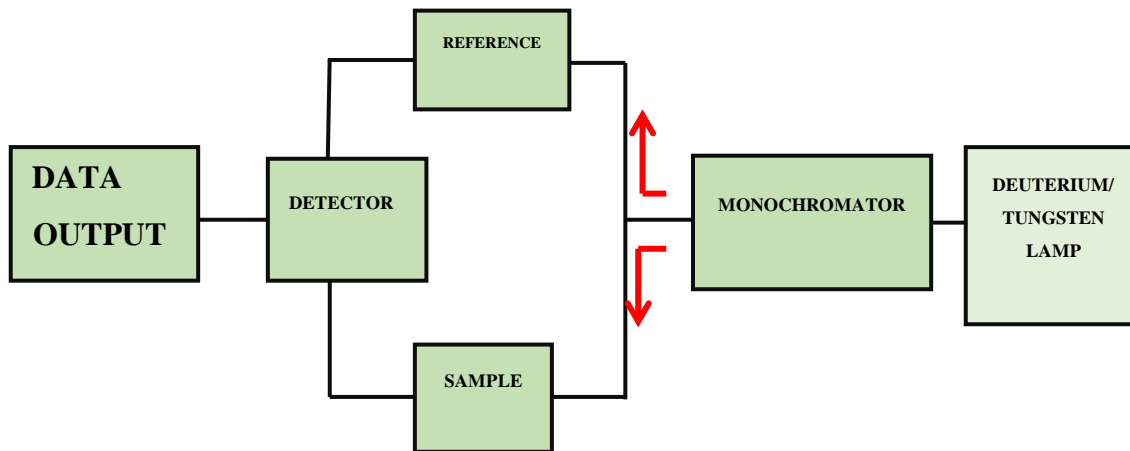


**Figure 16:** Simplified schematic of a double beam UV- Visible Spectrophotometer.

#### 4.3.5.3 Characterisation using Ultra Violet – Visible Spectroscopy

The UV-Vis spectroscopy was carried out to evaluate the optical properties and study the absorption characteristics of the samples using the UV 2600 Shimadzu set at wavelength 1000-200 nm with the fast scan speed in single mode operating at sampling interval 1.0. The maximum input wavelength was set at 1000 nm. Three samples were prepared for each of the four different concentrations. The absorption spectra obtained were used to evaluate the absorption characteristics of the samples.

#### 4.3.6 The Hall Effect Measurement

The Hall Effect is used to determine the carrier concentration, carrier type, and when coupled with a resistivity measurement and it is also used to measure the mobility of materials<sup>[69]</sup>. Figure 17 is a picture of the Hall Effect Measurement system.

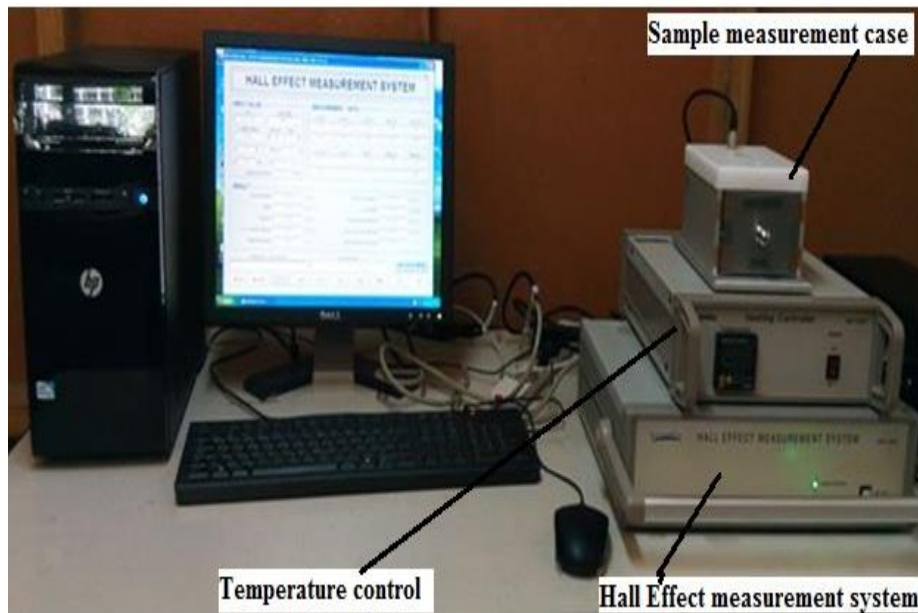


**Figure 17:** The Hall Effect Measurement System at University of Dar-es-salaam

#### 4.3.6.1 Working principle of Hall Effect

When the magnetic field  $B$  is applied on a conductor with current flowing in one direction, both positive and negative charge carriers are deflected in the magnetic field. If the charge carriers are electrons moving in the negative  $x$ -direction with a drift velocity  $v_d$ , they experience an upward magnetic force  $F_B = qv_d \times B$ , are deflected upward, and accumulate at the upper edge of the flat conductor, leaving an excess of positive charge at the lower edge. The accumulation of charge at the edges creates an electric field in the conductor and increases until the electric force on carriers balances the magnetic force acting on the carriers. When the equilibrium condition is reached, the electrons are no longer deflected upward and the potential difference generated across the conductor known as the Hall voltage  $\Delta V_H$  can then be measured<sup>[70]</sup>. The direction of charges depends on the carrier type. If the charge carriers are positive and moving in the

positive  $x$ -direction, the charges experience an upward magnetic force  $qv_d \times B$ , that induces accumulation of positive charge on the upper edge and leaving an excess of negative charge on the lower edge.

The Hall Effect operates by the underlying physical principle of the Lorentz force which is a combination of two separate forces, that is, the electric force and the magnetic force<sup>[71]</sup>. The Hall Effect describes the force exerted on a charged particle, such as an electron, moving through the magnetic field. If the magnetic field is oriented perpendicular to the direction of the motion of the electrons, the electrons experience a force that is perpendicular to both the direction of movement and the orientation of the magnetic field. Figure 18 shows the direction of the Lorentz force and velocity of an electron.

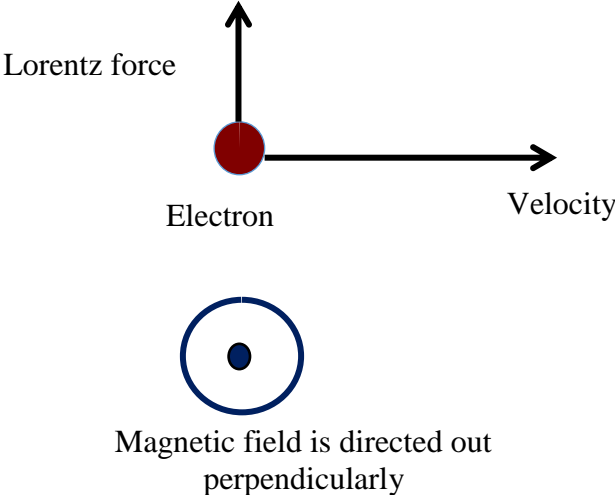


**Figure 18:** Schematic diagram showing the direction of the Lorentz force and velocity

The total resulting force experienced by the electron known as the Lorentz force  $F$  is the

$$\text{Lorentz force } (F) = -q(E + v \times B) \tag{6}$$

where  $q$  is the charge on the electron,  $E$  is the electric field,  $v$  is the particle velocity of the electron, and  $B$  is the magnetic field.

When in equilibrium, the magnetic force is balanced by the electric force, giving

$$qv_d B = qE \quad (7)$$

$$E = v_d B \quad (8)$$

If the sample is of width  $d$ , then the Hall voltage is given as

$$\Delta V_H = Ed = v_d B d \quad (9)$$

Measuring the current of the sample of cross sectional area  $A$  gives charge carrier density that can be used to find the drift velocity  $v_d$  as follows

$$v_d = \frac{I}{nqA} \quad (10)$$

Where  $A = dt$ ,  $d$  is the width and  $t$  is the thickness, then the Hall voltage becomes

$$\Delta V_H = \frac{IBd}{nqA} = \frac{IBd}{nqdt} = \frac{IB}{nqt} \quad (11)$$

The mobility can be determined from the equation

$$\mu = \frac{|V_H|}{R_s IB} = \frac{1}{qn_s R_s} \quad (12)$$

The bulk resistivity ( $\rho = R_s t$ ) and the bulk density ( $n = n_s / t$ ) can also be determined if the thickness of the conducting layer ( $t$ ) is known.

### 4.3.7 Hall Effect Measurements

The Hall Effect measurement was carried out to investigate the charge carrier mobility of PEDOT: PSS: SDS and PEDOT: PSS: SDS: CuNPs using HMS-3000 Ecopia Hall Effect measurement system connected to a data acquisition computer. The HMS-3000 Ecopia Hall Effect measurement system equipment contains a permanent magnetic source with a field strength of 0.57 Tesla, including the heating and cooling accessories, sample measurement case, and sample mounting board. The specimen sample was mounted on the stage by adjusting the probe contacts gently as shown in Figure 19. The hall effect measurement was performed by setting the parameters of the software to 1.0  $\mu A$ , with the interval and step range set to 0.10.

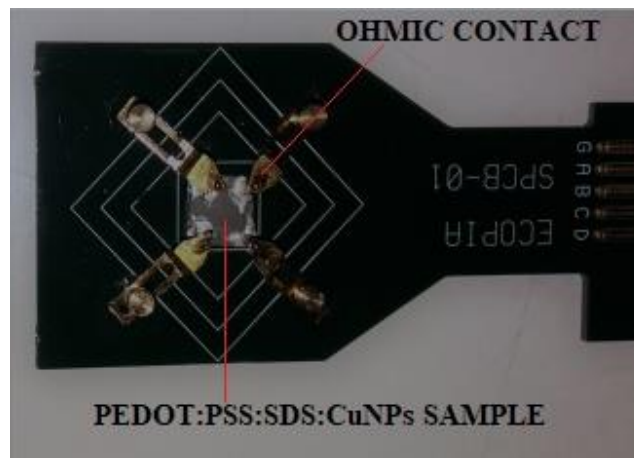


**Figure 19:** Picture of the Hall Effect sample mounting board with four ohmic contacts mounted on the sample specimen.

### 4.3.8 Electrical property measurements using a Four Point Probe

Four-point probe-based instruments work by the principle of a long-established technique that measures the average resistance of a thin sheet by passing a small current

through the outside two points of the probe and then measuring the voltage across the inside two points of the probe.

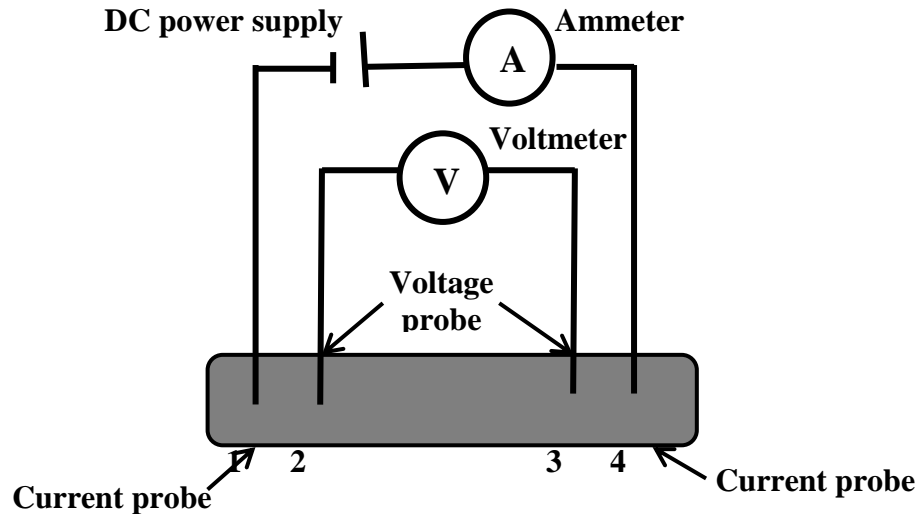


**Figure 20:** Schematic structure of a Four point probe

When the spacing between the probe points is constant, and the conducting film thickness is less than 40% of the spacing, and the edges of the film are more than four times the spacing distance from the measurement point, then the average resistance of the film or the sheet resistance is given by:

$$R_s = \frac{4.53 V}{I} \quad (13)$$

The resistivity (in ohm-cm) and the thickness of the film (in cm) are related to the sheet resistance ( $R_s$ ) by:

$$R_s = \frac{\text{resistivity}}{\text{thickness}} \quad (14)$$

Hence, the resistivity can be calculated if the thickness of a film is known, or the thickness of the film can be calculated if the resistivity is known.

The resistance of the samples can then be calculated as follows

$$R = \rho \frac{l}{wt} \quad (15)$$

Where  $\rho$  is the resistivity,  $A$  is the cross-sectional area, and  $l$  is the length. The cross-sectional area is split into the width ( $w$ ) and the sheet thickness ( $t$ ). If we combine the resistivity with the thickness, the resistance can be written as

$$R_s = \frac{\rho}{t} = 4.53 \frac{V}{I} \quad (16)$$

where  $R_s$  is the sheet resistance. With known film thickness, the bulk resistivity  $\rho_0$  can be calculated by multiplying  $R_s$  by the film thickness in cm:

$$\rho_0 = R_s \times t = \frac{4.532 \times V}{I} \times t \quad (17)$$

Equation (17) can be summarised as follows

$$\rho_0 = 4.532 \times t \times \frac{V}{I} \quad (18)$$

Then the conductivity of the sample or material is calculated using;

$$\text{conductivity} = \frac{1}{\text{Bulk Resistivity}} = \frac{1}{\rho_0} \quad (19)$$

The value of this conductivity is given in the Siemens per centimetre (S/cm).

#### **4.3.8.1 Characterisation using Four Point Probe Measurements**

The RM3000 Jandel Four Point Probe coupled to a source meter was used to study the electrical properties of the samples. The four-point probe interfaced to the computer was mounted on the sample gently. The recorded voltage and current values were used to generate the current-voltage curves which were then used to calculate the conductivity of the samples.

## CHAPTER FIVE

### RESULTS AND DISCUSSION

#### 5.0 Introduction

This chapter explains the results, observations and analysis made on the characterised samples of doped PEDOT: PSS with sodium dodecyl sulphate and copper nanoparticles. The chapter gives a detailed explanation of the observed morphological, optical, structural and electrical properties of the characterised samples.

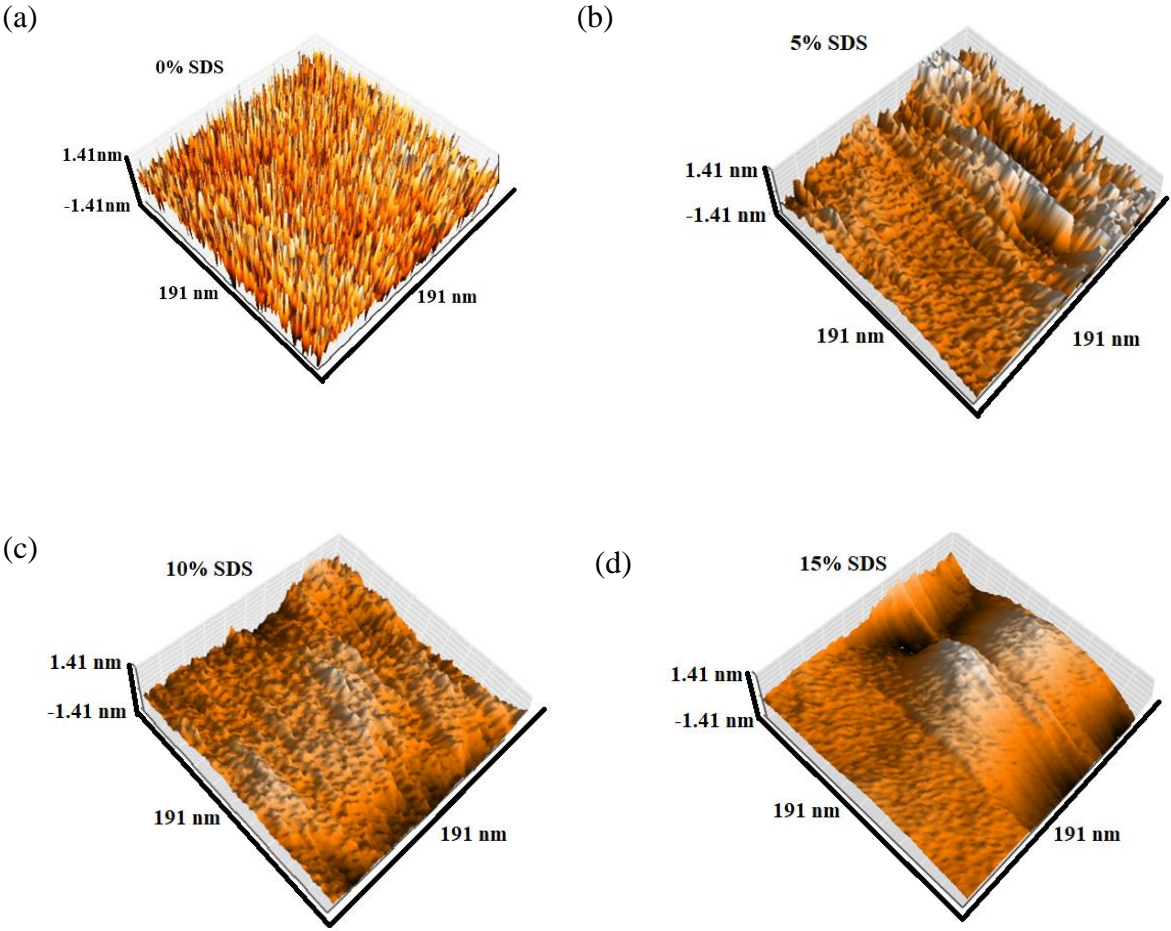
#### 5.1 Morphological Evaluation

The morphology was evaluated using Atomic Force Microscopy and Scanning Electron Microscopy.

##### 5.1.1 Morphological Evaluation by Atomic Force Microscopy

The topography obtained from the atomic force microscopy was evaluated to study the arrangement of the composites of polymers both in the pristine PEDOT: PSS and the doped PEDOT: PSS samples. The arrangement of the polymers is known to affect the mobility of the charges within the polymer itself. Polymers tend to align themselves when a surfactant is added. Polymers can form certain regular structures that demonstrate the improvement in the movement of charges. Some polymers form small packs of hexagonal structures, known as honey-combed structures when a suitable surfactant is added. Distinct changes in the surface morphologies of the PEDOT: PSS films were observed by atomic force microscopy as shown in Figure 22. Figure 22 (a) shows the composites of the polymers in undoped PEDOT: PSS. When the SDS is introduced in the pristine PEDOT: PSS, the composites of the polymers align

themselves in an orderly manner as observed from Figure 22 (b), which is doped with 5% SDS. As the concentration of the SDS doping increased from 10% SDS to 20% SDS, the composites of polymers formed orderly structures as shown in Figure 22 (c), (d), and (e), which are more visible at the nano scale. These results show that the introduction of SDS into PEDOT: PSS weakens the attraction between the hydrophobic PEDOT and hydrophilic PSS chains. Hence, induces phase separation between the PEDOT chains and the PSS chains featured by the segregation of the excess PSS domains surrounded by a continuous PEDOT phase leading to a more ordered polymer structure.



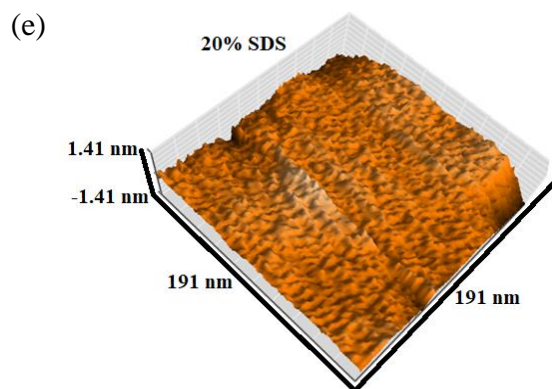


**Figure 21 3D:** AFM images of PEDOT: PSS (a) before doping, (b) after doping with 5% SDS, (c) after doping with 10% SDS, (d) after doping with 15% SDS, (e) after doping with 20% SDS.

In Figure 22, AFM results show phase images in which the positively charged (bright) and negatively charged (dark) phases corresponded to PEDOT-rich and PSS-rich grains, respectively<sup>[59]</sup>. The topography obtained from Atomic Force Microscopy showed phase separation between PEDOT chains and PSS chains as shown in Figure 22. In Figure 22 (a), the topography shows no phase separation in the pristine PEDOT: PSS. As soon as the SDS is introduced into PEDOT: PSS, distinct changes are observed as shown in Figure 22 (b), demonstrating the beginning of the phase separation in which the dark specs (PSS) separate from the bright spec (PEDOT). In Figure 22 (c), the PEDOT begin to assemble to form the continuous domains. In Figure 22 (d) and (e), the PEDOT forms continuous domains on top in which the insulating PSS is shielded at the bottom. The continuous PEDOT domains serve as better percolating pathways for charge carrier hopping among polymer chains, thus leading to higher conductivity. This is because the morphology change with phase separated PEDOT and PSS leads to larger grain sizes

and lower intergrain hopping. Thus, the conformal changes by reorientation of the PEDOT: PSS chains leads to better connection between the conducting PEDOT chains.<sup>[7]</sup>

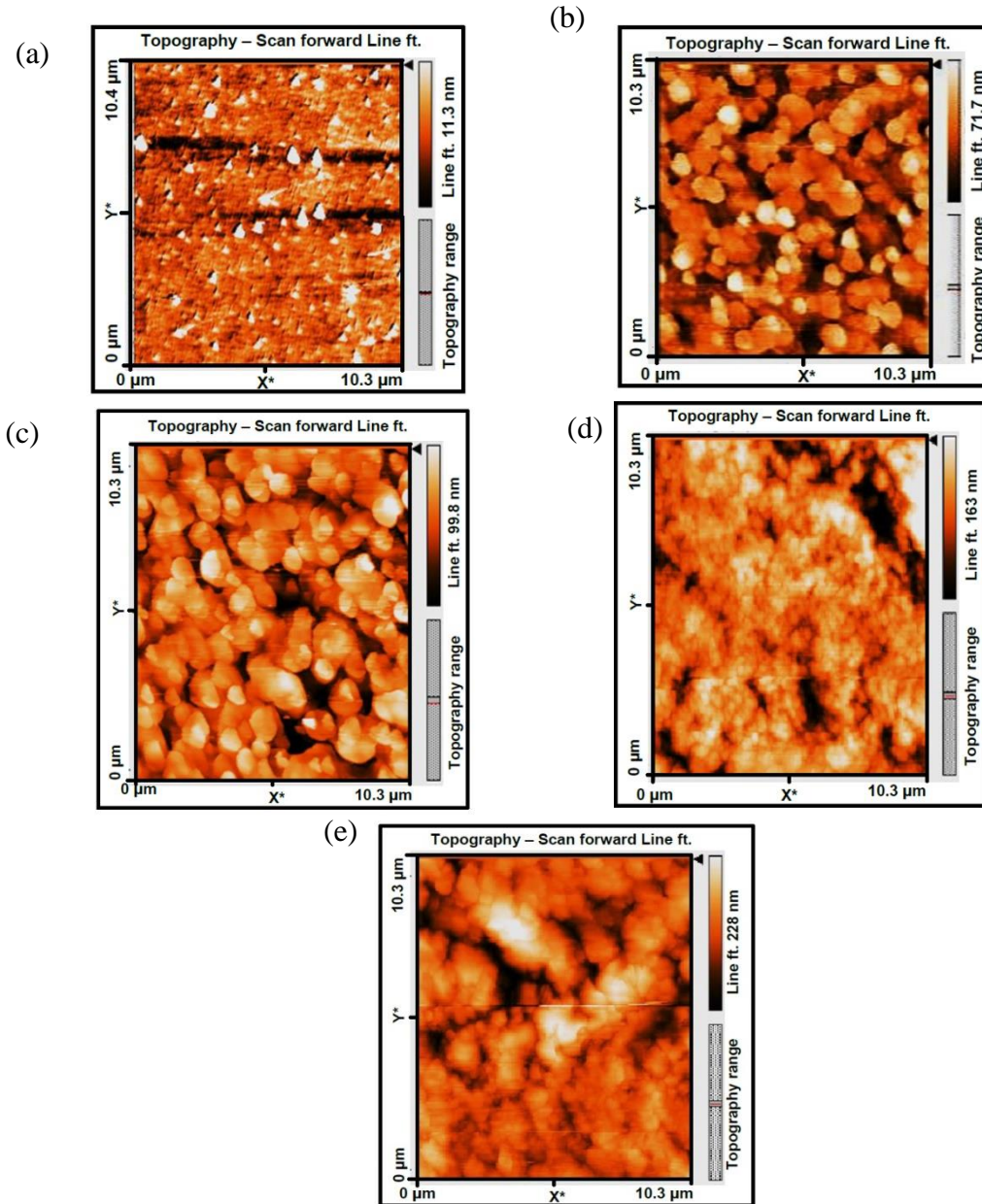


**Figure 22 2D:** AFM images showing phase separation(a) before doping, (b) after doping with 5%SDS, (c) after doping with 10% SDS, (d) after doping with 15% SDS, (e) after doping with 20% SDS.

In Figure 23, the morphology evolved into a honey-combed structure which was observed to be as a result of greatly exceeding the SDS critical micelle concentration (CMC)<sup>[72]</sup>. The CMS of SDS is 8 mM, and the concentration of the SDS that was used in doping was 690 mM. At higher concentrations, the spheres form small domains of loosely hexagonal packed spheres. The SDS increases the ionic strength of the solution, which is the driving force for the migration of the polystyrene spheres from the bulk solution to the air-liquid interface. The presence of the SDS in the PEDOT: PSS solution slows down the electrolyte evaporation at the air-liquid interface and decreases the surface tension allowing the polystyrene sulfonate to form a monolayer at the air-solution interface when the PEDOT electrode emerges from the solution. Furthermore, hydrophobic interactions between the surfactant and the glass substrate surface activate osmotic forces, which push the polystyrene sulfonate together with the substrate and interactions between the polystyrene and SDS promote the formation of a hexagonal monolayer arrangement due to its thermodynamic stability.<sup>[72]</sup>

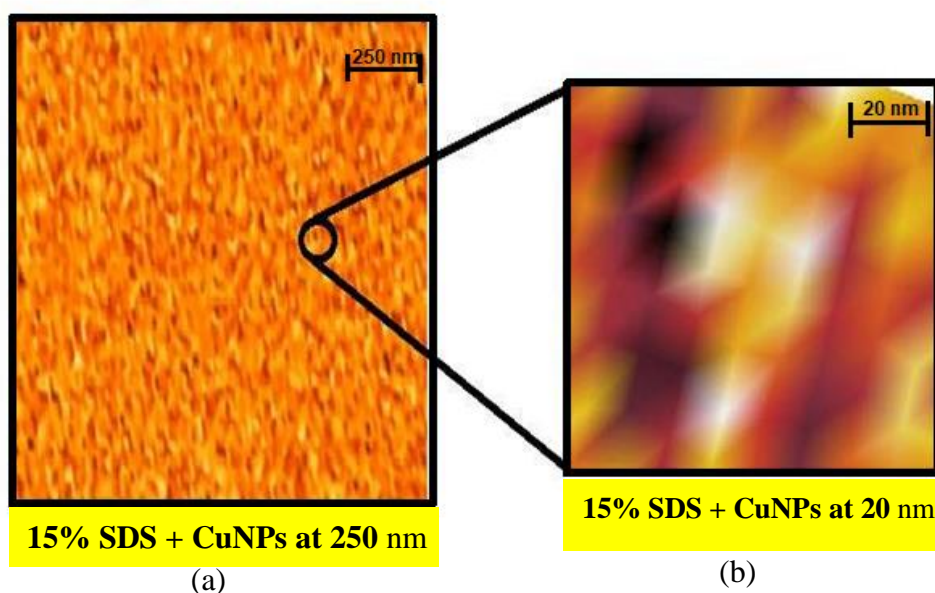


**Figure 23:** AFM image showing the formation of a honey-combed structure (a) 250 nm and (b) 20 nm with CuNPs

The addition of copper nanoparticles (CuNPs) gave topography with a fully formed hexagonal structure as shown in Figure 23, whose morphology is well depicted by the scanning electron microscopy (SEM) images. Figure 23 (b) shows a clear percolation conductive network of copper nanowire (CuNW) attached to the PEDOT bright specs.

The CuNPs interacts with PEDOT: PSS and binds with the PEDOT chains in the process where CuNPs attaches to the PEDOT chains and accumulate at the junctions during solvent evaporation because of strong capillary forces. The PEDOT: PSS solution tends to attach to the metal nanowire because it acts as a binder during solvent evaporation. These results are in close agreement with the work done by Chen, J. *et al.*<sup>[73]</sup>

The surface roughness (Sa) and line roughness (Ra) values of the films decreased as the concentration of SDS increased. At 20% SDS and 15% SDS + CuNPs, the surface and line roughness values increased as shown in the Table 2. The increase in roughness observed at 20% SDS indicates that the size of the conductive domains grows due to partial phase separation. According to Reyes-reyes *et al.*<sup>[74]</sup>, their results show that the roughness increases with the average size of the conductive domains.

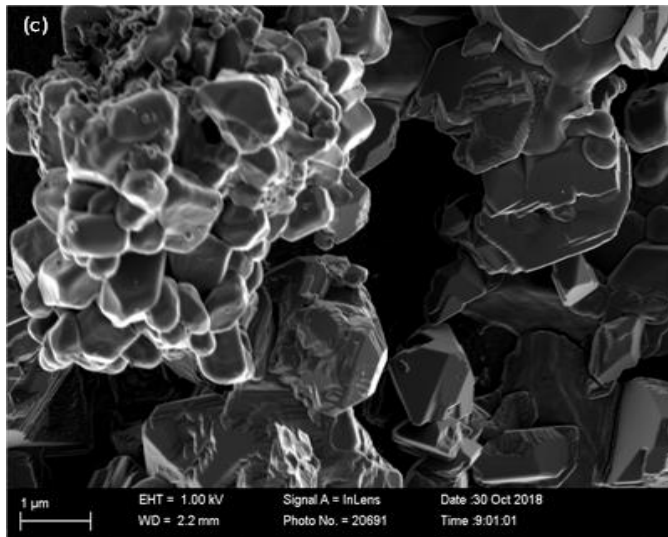
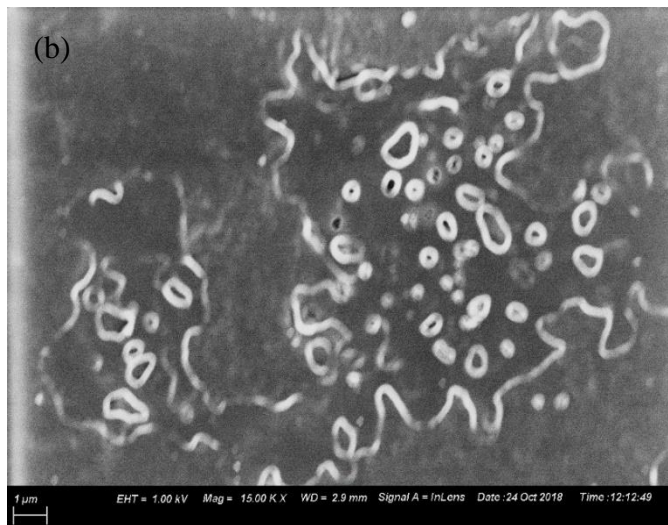
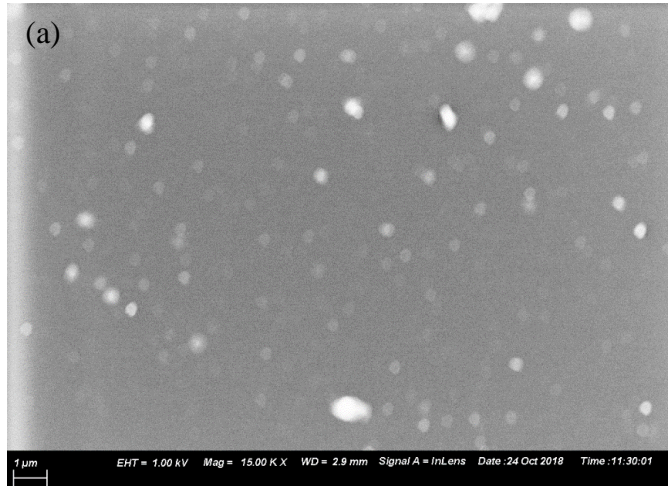
**Table 2:** Table of Roughness values at different doping levels

SDS SURFACTANT LOADING	ROUGHNESS AT 10.3 $\mu$ m		ROUGHNESS AT 500nm	
	Sa (nm)	Ra (nm)	Sa (pm)	Ra (pm)
<b>0%</b>	25.18	29.35	513.14	801.20
<b>5%</b>	15.56	16.43	389.08	408.87
<b>10%</b>	12.63	12.04	308.93	305.75
<b>15%</b>	11.41	11.87	189.50	246.32
<b>20%</b>	20.87	27.55	474.1	584.13
<b>15%+CuNPs</b>	34.65	41.48	1574.10	1844.15

From Table 2, we observe that adding copper nanoparticles to the PEDOT: PSS containing 15% SDS increases in the roughness of the surfaces. Even though the roughness increases, the surface is relatively smooth. This is because the copper nanoparticles are completely buried by the PEDOT: PSS polymer. The low surface roughness is beneficial for reducing shorting in OPV devices<sup>[73]</sup>.

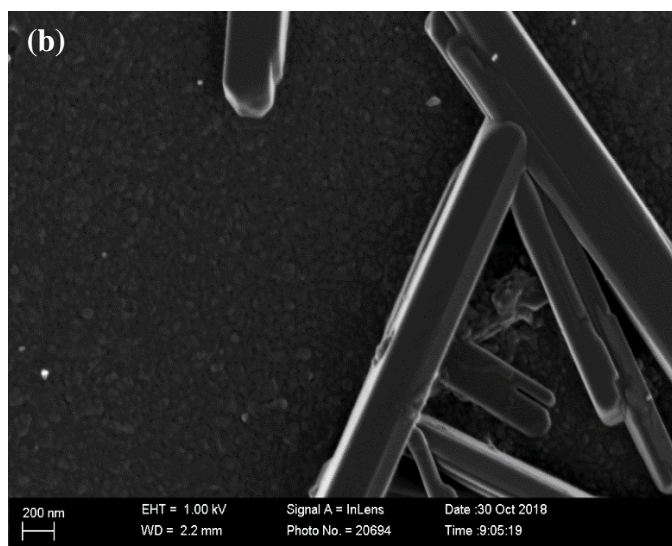
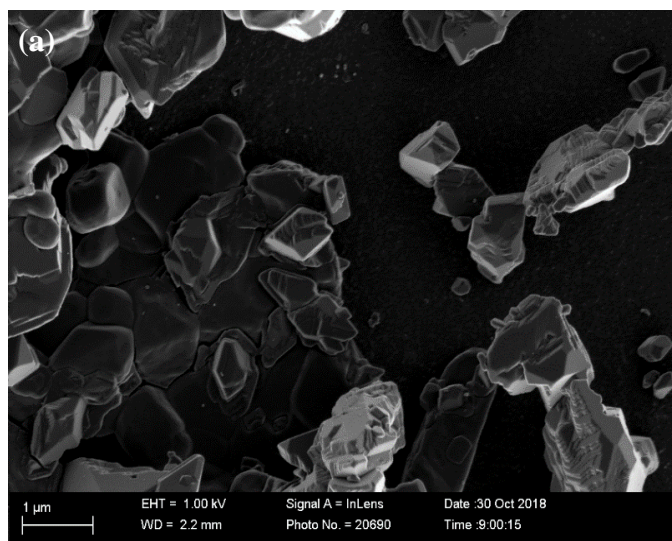
### 5.1.2 Morphological Evaluation by Scanning Electron Microscopy (SEM)

The morphology depicted by Scanning Electron Microscopy showed a good percolation network of copper nanowires beneficial to high conductivity. SEM images showed a substantial difference in the formation of copper nanoparticles concerning the concentration of surfactant.



**Figure 24:** Formation of Face-Centered Cubic (FCC)

Figure 24 shows the step by step trend of how clusters of copper nanoparticles formed into cuboid shaped crystals. At 0% SDS doping, the image from scanning electron microscopy showed no changes for the pristine PEDOT: PSS as shown Figure 24 (a). The image for 15% SDS in Figure 24 (b) shows features of different sizes which are attributed to phase separation that occurs when SDS is added to the PEDOT: PSS solution. The 15% SDS + CuNPs image in Figure 24 (c) shows a well percolated network of the clusters of copper nanoparticles (CuNPs) which grow to form cubic and cuboid like structures.



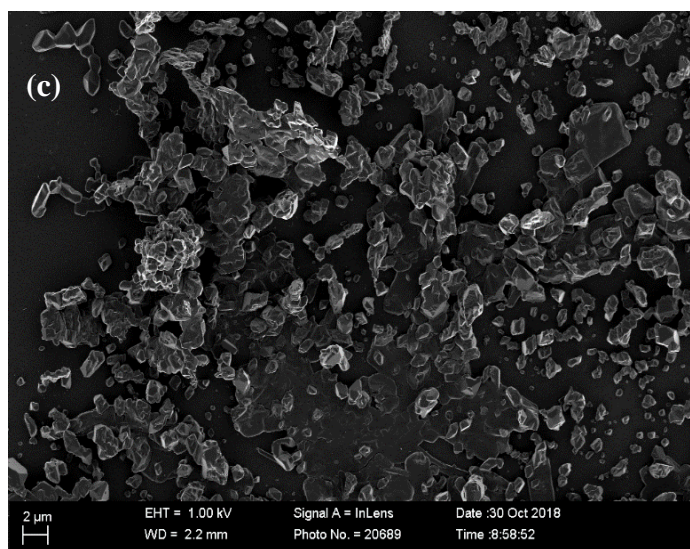


**Figure 25:** (a) Face Centered Cubic (FCC) Nanocrystal, (b) Nanosoldering Structures and (c) FCC crystal structures at 2 μm

In Figure 25, SEM images showed a well-connected percolation network of copper nanoparticles which formed a face-centered cubic (FCC) nanocrystal shown in Figure 25 (a) resulting in a cuboctahedral<sup>[75]</sup> and nano soldering structures<sup>[73]</sup> shown in Figure 25 (b) which explains the hexagonal structures observed in Figure 23 (b). Figure 25 (b) shows the neighboring copper nanowires tightly bonded by PEDOT: PSS at the nanowire junction<sup>[73]</sup>. Figure 25 (c) shows the image of the clusters of Copper Nanocrystals at 2 μm. The nano-soldering structure enhances the conductivity and decreases the nanowire-nanowire contact resistance by increasing the contact surface area under the assistance of the PEDOT: PSS conducting polymer<sup>[73]</sup> as reported by other researchers.

## 5.2 Structural Characterization

Structural characterization was carried out to investigate the structural changes in pristine PEDOT: PSS after doping with sodium dodecyl sulfate and copper nanoparticles.

### 5.2.1 Structural Characterization by X-Ray Diffraction

The X-ray diffraction (XRD) was carried to review the crystal phase and crystallinity of the copper nanoparticles. The XRD diffractogram in Figure 26 shows that the CuNPs have two types of copper oxide as well as the copper hydroxide. The XRD peak at  $41.6^\circ$  and  $37.8^\circ$  corresponded to the presence of copper(1)oxide, and  $45.96^\circ$  and  $47.09^\circ$  corresponded to the presence of copper oxide in PEDOT:PSS:SDS: CuNPs<sup>[76]</sup>. The peaks  $27.9^\circ$  and  $27.8^\circ$  represent the backbone of PEDOT: PSS polymer<sup>[77]</sup> while the peaks  $20.6^\circ$  and  $43.6^\circ$  show the presence of sodium dodecyl sulfate<sup>[78]</sup>.

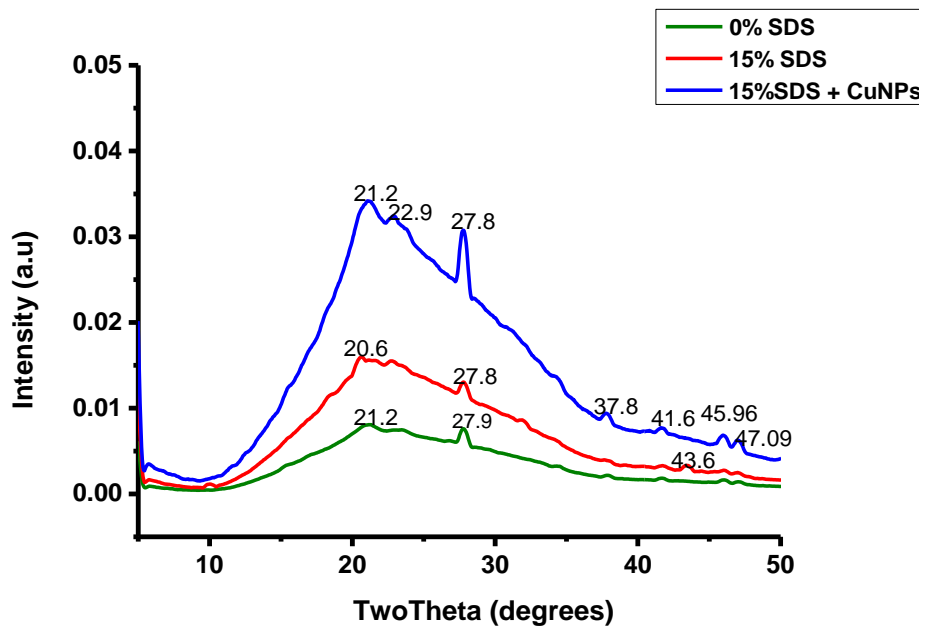
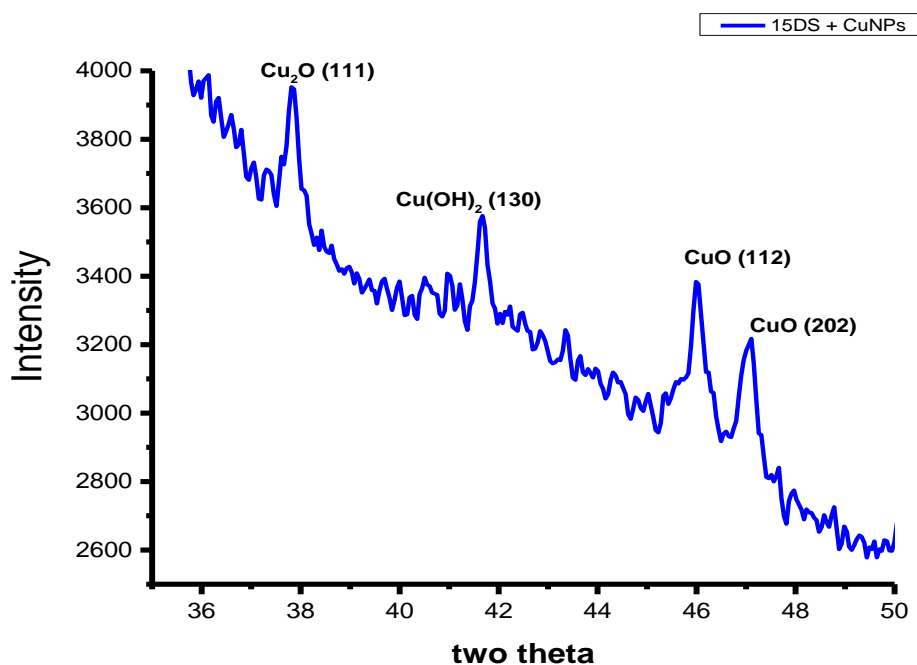


Figure 26: XRD patterns of PEDOT: PSS doped with SDS and CuNPs

In Figure 27, the diffractogram obtained showed the diffraction peaks of the samples corresponding to the characteristic face-centered cubic (FCC) of copper lines indexed as (111), (130), (112) and (202) which were observed in the samples at diffraction angles of  $37.8^\circ$ ,  $46^\circ$ ,  $47^\circ$ , and  $41.8^\circ$ , respectively<sup>[76]</sup>. XRD peaks at (112) and (202) facets were similar in terms of angular positions to those of CuO. The facet (130) was linked to copper hydroxide. The diffraction peak (111) was similar in terms of angular position to that of FCC of copper (I) oxide (Cu<sub>2</sub>O) peaks<sup>[75]</sup>. The (111) facet of copper (I) oxide explains the cuboctahedral structures observed in the Scanning Electron Microscope images in Figure 25 (a).



**Figure 27:** XRD patterns of PEDOT: PSS doped with SDS and CuNPs showing (111), (130),(112) and (202) facets.

The average size of the nanoparticles was calculated using the Debye Scherer's equation shown in equation (20).

$$D = \frac{K\lambda}{\beta \cos\theta} \quad (20)$$

where D is the crystalline size, K is a numerical factor known as the crystallite-shape factor,  $\lambda$  is the wavelength of the X-rays,  $\beta$  is the width of the X-ray diffraction peak in radians also calculated as full width half maximum (FWHM) from the XRD peaks,  $\theta$  is the diffraction angle also known as Bragg angle in radians.  $\theta$  was used to estimate the average size of the nanoparticle in the sample with 15% SDS and CuNPs.

**Table 3:** Calculation of the diffraction angles  $\theta$  and  $\beta$  at full width half maximum (FWHM)

FWHM	2theta	theta	theta(radians)	$\beta = \text{FWHM(radians)}$
1.36491	37.8	18.9	0.329867229	0.023822173

Table 3 was generated from the XRD peaks in figure 30 to calculate the diffraction angles as a full-width half-maximum at  $\lambda = 0.15405$  nm. The average grain size was calculated as 5.8 nm.

### 5.2.2 Structural Characterization by Raman spectroscopy

Raman spectroscopic analysis was carried out to investigate conformational changes in the pristine; SDS and SDS copper nanoparticles-modified PEDOT: PSS. The SDS introduced into PEDOT: PSS replaces PSS as its counter-ions resulting in the conformational change of the PEDOT chains from benzoid (coiled) to quinoid (linear), which is highly conductive<sup>[34]</sup>.

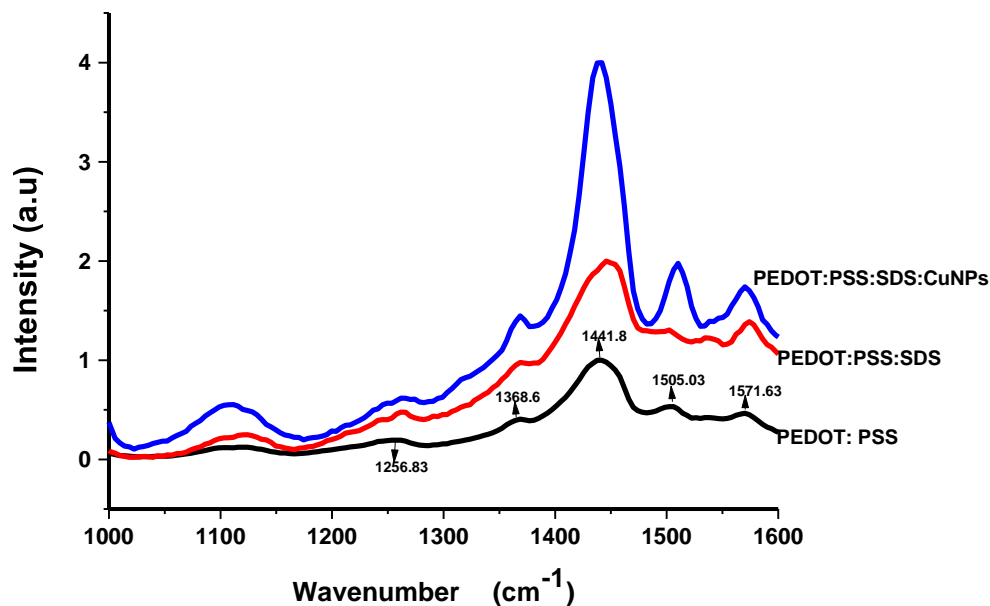


**Figure 28:** Raman spectra of PEDOT: PSS, PEDOT: PSS: SDS and PEDOT: PSS: SDS:CuNPs films.

In Figure 28, the dominant Raman band at  $1441.8\text{cm}^{-1}$  of PEDOT: PSS corresponds to the symmetric stretching mode of the aromatic C=C band. The peak at  $1368.6\text{cm}^{-1}$  represents the  $\text{C}_\beta\text{-C}_\beta$  stretching deformations and the peak at  $1256.83\text{cm}^{-1}$  corresponds to  $\text{C}_\alpha\text{-C}_\alpha$  inter-ring stretching vibrations. The C=C asymmetric stretching vibrations give rise to two bands at  $1505.03\text{cm}^{-1}$ , and  $1571.63\text{cm}^{-1}$  corresponding to the thiophene rings in the middle and at the end of the chains<sup>[35],[61]</sup>.

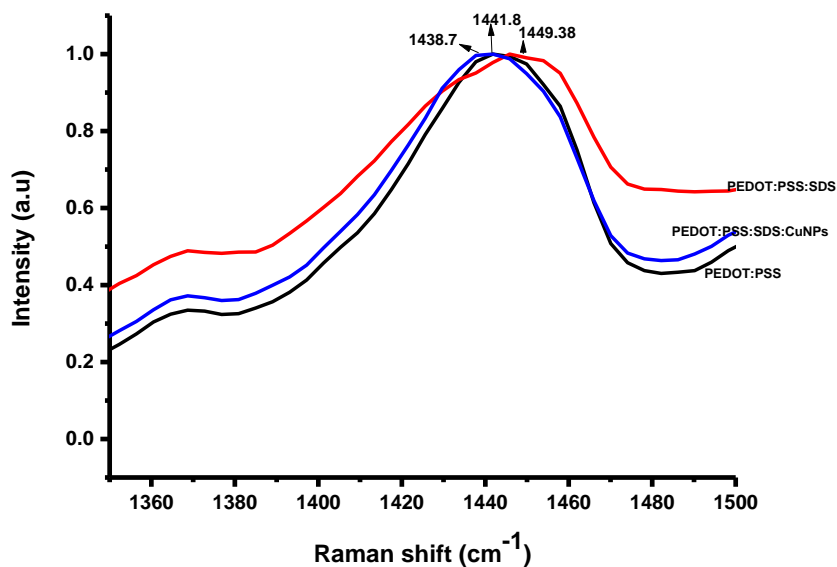


**Figure 29:** Raman spectra of PEDOT: PSS, PEDOT: PSS: SDS and PEDOT: PSS: SDS: CuNPs films

In Figure 29, the Raman spectrum of the PEDOT: PSS: SDS showed an  $8\text{cm}^{-1}$  shifted  $C_{\alpha}-C_{\beta}$  symmetric stretching vibrational peak to higher energy compared with that of pristine PEDOT: PSS. The degree of blue shift of the  $C_{\alpha}-C_{\beta}$  symmetric stretching peak gradually increased with the concentration of SDS and CuNPs. These results suggests that the SDS introduced into PEDOT: PSS solution can replace PSS as the counter ions to PEDOT chain resulting in a conformational change from benzoid (coiled) to a quinoid (linear) structure<sup>[79]</sup>. Contradicting the pristine PEDOT: PSS and PEDOT:PSS:SDS: CuNPs, the  $C_{\alpha}-C_{\beta}$ symmetric stretching peak of the PEDOT:PSS: SDS was a redshift. This redshift implied that the conformation of PEDOT: PSS changed from quinoid to benzoid structure. Hence the conductivity of PEDOT:PSS: SDS increased because of the PEDOT oxidation state changes from bipolaron to

polaron by the PSS removal which is supported by the increase of polaronic states in absorption spectra<sup>[59]</sup> of Figure 30.

### 5.3 Absorption properties

The absorption characteristics were evaluated using the UV-vis spectroscopy which included checking for the absorption peaks of the samples at different surfactant levels. The absorption regions considered under this evaluation process was to check the broadening and flattening of the absorption peaks. The drop in the absorption peaks in the hole transporting layer (HTL) is of great importance to the device performance because it increases the transparency of the HTL. Enhanced transparency increases the transmission of light reaching the active layer which leads to an increase in the generation of excitons.

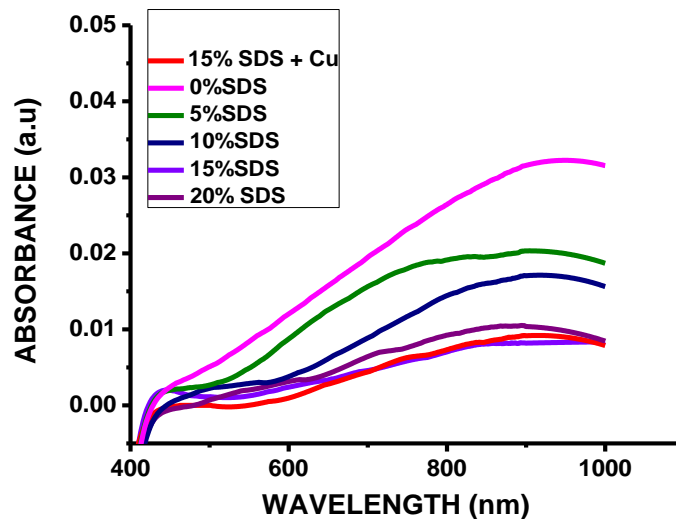


**Figure 30:** Graph of absorbance against wavelength showing the absorbance for each doping level

As most of the light incident on a solar cell should reach the active layer, it is vital to ensure that the Hole Transporting Layer (HTL) should be transparent. In Figure 30, the absorbance dropped from 0%SDS to 15%SDS. At 20% SDS, a slight increase in absorbance is observed which indicated the generation of polaronic states in the bandgap, due to the enhancement of the interchain interaction between the conducting domains. The presence of the polarons is evident by the flattening of the absorption band around 800 nm in Ultra-violet absorption spectra as shown in Figure 30. Therefore, 15% of SDS was considered the optimum for optical properties. The addition of copper nanoparticles increases the absorbance slightly as shown in Figure 30. The slight increase in the absorbance values of the films containing copper nanoparticles is attributed to increased roughness values as discussed earlier in the morphological evaluation by AFM. The slight increase in roughness values causes some of the light to scatter, therefore reducing the amount of light that reaches the active layer.

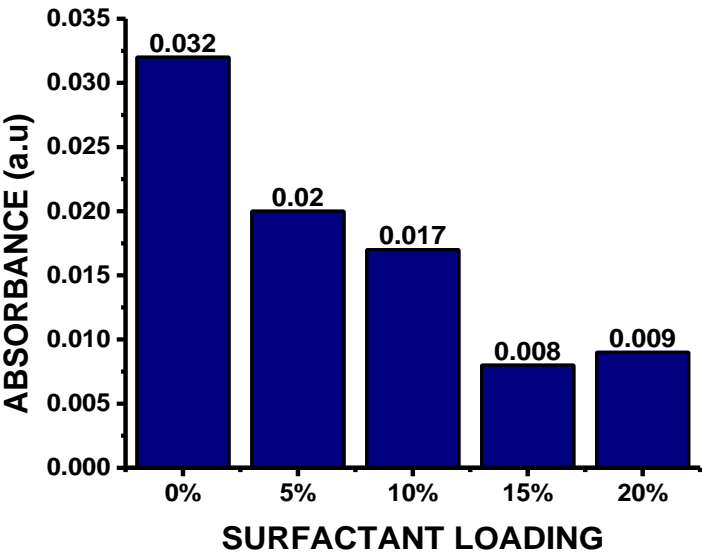


**Figure 31:** column chart showing absorbance at 950nm

In Figure 31, the absorption peak dropped from 0.032 a.u to 0.008 a.u as observed at 15% SDS doping level. The decrease in absorbance led to increased transparency which may be attributed to the alignment of the composites of the polymer PEDOT: PSS after the addition of SDS as discussed in morphological evaluation by AFM.

The reduction of absorbance values from 0.032 to 0.02 as the surfactant loading increased from 0% to 5% is a result of the alignment of the composite polymers which further reduces to 0.017 as the polymer aggregates become more aligned at 10% SDS. From 10% SDS to 15% SDS the polymers aggregates become more regular reducing the absorbance further to 0.008 a.u. The significant decrease in absorbance at 15% SDS doping originates from a strong absorption band from the aromatic rings of PSS<sup>[80]</sup>. This result demonstrated that the insulating PSS in the film was selectively removed<sup>[59]</sup>. The decrease in absorption is also attributed to the flattening of the polarons which was influenced by the weakening of Coulombic attractions between PEDOT and PSS caused by SDS doping. The small increase in the absorbance at 20% SDS was observed indicating the generation of the polaronic states in the bandgap due to enhancement of the interchain interaction between the conducting domains<sup>[81]</sup>.

**Table 4:** Analysis of the optical properties showing a trend in the maximum absorption peak, absorption region and range

SURFACTANT LOADING %	MAXIMUM ABSORPTION PEAK (a.u)	ABSORPTION REGION(nm)	ABSORPTION RANGE
0	0.032	468-1000	532
5	0.020	522-1000	478
10	0.017	615-1000	385
15	0.008	670-999	329
20	0.011	659-994	335
15%SDS + CuNPs	0.009	612-1000	388

In Table 4, as the concentration of the SDS increases and the absorption band around 800 - 1000 nm is observed to flatten which is associated to formation of polarons. The polarons form due to the expanding of the polymers chains and conformation changes from the benzoid to quinoid forms, hence increasing percolating pathways for inter and intra-chain interactions as shown in Figure 9.

## 5.4 Charge Mobility Measurements

The Hall effect measurement was performed to determine the charge carrier transport properties of PEDOT: PSS doped with SDS and copper nanoparticles. The performance of any organic device depends on the mobility of the charge carriers. Charge carrier mobility is the speed (cm/s) at which the charge carriers move in the material in a given direction in the presence of an applied electric field (V/cm). For organic semiconductors to be competitive with amorphous silicon they must approach mobility ( $\mu$ ) of  $1\text{cm}^2/\text{Vs}$  which is also a borderline value between the transport band regime and the hopping regime. These are the two modes of charge transfer. If the mobility is significantly lower than one it is in the hopping regime, if it is significantly higher than one, it is the band regime.

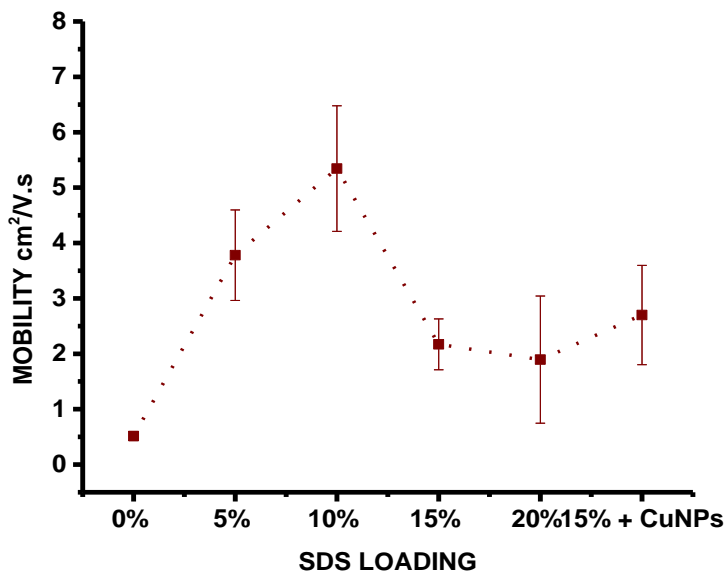


**Figure 32:** Graph of Concentration against Mobility

In Figure 32, a significant increase in charge mobility from  $0.5\text{cm}^2/\text{Vs}$  to  $5.3\text{cm}^2/\text{Vs}$  is observed as the concentration of the SDS increases from 0% SDS to 10% SDS. The carrier mobility obtained from thin-film substrates of highly conductive PEDOT: PSS with SDS and copper nanoparticles was  $5.3\text{ cm}^2/\text{Vs}$ . For the film without SDS and copper nanoparticles, the carrier mobility showed a much lower value of  $0.5\text{cm}^2/\text{Vs}$ .

These results provide direct evidence that the improvement in electrical conductivity in PEDOT: PSS following the addition of SDS and copper nanoparticles is mainly caused by improving the carrier mobility. At 15% SDS, a drop in charge mobility is observed. The SDS- induced reduction in ionic mobility is most likely due to the changes in mesoscale arrangements of the PEDOT polymer aggregates<sup>[82]</sup>. Meso-scale is the intermediate phase between nanoscale size and micro scale. At higher doping levels the SDS leads to an increase in PEDOT aggregation, and slightly tighter  $\pi$ -stacking, as shown in Figure 22 (d) and (e) under the section on morphological evaluation by Atomic Force Microscopy. Hence the PEDOT aggregates lead to mesoscale arrangements as the PEDOT forms continuous domains as observed in Figure 22 (d).

## **5.5Electrical Properties**

The electrical properties were analysed using the curves that were generated from the voltage and current values obtained from the four-point probe. The voltage-current curves were then used to calculate the conductivity values plotted in Figure 33.

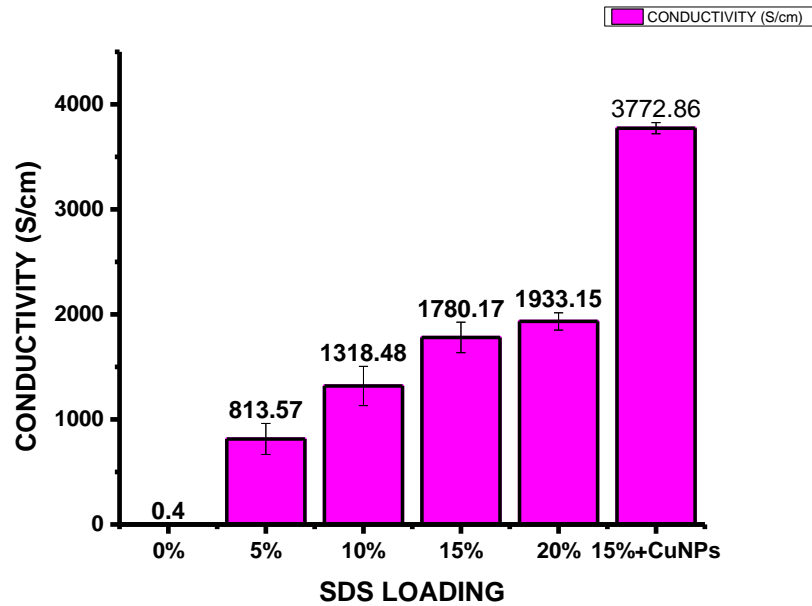


**Figure 33:** Column chart showing conductivity of PEDOT: PSS after doping with SDS and Copper nanoparticles

In Figure 33, an increase in the conductivity of the PEDOT: PSS film was observed as the SDS concentration increased from 0% to 20% and the highest conductivity of 1933.15S/cm, achieved at 20%v/v SDS. The addition of copper nanoparticles further increased the conductivity to 3772.86S/cm as shown in Figure 33. For pristine PEDOT: PSS film the conductivity is 0.4S/cm, while for PEDOT: PSS: SDS films the conductivity increased to 813.57S/cm at 5% SDS doping level. When the concentration of SDS increased to 20%, the conductivity significantly increased to 1933.15S/cm. The increase in conductivity could be attributed to conformational changes in PEDOT due to SDS and the removal of insulating PSS from PEDOT: PSS along with improved crystallinity of PEDOT<sup>[9]</sup> as reported by other researchers. Upon adding CuNPs, the conductivity tremendously increased to 3772.86S/cm as observed from the column chart in Figure 33.

The doping of PEDOT: PSS with SDS weakens the attraction between PEDOT: PSS and phase separation occurs, causing the polymers to expand<sup>[11]</sup>. The expansion improves the network for the interaction of charges among polymer chains hence, reducing the contact resistance of the charges. The formation of the continuous PEDOT network in the polymers, the high contact area and fast transfer of charge carriers resulted in an overall increase in the conductivity of the doped films. The increase in conductivity is also attributed to the fact that PEDOT was tightly bonded to the neighbouring copper nanowires at the nanowire junction as observed in the morphological evaluation by SEM. The nano-soldering enhanced the conductivity and decreased the contact resistance by increasing the contact surface area under the assistance of the conducting polymer<sup>[63]</sup>.

# CHAPTER SIX

## CONCLUSIONS AND RECOMMENDATIONS

### 6.0 Introduction

This chapter gives a summary of the observed morphological, structural, optical and electrical properties of the characterised samples of doped PEDOT:PSS with sodium dodecyl sulphate and copper nanoparticles.

The chapter further entails the future work for this research.

### 6.1 Conclusions

Thin films of doped PEDOT: PSS were characterised for the purpose of a hole transporting layer in organic solar cells. The conductivity of PEDOT: PSS films increased with the addition of SDS, and a further increase was observed with the addition of CuNPs to the optimised PEDOT: PSS. The optimum concentration at which the PEDOT: PSS films improved conductivity was at 15% SDS and 0.3% CuNPs.

The addition of SDS induced segregation of PSS chains and the conformational change of the conductive PEDOT chains. The percolating pathways were improved due to more inter-chain and intra-chain interactions that resulted in higher conductivity. The morphology evolved into a honey-combed structure.

The introduction of SDS into PEDOT: PSS films reduced absorption peak from 0.032 a.u to 0.008 a.u achieved at 15% SDS doping level. This reduction in absorbance led to an increased amount of light reaching the active layer resulting in increased excitation.

SEM images confirmed a well-connected percolation network of CuNPs which formed a nano-soldering structure and a Face-Centered Cubic (FCC) which resulted in a

cuboctahedral structure as revealed from the (111) facet of the diffractogram of the XRD peaks. The crystal size was calculated and estimated to be 5.83nm.

Raman measurements confirmed the conformational change of the PEDOT: PSS from benzoid (coiled) to quinoid (linear). The quinoid structure is highly conductive and hence contributed to the significant increment of the PEDOT: PSS.

The charge carrier mobility increased from  $0.5\text{cm}^2/\text{Vs}$  to  $5.3\text{cm}^2/\text{Vs}$ . These results confirmed that the increase in conductivity is mainly by increasing the charge carrier mobility.

The conductivity of the PEDOT: PSS film increased as the SDS concentration increased from 0 to 690 mM and the highest conductivity of  $1933.15 \pm 53.53$  S/cm. Doping with copper nanoparticles further increased the conductivity to  $3772.86 \pm 53.18$  S/cm.

Phase separation between PEDOT and PSS, removal of excess PSS from the film, increased transparency and conformation change from benzoid to quinoid are the mechanisms for the conductivity enhancement.

## **6.2 Recommendations**

Polymer solar cells are on the increasing global demand for clean energy. In order for polymer solar cells to be competitive, there is need to improve the power conversion efficiencies and stability. Based on my research findings on the characterisation of the PEDOT:PSS samples doped with sodium dodecyl sulphate and copper nanoparticles, there is need to:

1. Study the stability of the PEDOT:PSS doped samples, as the copper nanoparticles oxidises quickly when exposed.
2. Improve the workfunction. Workfunction is a very important parameter for device performance. Workfunction is the amount of energy needed to release the electrons from the material surface and its related to the material optical, electrical and mechanical properties. Therefore, it is essential to know the work function difference of the conducting materials because the high work function is responsible in reducing the barrier height between the anode and polymer interface which results in better holes and electron separation.

## REFERENCES:

1. Battaglia Corsin, Cuevas Andres & Wolf Stefan De. Environmental Science status and perspectives. *Energy Environ. Sci* 1552–1576 (2016). doi:10.1039/c5ee03380b
2. Miles W. Robert, Zoppi, Guillaume Zoppi & Forbes Ian. Inorganic photovoltaic cells The inorganic semiconductor materials used to make photovoltaic cells. *Mater. Today* **10**, 20–27 (2007).
3. Green M. A. Conversion, U. Third Generation Photovoltaics: Ultra-high conversion Efficiency at Low Cost, *Prog. Photovoltaic: Res. Appl*, **135**, 123–135 (2001).
4. You, J., Dou, L., Hong, Z., Li, G. & Yang, Y. Progress in Polymer Science Recent trends in polymer tandem solar cells research. *Prog. Polym. Sci.* **38**, 1909–1928 (2013).
5. Huang, J. S., Goh, T., Li, X., Sfeir, M. Y., Bielinski, E. A., Tomasulo, S.,---- Taylor, A. D. Polymer bulk heterojunction solar cells employing Forster resonance energy transfer: *Nature Photonics* 2–8 (2013). doi:10.1038/nphoton.2013.82
6. Hamid Elsheikh, Mohamed & Shnawah, Dhafer Abdulameer & Sabri, Mohd Faizul Mohd & Said, Suhana Binti Mohd & Haji Hassan, Masjuki & Ali Bashir, Mohamed Bashir & Mohamad, Mahazani, 2014. "A review on thermoelectric renewable energy: Principle parameters that affect their performance," *Renewable and Sustainable Energy Reviews. Renew. Sustain. Energy Rev.* **30**, 337–355 (2014).

7. Mengistsie, D. A., Wei, H-Y., Kuo-C; Chu, C.W., Highly conductive PEDOT : PSS electrode by simple film treatment with methanol for ITO- free polymer solar cells Energy & methanol for ITO-free polymer solar cells.*Energy Environ. Sci.*9662-9671 (2012). doi:10.1039/C2EE22595F
8. Ouyang, J., Chu, C. & Chen, F. Polymer Optoelectronic Devices with Poly ( 3 , 4- Ethylenedioxythiophene ) Anodes. *Macromolecular Science*, **41**, 1497–1511 (2004).
9. Wei, Q., Mukaida, M., Naitoh, Y. & Ishida, T. Morphological Change and Mobility Enhancement in PEDOT : PSS by Adding Co-solvents. *Advanced Materials*. 2831–2836 (2013). doi:10.1002/adma.201205158
10. Fallahzadeh, A. ITO-free organic solar cells using highly conductive phenol-treated PEDOT : PSS anodes. *Org. Electron*. **24**, 188–194 (2015).
11. Zhang Wenfeng, Baofeng Zhao, Zhicai He, Xuemei Zhao, Haitao Wang, Shangfeng Yang,\* Hongbin Wu\* and Yong Cao. High-efficiency ITO-free polymer solar cells using highly conductive PEDOT:PSS/surfactant bilayer transparent anodes. *Energy Environ. Sci.* **6**, 1956–1964 (2013).
12. Zhao, K. Ngongang N., Guy O., Jagadamma, Lethy Krishnan, El Labban, Abdulrahman Hu, Hanlin Wang, Qingxiao Li, Ruipeng Abdelsamie, Maged Beaujuge, Pierre Amassian, Aram . Highly efficient organic solar cells based on a robust room-temperature solution-processed copper iodide hole transporter. *Nano Energy* **16**, 458–469 (2015).
13. Cai, W., Gong, X. & Cao, Y. Solar Energy Materials & Solar Cells Polymer solar cells : Recent development and possible routes for improvement in the

- performance. *Sol. Energy Mater. Sol. Cells* **94**, 114–127 (2010).
14. Gu, S., Neugebauer, H. & Sariciftci, N. S. Conjugated Polymer-Based Organic Solar Cells. *American Chemical Society* 1324–1338 (2007).
  15. Kaur, N., Singh, M., Pathak, D., Wagner, T. & Nunzi, J. M. Organic materials for photovoltaic applications: Review and mechanism. *Synth. Met.* **190**, 20–26 (2014).
  16. Fungura Fadzai. Organic solar cells: Degradation processes and approaches to enhance performance. Graduate Theses and Dissertations. Iowa State University, Ames, Iowa. <https://lib.dr.iastate.edu/etd/15912>. (2016).
  17. Chiechi, R. C., Havenith, R. W. A., Hummelen, J. C., Koster, L. J. A. & Loi, M. A. Modern plastic solar cells: materials, mechanisms and modeling. *Biochem. Pharmacol.* **16**, 281–289 (2013).
  18. Ra, S., Mah, S., Sulaiman, K. & Iwamoto, M. Fundamentals of bulk heterojunction organic solar cells: An overview of stability / degradation issues and strategies for improvement. *Renewable and Sustainable Energy Reviews.* **84**, 43–53 (2018).
  19. Mayer, A. C., Scully, S. R., Hardin, B. E., Rowell, M. W. & McGehee, M. D. Polymer-based solar cells A significant fraction of the cost of solar panels comes from the. *J. Appl. Phys.* **10**, 28–33 (2007).
  20. Jin Zhiwen. & Wang Jizheng. Thin film photoconductors. *Scientific reports* **4**, Article number 5331, 1–7 (2014). doi:10.1038/srep05331
  21. Skompska Magdalena. Hybrid conjugated polymer / semiconductor photovoltaic cells. *Synthetic metals.* **160**, 1–15 (2010). doi:10.1016/j.synthmet.2009.10.031

22. Xu, T. & Yu, L. How to design low bandgap polymers for highly efficient organic solar cells. *Biochem. Pharmacol.* **17**, 11–15 (2014).
23. Yun, J., Yeo, J., Kim, J., Jeong, H. & Kim, D. Solution-Processable Reduced Graphene Oxide as a Novel Alternative to PEDOT : PSS Hole Transport Layers for Highly Efficient and Stable Polymer Solar Cells. *Advanced Materials.* 4923–4928 (2011). doi:10.1002/adma.201102207
24. Beata Luszczynska, Krzysztof Matyjaszewski, Jacek Ulanski. John Wiley & Sons, 16 Sep 2019. Solution-Processable Components for Organic Electronic Devices - Technology & Engineering - 688 pages, University of Technology, Poland. (2019)Solution-Processable Components for Organic Electronic Devices - Google Books.
25. Su, Y., Lan, S. & Wei, K. Organic photovoltaics In the last ten years , the highest efficiency obtained from organic. *Mater. Today* **15**, 554–562 (2012).
26. Su, Y., Lan, S. & Wei, K. Organic photovoltaics In the last ten years , the highest efficiency obtained from organic. *Mater. Today* **15**, 554–562 (2012).
27. Hest, M. F. A. M. Van, M.S. Dabney, J.D Perkins, D. S. Ginley and M. P Taylor. Titanium-doped indium oxide : A high-mobility transparent conduct. *Applied Physics Letters* **87**,032111, 2003–2006 (2012).
28. Moulé, A., Bonekamp, J.-B. & Meerholz, K. The effect of active layer thickness and composition on the performance of bulk-heterojunction solar cells. *Journal of Applied Physics* **100**, (2006).
29. Hansson, R. Materials and Device Engineering for Efficient and Stable Polymer Solar Cells. Karlstad Universty, Sweden. (2017).
30. Lattante, S. Electron and Hole Transport Layers: Their Use in Inverted Bulk

- Heterojunction Polymer Solar Cells. *Electronics* 3(1), 132-164 (2014).  
doi:10.3390/electronics3010132
31. Kalagi, S. S. & Patil, P. S. Secondary electrochemical doping level effects on polaron and bipolaron bands evolution and interband transition energy from absorbance spectra of PEDOT : PSS thin films. *Synth. Met.* **220**, 661–666 (2016).
  32. Hari Singh Nalwa. Effective, B. & Approximation, M. Handbook of Nanostructured Materials and Nanotechnology. 508–513.(1999).
  33. Dietrich, K. Handbook of Conducting Polymers. **38**, Newyork (1987).
  34. Shi, H., Liu, C., Jiang, Q. & Xu, J. Effective Approaches to Improve the Electrical Conductivity of PEDOT : PSS. *Advanced Electronic Materials* - Wiley Online Library: A Review. 1–16 (2015). doi:10.1002/aelm.201500017
  35. Singh, V., Arora, S., Arora, M. & Sharma, V. Characterization of doped PEDOT : PSS and its influence on the performance and degradation of organic solar cells. *iopscience* **045020**, (2014).
  36. Luscombe, C. Somori, P. Pinyi Yang Xiaoyhan Zhou, Gongzhong, Cao, Christine K. Luscombe. Interface Engineering of Organic and Molecular Electronics P3HT : PCBM polymer solar cells with TiO<sub>2</sub> nanotube aggregates in the active layer. *Materials Chemistry* **20**, (2010).
  37. Dai, S. & Yang, S. Improving the Conductivity of PEDOT:PSS Hole Transport Layer in Polymer Solar Cells via Copper(II) Bromide Salt Doping. *ACS Publications*.(2014). doi:10.1021/am505387q
  38. Anna, K. & Moos, R. Why Does the Electrical Conductivity in PEDOT : PSS Decrease with PSS Content ? A Study Combining Thermoelectric Measurements

- with Impedance Spectroscopy. *Polymer Physics*. 976–983 (2012).  
doi:10.1002/polb.23089
39. Chen, C., Kine, A., Nelson, R. D. & Larue, J. C. Impedance spectroscopy study of conducting polymer blends of PEDOT : PSS and PVA. *Synth. Met.* **206**, 106–114 (2015).
  40. Xia, Y. & Ouyang, J. Highly conductive PEDOT : PSS films prepared through a treatment with geminal diols or amphiphilic fluoro compounds. *Org. Electron.* **13**, 1785–1792 (2012).
  41. El-hefian, E. A. & Yahaya, A. H. Investigation on Some Properties of SDS Solutions Investigation on Some Properties of SDS Solutions. *Australian Journal of Basic and Applied Sciences*. (2014).
  42. Jin Y.K., Sun H.K., Hyum H. L., Kwanghee L., Wandu M., Xiong G. and Alan J.H. New Architecture for High-Efficiency Polymer Photovoltaic Cells Using Solution-Based Titanium Oxide as an Optical Spacer . *Advanced Materials*. 572–576 (2006). doi:10.1002/adma.200501825
  43. Peet, J., Tamayo, A. B., Dang, X., Seo, J. H. & Nguyen, T. Small molecule sensitizers for near-infrared absorption in polymer bulk heterojunction solar cells. *Applied Physics Letters*. 2008–2010 (2008). doi:10.1063/1.3001802
  44. Macdiarmid G. Alan, A. J. E. Secondary doping. University of Wollongong Thesis Collections. h n University of Wollongong (2006).
  45. Eun Young Choi, Ji Hyun Seo, Hoe Min Kim, Jun Ho Kim, Jong-Tae Je, Y. K. K. Improved Efficiency and Adhesion Property between the PEDOT:PSS and ITO in Solution-Processed Organic Light-Emitting Diodes. *IEEE*. 3–4 (2010).

46. <http://www.Thebigger.com/physics/conductors-insulators-and-semiconductors/what-is-Doping/#.html>. (2018).
47. Hansson, R. Errisson, *LKE, Holland N. P.* Vertical and lateral morphology effects on solar cell performance for a thiophene – quinoxaline. *J. Mater. Chem. A Mater. energy Sustain.* **3**, 6970–6979 (2015).
48. Shuyan S., Fengmin L., Zhiyuan. X. and Lixiang W. High-Efficiency Hybrid Polymer Solar Cells with Inorganic P- and N-Type Semiconductor Nanocrystals to Collect Photogenerated Charges. *J. Phys. Chem. C*, 114, 19, 9161-9166 (2010).
49. Worfolk BJ1, Andrews SC1, Park S2, Reinspach J1, Liu N3, Toney MF4, Mannsfeld SC5, B. Z. Ultrahigh electrical conductivity in solution-sheared polymeric transparent films. *Pro. Natl. Acad. Sci. USA*. 2015 Nov 17;112(46):14138-14143 (2015).
50. Xu, Y., Liu, C., Khim, D. & Noh, Y.-Y. Development of high-performance printed organic field-effect transistors and integrated circuits. *Phys. Chem. Chem. Phys.* **17**, 26553–26574 (2015).
51. Jørgensen M., Norrman K., Gevorgyan S. A., Tromholt T., Andreasen B, K. F. Stability of polymer solar cells. *Advanced Materials*.2012 Feb 2;24(5):580-612 (2012).
52. Noh, Y. Park, S. Yeo, J. Kim, D., Efficient PEDOT : PSS-Free Polymer Solar Cells with an Easily Accessible Polyacrylonitrile Polymer Material as a Novel Solution- Processable Anode Interfacial Layer. *ACS Appl. Mater interfaces.* (2015). doi:10.1021/acsami.5b07841

53. Wang, Y., Cong, H., Yu, B., Zhang, Z. & Zhan, X. Efficient inverted organic solar cells based on a fullerene derivative-modified transparent cathode. *Materials (Basel)*. **10**, (2017).
54. Nelson, J. Polymer : fullerene bulk heterojunction solar cells The efficiency of solar cells made from a conjugated polymer blended. *Mater. Today* **14**, 462–470 (2011).
55. Zhang, X., Wu, J., Wang, J., Zhang, J. & Yang, Q. Solar Energy Materials & Solar Cells Highly conductive PEDOT : PSS transparent electrode prepared by a post-spin-rinsing method for efficient ITO-free polymer solar cells. *Sol. Energy Mater. Sol. Cells* **144**, 143–149 (2016).
56. Mengistie, D. A. Chen C.H., Boopathi K.M., Chu W., Enhanced Thermoelectric Performance of PEDOT : PSS Flexible Bulky Papers by Treatment with Secondary Dopants. *ACS Applied Material & Interfaces* 7(1):94-100 (2015). doi:10.1021/am507032e
57. Cruz-cruz, I., Reyes-reyes, M., Aguilar-frutis, M. A., Rodriguez, A. G. & López-sandoval, R. Study of the effect of DMSO concentration on the thickness of the PSS insulating barrier in PEDOT : PSS thin films. *Synthetic Metals*, Elsevier **160**, 1501–1506 (2010).
58. Online, V. A., Kim, G., Lim, J. W. & Yun, S. J. *RSC Advances*. (2016). doi:10.1039/C6RA24749K
59. Yeon, C., Kim, G., Lim, J. W. & Yun, S. J. RSC Advances Highly conductive PEDOT : PSS treated by sodium dodecyl sulfate for stretchable fabric heaters †. *RSC Adv.* **7**, 5888–5897 (2017).

60. Zhang, W. Zhao, B. He, Z. Zhao, X. Wang, H. Yang, S. Wu, H. Cao, Y. High-efficiency ITO-free polymer solar cells using highly conductive PEDOT:PSS/surfactant bilayer transparent anodes. *Environmental Science* .1956–1964 (2013). doi:10.1039/c3ee41077c
61. Ouyang, J., Chu, C.-W., Chen, F.-C., Xu, Q. & Yang, Y. Polymer Optoelectronic Devices with High-Conductivity Poly(3,4-Ethylenedioxythiophene) Anodes. *Online) Part A—Pure Appl. Chem.* **41**, 1060–1325 (2004).
62. Mengistie, D. A., Ibrahim, M. A., Wang, P. & Chu, C. Highly Conductive PEDOT : PSS Treated with Formic Acid for ITO-Free Polymer Solar Cells. *ACS Appl. Mater. Interfaces* 2014, 6, 2292–2299 (2014).
63. Xia, Y., Sun, K. & Ouyang, J. Solution-Processed Metallic Conducting Polymer Films as Transparent Electrode of Optoelectronic Devices. *Advanced Matter.* 2436–2440 (2012). doi:10.1002/adma.201104795
64. Wei, Q., Mukaida, M., Kirihara, K., Naitoh, Y. & Ishida, T. Recent Progress on PEDOT-Based Thermoelectric Materials. *Materials.* 732–750 (2015). doi:10.3390/ma8020732
65. Applications of Absorption Spectroscopy (UV, Visible) PharmaTutor. <https://www.pharmatutor.org/pharma-analysis/analytical-aspects-of-uv-visible-spectroscopy/applications.html>. 10/02 (2018).
66. Barbara L Dutrow, Louisiana State University, Christian M. Clark Eastern Michigan University. X-ray Powder Diffraction (XRD). [https://www.researchgate.net/publication/274400086X-Ray Diffraction Instrumentation and Applications](https://www.researchgate.net/publication/274400086X-Ray_Diffraction_Instrumentation_and_Applications). November 2018. The Internet Public Library. 18 November 2018.

67. Graves, R. Practical Raman Spectroscopy. ISBN-13: 978-3-540-50254-8; 3-642-74040-4. The Internet Public Library. 1989.
68. Raman spectroscopy . The Internet Public Library. October 2018.
69. Lindemuth, J. R. An Introduction to AC Field Hall Effect Measurements. Lake Shore Cryotronics.Inc 575 McCorkle Boulevard Westerville, OH43082 USA  
[https://www.lakeshore.com/docs/default-source/product-downloads/applications-notes/acfield\\_appnote\\_h.pdf?sfvrsn=55fc9760\\_7](https://www.lakeshore.com/docs/default-source/product-downloads/applications-notes/acfield_appnote_h.pdf?sfvrsn=55fc9760_7).
70. Raymond A. Serway, John W. Jewett. Emeritus James Madison University, California State Polytechnic University, Pomona. Physics for Scientists and Engineers, 6<sup>th</sup> Edition, ISBN 0534408427, Thomson Brooks/cole (2004).
71. The Hall Effect NIST. The Internet Public Library. February 2018.
72. Socha, E., Soliwoda, K. & Celichowski, G. Honeycomb-structured porous poly(3,4-ethylenedioxythiophene) composite layers on a gold electrode. *Thin Solid Films* **565**, 54–61 (2014).
73. Chen, J., Zhou, W., Chen, J. Fan Y., Zhang Z., Huang Z., Xiaomiao F., Haug W. Solution-processed copper nanowire flexible transparent electrodes with PEDOT:PSS as binder, protector and oxide-layer scavenger for polymer solar cells. *Nano Res.* 8, 1017–1025 (2015). doi:10.1007/s12274-014-0583-z
74. Cruz-cruz, I., Lopez-sandoval, R., Reyes-reyes, M. & Cruz-cruz, I. Enhancement of the Electrical Conductivity in PEDOT : PSS Films by the Addition of Dimethyl Sulfate. *J. Phys. Chem.* 114, 47, (2010). doi:10.1021/jp107386x
75. Abbullah R., Debabrata P., Youngku S. and K. T. Leung. Nanoscale Shape and Size Control of Cubic, Cuboctahedral, and Octahedral Cu–Cu<sub>2</sub>O.pdf. VOL 4. No.

3. 1553-1560.(2010).
76. Sambandam, A., Asiri, A. M. & Wu, J. J. Surfactant Assisted Synthesis of Copper Oxide. *Energy and Environment Focus*. 250-255 (2015). doi:10.1166/eef.2015.1168
77. Yang, W. Zhao Y., He X., Chen Y., Xu J., Li S., Yang Y. and Jiang Y. Flexible conducting polymer / reduced graphene oxide films : synthesis , characterization , and electrochemical performance. *Nanoscale Res Lett* . 015-0932-1(2015). doi:10.1186/s11671-015-0932-1
78. Pal, P. & Pal, A. Surfactant-modified chitosan beads for cadmium ion adsorption. *Int. J. Biol. Macromol.* (2017). doi:10.1016/j.ijbiomac.2017.02.042
79. Ouyang, J. “ Secondary doping ” methods to significantly enhance the conductivity of PEDOT : PSS for its application as transparent electrode of optoelectronic devices. *Displays* **34**, 423–436 (2013).
80. Alemu, D., Wei, H.-Y., Ho, K.-C. & Chu, C.-W. Highly conductive PEDOT:PSS electrode by simple film treatment with methanol for ITO-free polymer solar cells. *Energy Environ. Sci.* **5**, 9662 (2012).
81. Bubnova, O., Crispin, X., Bubnova, O. & Crispin, X. Towards polymer-based organic thermoelectric generators. *Energy & Environmental Science*. **5**, 9345–9362 (2012).
82. Rivnay, J. Inal S., Brian A., Collins, Sessolo M.,Stavriniidou E., Strakosas X., Tassone C. Delongchamp D.M. and Malliaras G.G. Structural control of mixed ionic and electronic transport in conducting polymers. *Nature Communicatations* 1–9 (2016). doi:10.1038/ncomms11287

## APPENDIX:

### Appendix A:

#### Calculation of the average copper nanoparticles crystal size

The size of the crystal was calculated as follows using the values in the table below generated from the plot of intensity versus two theta graph.

FWHM	2theta	theta	theta(radians)	$\beta = \text{FWHM(radians)}$
1.36491	37.8	18.9	0.329867229	0.023822173

$$D = \frac{K\lambda}{\beta \cos\theta}$$

Substituting we get,

$$D = \frac{0.9 * 1.54184}{0.023822173 * \cos(0.329867229)}$$

$$D = 58.25\text{A}$$

Converting from Armstrong to nanometres, we get

$$1\text{A} = 0.1\text{nm} \quad \text{or} \quad 10\text{A} = 1\text{nm}$$

$$D = 58.25/10 = 5.825\text{nm}$$

Hence, the average crystal size is  $D = 5.8\text{nm}$

## Appendix B:

### Current – Voltage Measurements

**Figure 1: Current-Voltage curve for 0% SDS**

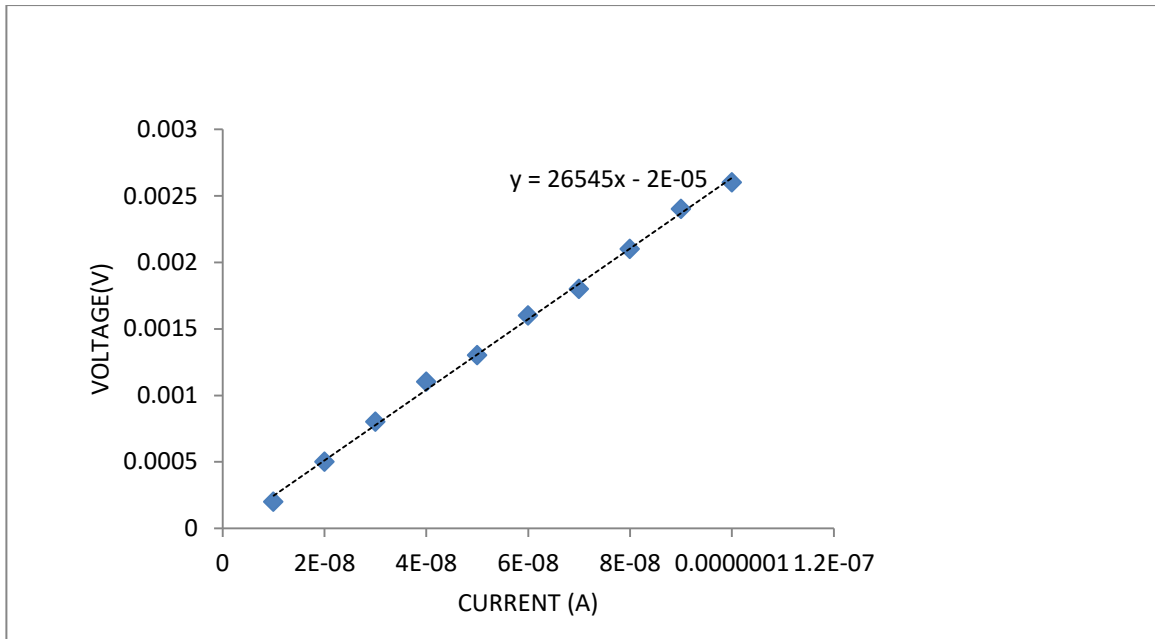


**Figure 2: Current-Voltage curve for 5% SDS**

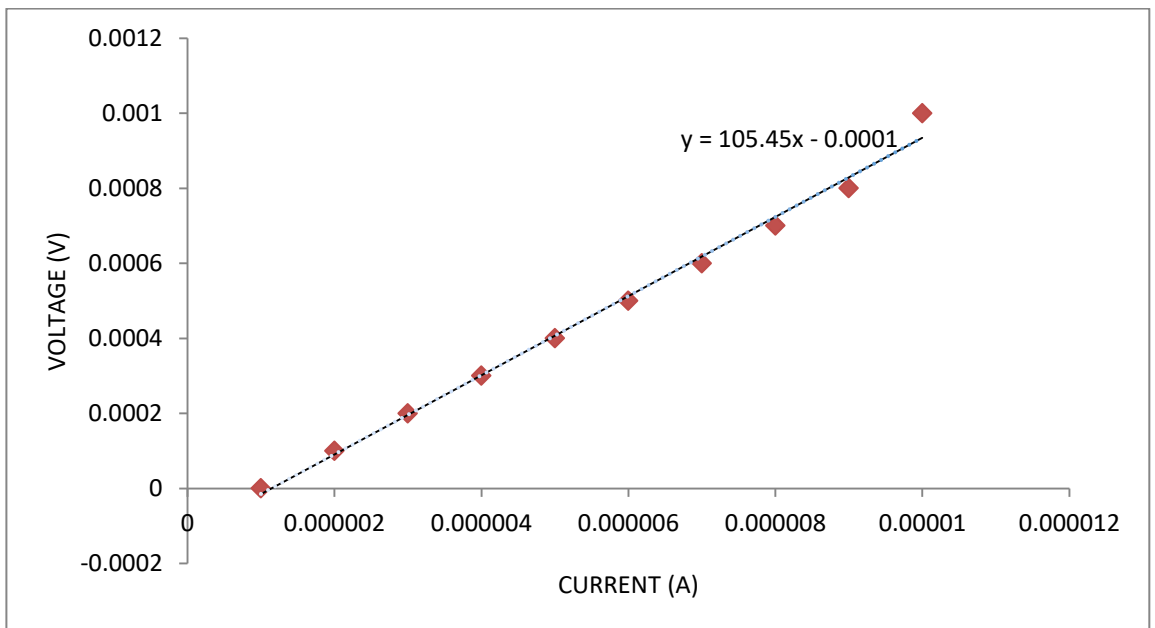


**Figure 3: Current-Voltage curve for 10% SDS**

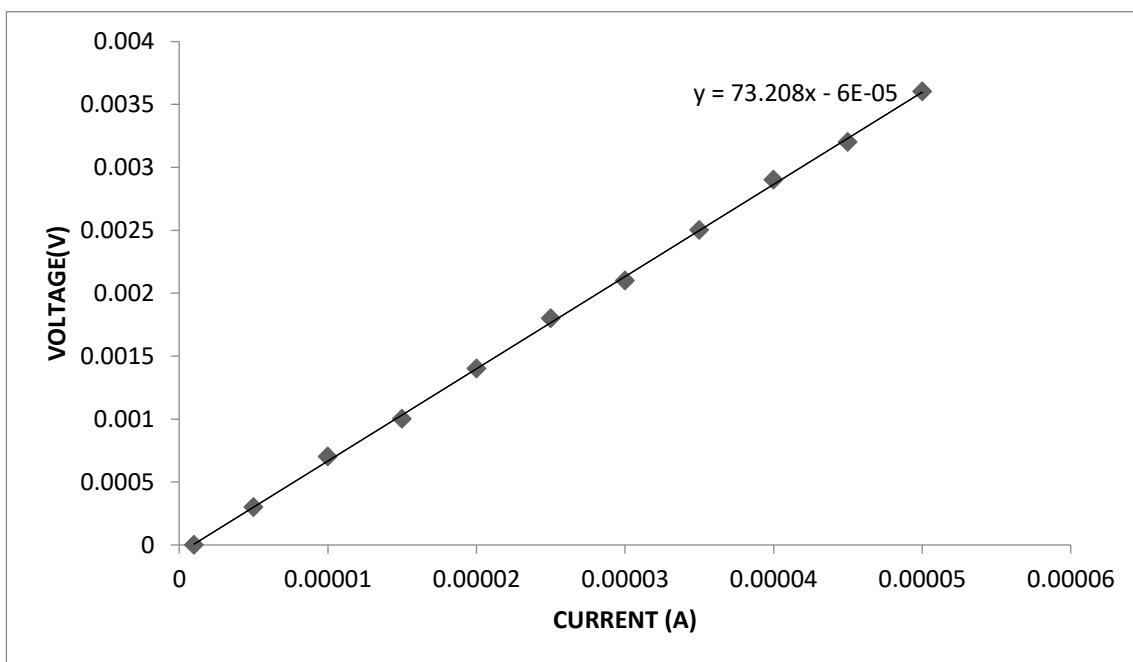


**Figure 4: Current-Voltage curve for 15% SDS**

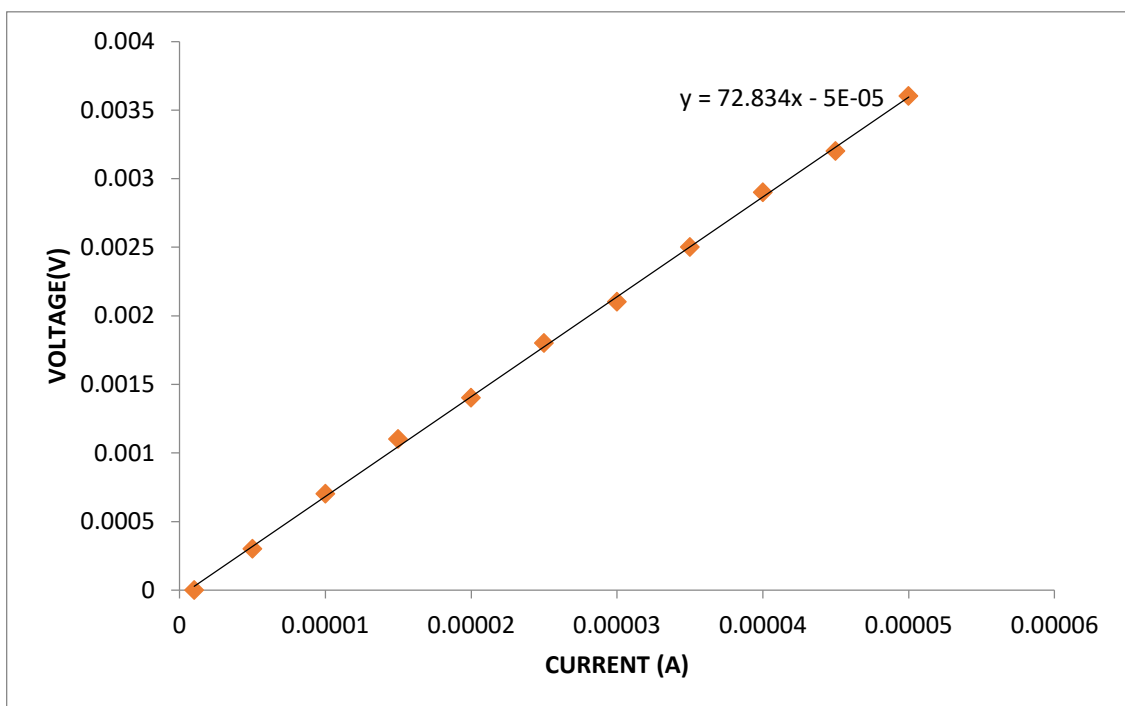


**Figure 5: Current-Voltage curve for 20% SDS**

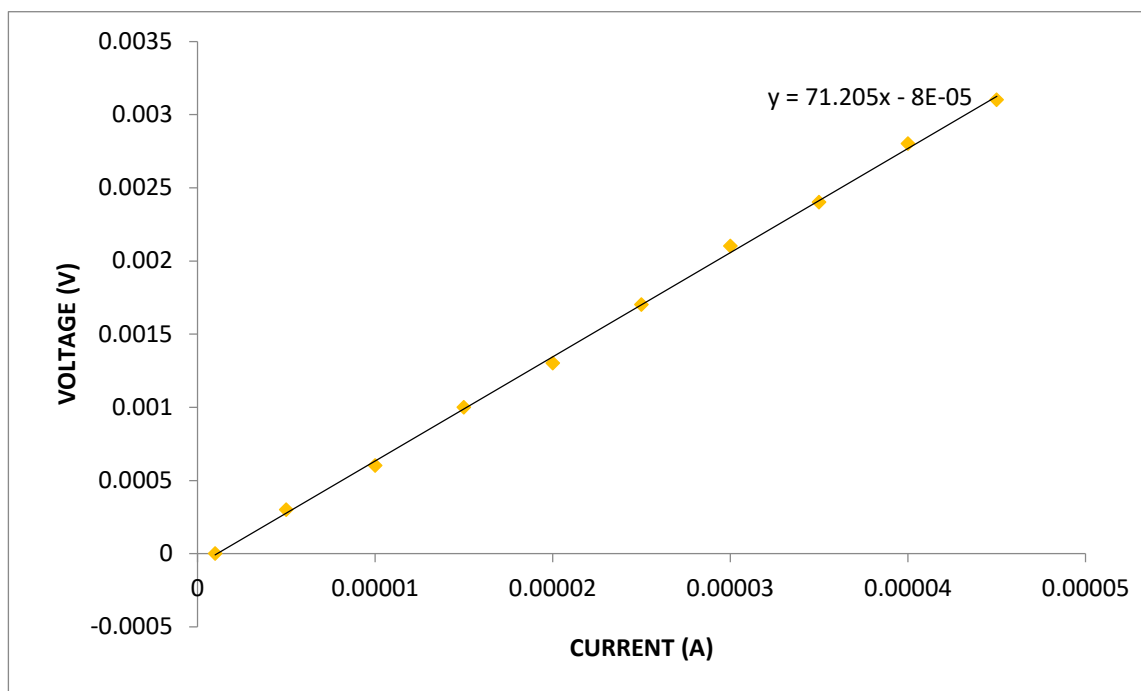


**Figure 6: Current-Voltage curve for 15% SDS and CuNPs**

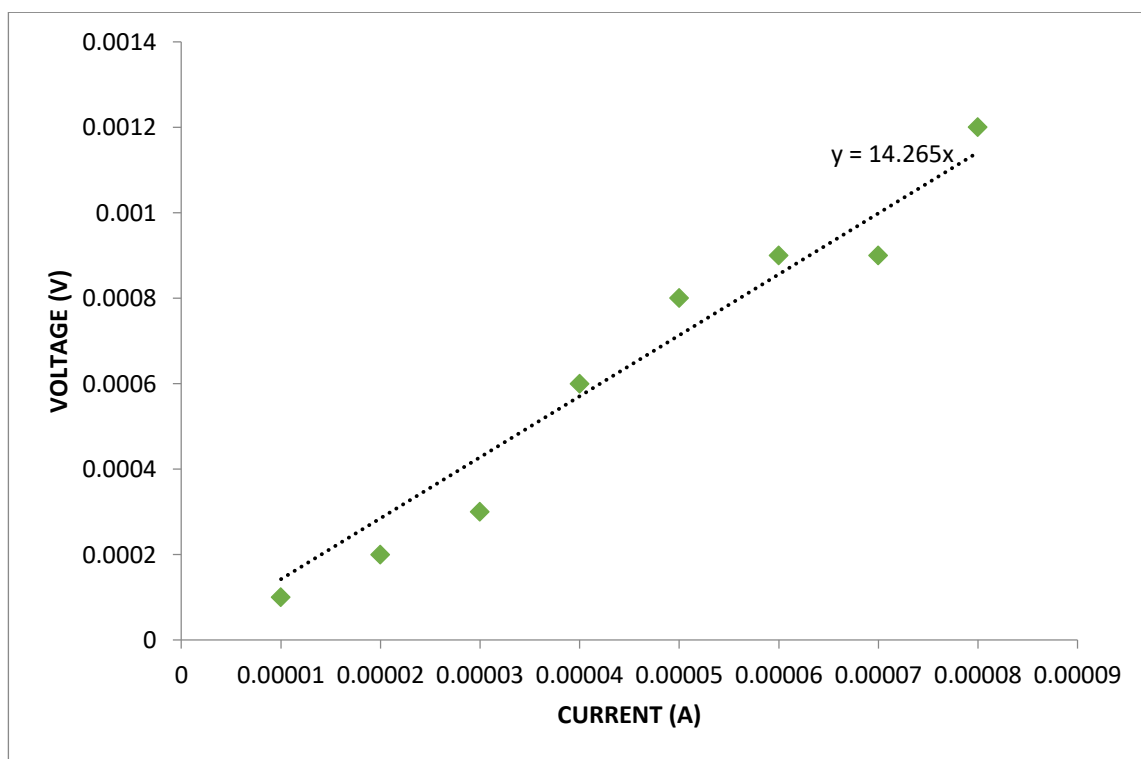


**Table 1: Error analysis in conductivity values for undoped PEDOT: PSS**

0% SDS						
$x$	$n$	$\bar{x}$	$(x - \bar{x})$	$(x - \bar{x})^2$	$\sum (x - \bar{x})^2$	$\sqrt{\frac{\sum (x - \bar{x})^2}{n(n-1)}}$
0.34	3	0.56	-0.22	0.05	0.22	0.19
0.40	3	0.56	-0.16	0.03	0.22	0.19
0.94	3	0.56	0.38	0.14	0.22	0.19

**Table 2: Error analysis in conductivity values for 5% SDS**

5% SDS						
$x$	$n$	$\bar{x}$	$(x - \bar{x})$	$(x - \bar{x})^2$	$\sum (x - \bar{x})^2$	$\sqrt{\frac{\sum (x - \bar{x})^2}{n(n-1)}}$
304.34	3	547.71	-243.37	59230.58	130415.85	147.43
525.23	3	547.71	-22.48	505.50	130415.85	147.43
813.57	3	547.71	265.86	70679.77	130415.85	147.43

**Table 3: Error analysis in conductivity values for 10% SDS**

10% SDS						
$x$	$n$	$\bar{x}$	$(x - \bar{x})$	$(x - \bar{x})^2$	$\sum (x - \bar{x})^2$	$\sqrt{\frac{\sum (x - \bar{x})^2}{n(n-1)}}$
1111.64	3	1268.53	-156.89	24615.52	38546.64	80.15
1318.49	3	1268.53	49.96	2495.67	38546.64	80.15
1375.47	3	1268.53	106.94	11435.45	38546.64	80.15

**Table 4: Error analysis in conductivity values for 15% SDS**

15% SDS						
<b>x</b>	<b>n</b>	$\bar{x}$	$(x - \bar{x})$	$(x - \bar{x})^2$	$\sum (x - \bar{x})^2$	$\sqrt{\frac{\sum (x - \bar{x})^2}{n(n-1)}}$
1231.10	3	1498.92	-267.82	71729.16	126541.75	145.22
1535.50	3	1498.92	36.58	1337.88	126541.75	145.22
1730.17	3	1498.92	231.25	53474.71	126541.75	145.22

**Table 5: Error analysis in conductivity values for 20% SDS**

20% SDS						
<b>x</b>	<b>n</b>	$\bar{x}$	$(x - \bar{x})$	$(x - \bar{x})^2$	$\sum (x - \bar{x})^2$	$\sqrt{\frac{\sum (x - \bar{x})^2}{n(n-1)}}$
1755.38	3	1859.48	-104.10	10837.50	17190.67	53.53
1889.92	3	1859.48	30.44	926.39	17190.67	53.53
1933.15	3	1859.48	73.67	5426.78	17190.67	53.53

**Table 6: Error analysis in conductivity values for 15% SDS + CuNPs**

15% SDS+CuNPs						
<b>x</b>	<b>n</b>	$\bar{x}$	$(x - \bar{x})$	$(x - \bar{x})^2$	$\sum (x - \bar{x})^2$	$\sqrt{\frac{\sum (x - \bar{x})^2}{n(n-1)}}$
3635.08	3	3739.28	-104.20	10856.95	16971.03	53.18
3809.89	3	3739.28	70.61	4986.24	16971.03	53.18
3772.86	3	3739.28	33.58	1127.84	16971.03	53.18